UNIVERSITY OF CALIFORNIA
Santa Barbara

The Dynamics and Near-Source Ground Motion of Supershear Earthquakes

A dissertation submitted in partial satisfaction of the
requirements for the degree of

Doctor of Philosophy

in

Physics

by

Eric Michael Dunham

Committee in charge:

Professor Jean M. Carlson, Chair
Professor Ralph J. Archuleta
Professor James S. Langer
Professor Lars Bildsten

June 2005

The dissertation of Eric Michael Dunham is approved.

Ralph J. Archuleta

James S. Langer

Lars Bildsten

Jean M. Carlson, Chair

May 2005

The Dynamics and Near-Source Ground Motion of Supershear Earthquakes

by

Eric Michael Dunham

To my wife,

Ann Katherine Folkins.

Acknowledgements

My foremost thanks goes to Jean Carlson and Ralph Archuleta, whose guidance, advice, and friendship have been invaluable. Jean offered unwavering support while allowing me complete freedom to pursue my ideas. Ralph provided the grounding of my ideas and was always quick to point out the practical implications of the latest results. To Lars Bildsten I owe much of my inspiration to discover the physics of the natural world. His physical intuition is unequaled and several of the ideas in this work were sparked by his comments. My knowledge of material science largely stems from discussions and interactions with Jim Langer. I also thank Toshiro Tanimoto for his excellent seminars in which I gained a broad exposure to geodynamics and seismology.

I am grateful to Pascal Favreau for introducing me to rupture dynamics and for providing me with a finite difference code that I used extensively in this work. Anael Lemaitre provided many useful discussions regarding friction. I also thank Morgan Page, whose humor made our collaboration most enjoyable.

I owe a special thanks to Bernard Minster and the Institute of Geophysics and Planetary Physics at the University of California, San Diego, for hosting me part-time during the many weeks I spent in La Jolla.

Finally, thanks to everyone who had to deal with the fact that I lived in two

places at once: my friends (in both Santa Barbara and San Diego), my parents and brother (who never knew which place to call, but never gave up trying), and, of course, my wife Ann.

This work was supported by a National Defense Science and Engineering Graduate Research Fellowship through the Office of Naval Research.

Curriculum Vitæ

Eric Michael Dunham

Education

2000–2005	Doctor of Philosophy in Physics, University of California, Santa Barbara
1996–2000	Bachelor of Science in Physics, University of Virginia

Publications

Dunham, E. M., and R. J. Archuleta (2005), Near-source ground motion from steady state dynamic rupture pulses, *Geophys. Res. Lett.*, 32, L03302, doi: 10.1029/2004GL021793.

Dunham, E. M. (2005), Dissipative interface waves and the transient response of a three-dimensional sliding interface with Coulomb friction, *J. Mech. Phys. Solids*, 53, 327-357.

Dunham, E. M., and R. J. Archuleta (2004), Evidence for a supershear transient during the 2002 Denali Fault earthquake, *Bull. Seismol. Soc. Am.*, 94, S256-S268.

Dunham, E. M., P. Favreau, and J. M. Carlson (2003), A supershear transition mechanism for cracks, *Science*, 299, 1557-1559.

Honors and Awards

2004	UCSB Affiliates Graduate Dissertation Fellowship
2004	Outstanding Student Paper, American Geophysical Union fall meeting
2004	Student Presentation Award, Seismological Society of America annual meeting
2002	Outstanding Student Paper, American Geophysical Union fall meeting
2001–2005	National Defense Science and Engineering Graduate Research Fellowship
2000	Graduated with Highest Distinction, University of Virginia
1999	Phi Beta Kappa
1996–2000	Jefferson Scholar, University of Virginia

Abstract

The Dynamics and Near-Source Ground Motion of Supershear Earthquakes

by

Eric Michael Dunham

Earthquake ruptures propagate in one of two velocity regimes: either less than the Rayleigh wave speed (sub-Rayleigh) or between the S- and P-wave speeds (intersonic or supershear). We present an overview of rupture dynamics, the basis of which is a consideration of how waves released by material failure processes in the fault zone transmit shearing stresses ahead of the propagating rupture. Departure from steady state rupture growth generates a set of elastic waves that diffract off of the moving crack edge. These transient diffractions provide the mechanism that allows ruptures to jump between the two propagation velocity regimes. The supershear transition is accompanied by the release of a Rayleigh interface wave on the fault surface, which manifests as a secondary slip pulse trailing the supershear rupture.

Until recently, seismic inversions have revealed most earthquakes to be sub-Rayleigh. Near-source seismograms from the 2002 M_w 7.9 Denali Fault earthquake

offer evidence to the contrary. We present a dynamic rupture model of the event, in which an initially sub-Rayleigh rupture accelerates to supershear velocities prior to the station. The ground motion is characterized by two sets of pulses, one set appearing when the supershear rupture passes the station, and the second when the theoretically predicted Rayleigh wave goes by.

We augment this analysis by calculating synthetic ground motions using two-dimensional analytical solutions for steady state ruptures, valid for an arbitrary traction function within the slip zone, in both the sub-Rayleigh and supershear regimes. These solutions place constraints on which friction law properties can be inferred from near-source records. At supershear rupture velocities, information remains unattenuated as it is transported away from the fault along the S-wave Mach front, a situation that does not occur at sub-Rayleigh speeds. Consequently, ground motion from supershear ruptures offers unprecedented insight into such parameters as the rupture pulse length and the extent of the process zone. This comes at the expense of significantly higher peak velocities and accelerations far from the fault, an obvious point of concern for seismic hazard analyses.

Contents

List of Tables

List of Figures

Chapter 1

Introduction

Tectonic motions, driven by internal convection of the mantle, deform the surface of the Earth. The brittle crust, the outermost portion of the planet, accomodates this deformation through the formation of highly localized weak fault zones on which slip occurs. The rocks surrounding faults sustain small deformations and may consequently be modeled as a linear elastic solid. Deviations from linear elasticity, in particular the extreme strains occuring within the fault zone during slip, become sources in the linear elastic model. We shall refer to these inelastic deformations as the source process.

Slip often occurs in earthquakes, rapid shear fracture events characteristic of highly strained brittle materials under compression. Ruptures follow complicated paths through fault zones determined by the interplay between the heterogeneous fault strength and the elastic waves released when the fault zone material fails. These elastic waves play a central role in earthquake dynamics. In the vicinity of the fault, they redistribute the stress field, transmitting the driving force of the rupture to the unbroken region ahead of the propagating rupture front. The rupture consequently proceeds at a velocity comparable to the elastic wave speeds, meaning that inertial dynamics of the elastic material surrounding the fault become important. The most pronounced manifestation of this feature is the generation of seismic waves that are responsible for the destructive ground motion well known to those who live in the vicinity of active faults.

The rheology of fault zones and the resulting friction laws are the subject of considerable debate. We avoid this question entirely in this work. The only requirement that we demand of the source process is that slip occurs as the strength of the fault zone decreases. This process is dissipative, characterized by a flow of kinetic and strain energy from the elastic medium into the slipping fault zone. The dissipated energy is typically classified as friction (the energy lost due to frictional sliding behind the rupture front) and fracture energy (the energy consumed at the rupture front that is required to extend the rupture in the absence of friction on the slipping fault). We further assume, based on entropic arguments, that this energy enters a disordered form (eventually heat) and cannot be recovered as elastic energy.

The primary focus of this work is the relationship between rupture speed and seismic waves. The geometry of many ruptures, particularly crustal strike-slip events, is such that the rupture moves in the direction of slip. In this case, the source process generates both P and S waves. The interference of these waves introduces another velocity, the Rayleigh speed c_R, which is slower than either the P- or S-wave speeds c_p and c_s. Ruptures propagate in one of two rupture velocity regimes, either less than the Rayleigh speed (sub-Rayleigh) or between the S- and P-wave speeds (intersonic or supershear). At supershear velocities, S waves radiate from the rupture to form a Mach front, completely changing the

seismic signature and ground motion of these events.

Evidence for supershear ruptures continues to mount, warranting further exploration of the phenomenon. In this work, we focus on two aspects: the dynamics of the supershear transition and the seismic signature of supershear ruptures in near-source ground motion. This work is organized as follows. A review of the literature is provided in Chapter 2, which assumes a certain basic knowledge of fracture mechanics. Such may be found in any number of review articles (Rice, 1980; Dmowska and Rice, 1986; Das, 2003) or texts (Freund, 1989; Broberg, 1999a), and a review of intersonic fractures, focusing particularly on laboratory experiments, has recently appeared (Rosakis, 2002). Chapter 3 discusses elastic waves and the earthquake source process, and provides an explanation for the allowed propagation velocity regimes. Chapter 4 contains a study of elastic wave propagation in the vicinity of frictionally sliding faults. After these preparatory studies, we examine in Chapter 5 the ground motion from steady state ruptures propagating with both sub-Rayleigh and intersonic speeds. We then turn in Chapter 6 to the underlying dynamics behind the supershear transition. Finally, in Chapter 7 we bring these theoretical ideas together with seismic data to present evidence for supershear rupture speeds in the 2002 Denali Fault, Alaska, earthquake.

Chapter 2

Background

The speed at which ruptures propagate depends on their geometry, which may be decomposed into three modes. Tensile, or mode I, fracture is the most common failure mode in engineering materials, and involves symmetric normal displacement of the crack faces. Under conditions of large compressive stresses, as commonly occur in the earth, failure may occur via shear slip along an interface. Shear fractures are classified as either mode II or mode III, depending on the relative orientation of the slip vector and the crack edge (or rupture front, as we shall often call it). Mode II rupture has slip perpendicular to the front, and mode III has slip parallel to it. In this work, we shall be concerned only with the shear failure modes since no evidence of tensile failure has been observed in earthquakes.

2.1 Theoretical Studies

Mathematical solutions for propagating ruptures appeared in the early 1960s in the context of the singular crack model. The solution for self-similarly expanding mode I cracks was given by Broberg (1960), and the corresponding problem for mode II shear cracks was obtained by Kostrov (1964). The solution for a steady state semi-infinite crack involving a combination of mode I and II loading was obtained by Craggs (1960). In these models, all of the dissipation is localized to the crack edge, where the stress field diverges as the inverse square-root of the

distance from the edge. This singularity acts as an energy sink in an otherwise linear elastic body. A flux of energy into the crack edge is taken to be a physical requirement for occurence of rupture. At sub-Rayleigh speeds, energy flows from the elastic medium into the crack edge, as required (Craggs, 1960). For speeds between the Rayleigh and S-wave speed, the flow of energy reverses, and the propagating crack releases energy into the elastic medium (Kostrov, 1964; Fossum and Freund, 1975). Since this process violates our basic assumption that rupture is a dissipative phenomenon, this rupture velocity regime is forbidden.

The intersonic (or supershear, as it is known within seismology) rupture velocity regime, in which the rupture speed lies between the S- and P-wave speeds, has more complicated energetics. Application of the singular crack model yields solutions for which the singularity at the crack edge is weaker. The stress field σ diverges as $\sigma \propto r^{-q}$, where r is the distance from the edge and $0 < q \leq 1/2$ (Burridge, 1973; Andrews, 1976). The exponent q is a function of rupture speed and takes on the value $1/2$ only at the particular speed of $\sqrt{2}c_s$. Except at this speed, the singularity is too weak to be associated with a flow of energy into the crack edge, leading to the (mistaken) conclusion that intersonic propagation is not possible except at $\sqrt{2}c_s$.

A major change in the wavefield occurs at intersonic speeds: The S waves excited by the propagating rupture switch from being evanescent to radiating

waves, manifesting in the formation of a distinctive Mach front. An exception to this again occurs at $\sqrt{2}c_s$, a speed at which no S waves are excited. The absence of radiation at this speed was noted quite early by Eshelby (1949) in a study of propagating edge dislocations. This coincidence suggests a connection between energy dissipation at the crack edge and emission of S-wave radiation that will be discussed in Chapter 5.

The early conclusion that the limiting velocity of mode II ruptures was the Rayleigh speed (Craggs, 1960) was first questioned by Burridge (1973), who conducted an analytical study of self-similarly expanding cracks with a finite-stress fracture criterion. This criterion has the property that stresses remain bounded at the crack edge, as expected for a real material, but carries with it the unphysical consequence that no energy is dissipated from the medium. Despite this questionable assumption, Burridge (1973) obtained solutions for shear ruptures at the P-wave speed, hinting that elastic waves moving along faults at intersonic speeds transmit driving forces that could potentially generate intersonic shear failure.

A physically satisfying approach was taken by Andrews (1976) in his numerical models of shear crack growth. The key idea was to remove the singularity at the crack tip by introducing a finite length scale over which dissipative processes occur, a feature that most certainly occurs in real materials. To simplify the numerical calculations, this region, known as the process zone, is confined to

the fault plane. This idea emerged in the work of Barenblatt (1959) and Dugdale (1960) for tensile cracks, where it was known as the cohesive-zone model, and was extended to shear fractures by Ida (1972, 1973) and Palmer and Rice (1973). Andrews (1976) introduced this into his numerical models through a slip-weakening fracture criterion, in which the fault strength decreases from a peak strength (or yield stress) to a residual strength (or sliding friction) as the fault slips. The amount of slip required to decrease the strength to the residual strength is known as the slip-weakening distance. With this fracture criterion, ruptures propagate spontaneously, as the actively slipping zone extends whenever the stress on the fault reaches the peak strength.

In his numerical models, Andrews (1976) observed that bilaterally expanding cracks begin at sub-Rayleigh speeds. As the crack expands, a peak in shear stress moving at the S-wave speed develops ahead of the crack tip, a feature revealed in the earlier study by Burridge (1973). Under certain conditions (basically, when faults are loaded close to failure), this peak exceeds the peak strength of the fault, initiating a secondary rupture ahead of the original sub-Rayleigh crack. The secondary rupture expands at intersonic speeds around $1.5c_s$ and the original rupture coalesces with it. In this way, the rupture bypasses the forbidden velocity region between c_R and c_s by simply jumping discontinuously across it. The same effect was observed in the numerical work by Das and Aki (1977b).

A complimentary analytical study of steady state intersonic cracks appeared soon after this (Burridge et al., 1979). Like Andrews (1976), Burridge et al. (1979) introduced a finite cohesive zone, actually idealized to a single point force following at a fixed distance behind the crack tip. The strength of this point force was chosen such that the stresses at the crack tip remained finite. They found that while all intersonic speeds were allowed, the region between c_s and $\sqrt{2}c_s$ was mechanically unstable, in the sense that propagation at faster speeds required a smaller load. This conclusion was consistent with the simulations of Andrews (1976), in which intersonic rupture speeds were always greater than $\sqrt{2}c_s$.

Other seismologically relevant studies from this time dealt with propagating rupture pulses (where the slip zone has a fixed width), rather than with traditional cracks (where the area of the actively slipping zone grows with the rupture). The rupture pulse model is closer to a propagating dislocation, which was successfully used by Aki (1968) in his seminal study of the near-source records of the 1966 Parkfield earthquake. This model was studied for an arbitrary shear traction distribution within the slip zone by Broberg (1978). This study was initially constrained to sub-Rayleigh rupture speeds, although this restriction was lifted in later work (Broberg, 1989). Freund (1979) also studied the rupture pulse model, both for sub-Rayleigh and intersonic ruptures, but only in the singular limit. Analytical studies of self-similarly expanding cracks in the intersonic regime were

conducted by Broberg (1994, 1995), who built on ideas developed earlier regarding the necessity of cohesive zones for a finite energy dissipation at intersonic speeds (Broberg, 1989).

There has recently been a growing number of papers related to intersonic growth, spurred particularly by the laboratory experiments of Rosakis, which are discussed in the next Section. Steady state growth under combined mode I and II loading, as might occur in engineering applications, has been investigated both numerically (Geubelle and Kubair, 2001) and analytically (Kubair et al., 2002). Intersonic growth is possible, with the mode II component driving the rupture while the mode I component resists.

Intersonic propagation, in particular the supershear transition, has also received attention in three-dimensional or shear mixed mode loading. These include numerical studies of three-dimensional problems having two-dimensional planar faults. This involves a combination of mode II and III loading that varies around the rupture front. Day (1982b) found that for relatively homogeneous faults, the supershear transition occurs in the predominantly mode II direction via the same mechanism described earlier by Andrews (1976). This conclusion was also reached by Johnson (1990). For heterogeneous faults, ruptures can discontinuously jump to sections close to failure, leading to apparent rupture speeds exceeding the *S*- or even *P*-wave speed (Day, 1982b). The supershear transition in the presence

of heterogeneities has been studied by Fukuyama and Olsen (2002) and Dunham et al. (2003). These studies indicate that local bursts of supershear rupture are common in dynamic crack models.

Studies of the supershear transition for three-dimensional ruptures expanding radially outward from an initially circular nucleation patch were conducted by Madariaga and Olsen (2000) and Madariaga et al. (2000). They found that the supershear transition occurs smoothly, unlike the discontinuous jump described by Andrews (1976). The supershear transition occurs first in the mode II direction and spreads laterally around the rupture front.

A number of analytical solutions have recently appeared, focusing on the unsteady growth of semi-infinite cracks in the intersonic regime or on the jump between the sub-Rayleigh and intersonic regimes. At the basis of these problems is a self-similar "fundamental" solution that can be used in superposition schemes to solve non-steady problems. The method was pioneered by Freund (1972a,b) for mode I cracks and extended to sub-Rayleigh mode II cracks by Fossum and Freund (1975). An alternative path to the solution for non-uniformly moving cracks in the sub-Rayleigh (for mode I and II) and subshear (for mode III) regimes was given by Kostrov (1975). The solution to the "fundamental" solution for intersonic cracks was obtained by Huang and Gao (2001), who then used the results to study a suddenly stopping intersonic crack (Huang and Gao, 2002). The solution

was used by Guo et al. (2003b) to solve the problem of a suddenly decelerating or accelerating crack. Their results highlight the fact that both S waves and Rayleigh waves trail supershear ruptures. When a rupture decelerates from the intersonic to sub-Rayleigh regime, these waves will catch up to the crack edge and influence its dynamics. A solution for a continuously accelerating intersonic crack is given by Broberg (1999b). For semi-infinite intersonic cracks subject to a time-dependent load, the stress intensity factor has been derived by Guo et al. (2003a).

Antipov et al. (2004) studied the cohesive-zone model for intersonic cracks, obtaining a simple expression for the energy release rate as a function of rupture speed and cohesive zone size. This result was used by Obrezanova and Willis (2003) in a linearized stability analysis of intersonic cracks. They concluded that the crack is stable to two-dimensional perturbations of its propagation velocity, in accordance to what has been observed in numerical simulations.

Supershear crack growth has also been studied in molecular dynamic simulations (Abraham and Gao, 2000; Abraham et al., 2002), in which particles interact via a Lennard-Jones potential. They found that the supershear transition occurs as described by Andrews (1976), indicating that the transition mechanism is a rather universal feature associated with wave propagation in an elastic solid. Gao et al. (2001) provided an analytical analysis of these simulations, which they used

to predict the timing of the supershear transition.

2.2 Laboratory Experiments

Recent interest was spurred by the observation of supershear ruptures in laboratory experiments (Rosakis et al., 1999). The original experiments were conducted using a plate containing a pre-existing notch to act as a stress concentrator. The material was chosen because of its rheology as a brittle solid (similar to rock) and to its photoelastic properties, which allow the imaging of the internal stress field via interference fringe patterns. The rupture was triggered by the impact of a moving projectile, which generates a loading wave and transmits driving stresses to the stress concentration at the notch. Evidence of supershear speeds comes from the distinctive Mach fronts emanating from the ruptures. Finite element simulations of the experiment were conducted by Needleman (1999). An analytical study of self-similar cracks with a velocity-weakening cohesive zone by Samudrala et al. (2002) explains many of the observed features, including tensile microcracks that were observed on the extensional side of the interface.

Recently, the laboratory experiments have been modified to mimic real faults, in which slip occurs on a pre-existing frictional interface. An interface is cut in the sample and held in place by a compressive load. A shear load mimics the

tectonic stress field prior to an earthquake. The rupture is nucleated in the center of the interface by exploding a small wire. Using this setup, Xia et al. (2004) have captured the transition from sub-Rayleigh to supershear speeds, which in their experiments occurs via a discontinuous jump originally described by Andrews (1976).

2.3 Seismic Observations

Supershear rupture speeds have been inferred for several earthquakes, based on various types of data ranging from near-source to teleseismic records. Many of these studies rest on seismic inversions, a procedure for extracting source parameters from a finite data set. The inverse problem is underdetermined, resulting in instability unless additional assumptions are made. These typically involve constraints on slip positivity (no reverse slip is permitted) and solution smoothness. Inherent trade-offs between variations in rupture speed and variations in slip render accurate statements regarding local rupture speeds somewhat difficult to substantiate.

For the most part, supershear ruptures seem to occur on well-developed, active strike-slip faults (e.g., the Izmit, Duzce, Kunlunshan, and Denali Fault events). Exceptions to this rule appear to occur when the rupture process is sufficiently

heterogeneous as to involve some focusing process or rupture of a highly loaded region (e.g., the Imperial Valley and Landers events). The geologic or tectonic setting is likely correlated with the propensity for supershear ruptures. New faults will be complex, composed of multiple, partially connected fault segments. Rupture through such a system will be locally delayed during the transfers between faults, and the driving radiation is likely to be less coherent due to scattering at the junctions. On the other hand, well-developed fault systems consist of a single dominant fault that accomodates almost all of the deformation of the region. These faults are often quite straight, which will enhance the coherence of the driving radiation and more easily promote supershear ruptures. The data appear to support this idea, although the paucity of records from large faults renders such a conclusion rather speculative. In the remainder of this Section, we summarize the studies of earthquakes for which supershear speeds have been suggested.

1979 Imperial Valley, California

The first seismic observation of supershear rupture speeds comes from the Imperial Valley earthquake. Trial and error waveform fitting of near-source strong motion data by Archuleta (1984) suggested that the rupture process was quite variable, with rupture speeds approaching the P-wave speed at depth during the later stages of rupture on the Imperial Fault. The argument rests not on the dom-

inant fault normal motions, which could be explained by a sub-Rayleigh rupture, but on fault parallel motions recorded, in particular, at distances quite removed from the fault. The amplitudes at these distances were larger than would typically be expected. This observation foreshadows our conclusions regarding the ground motion generated by the *S*-wave Mach front, and will be discussed in Chapter 5.

The possibility of supershear speeds had been suggested earlier in the inversion results of Olson and Apsel (1982), who also used near-source data. They constrained the average rupture velocity to $0.9c_s$, but allowed local variations in rupture time both ahead and behind the average by allowing slip in multiple time windows surrounding and centered on the average. Their results indicated supershear speeds over the same section identified by Archuleta (1984). Analysis of data from a short baseline accelerometer array, from which the location of the incident radiation could be determined, also suggested supershear speeds (Spudich and Cranswick, 1984). Not all studies reached this conclusion, however. Two other studies, the first by Hartzell and Helmberger (1982) using near-source data and the second by Hartzell and Heaton (1983) using both near-source and teleseismic data, did not find supershear rupture. As discussed by Archuleta (1984), their models underpredict the ground motion at stations removed from the fault.

1992 Landers, California

The Landers earthquake offers an example of an extremely complex rupture process with highly variable rupture speed. Unlike the other earthquakes discussed in this section, the Landers earthquake propagated through numerous fault segments having various orientations, none of which play a dominant role in accomodating lithospheric deformation. The inversion by Wald and Heaton (1994) using near-source, teleseismic, and geodetic data sets suggests that the average rupture speed was sub-Rayleigh. However, there are significant fluctuations, including a segment on the Camp Rock and Emerson fault segments that propagates at supershear speeds. Cohee and Beroza (1994), in their inversion, also fail to find evidence for supershear rupture, at least on average. They present several models for the inferred slip distribution for various average rupture speeds. The extreme variability between the models highlights a strong trade-off between heterogeneity in slip and rupture timing.

Several later studies examined this in more detail. In particular, Cotton and Campillo (1995) developed an inversion method in the frequency domain that places no restrictions on rupture speed. Building on this work, Hernandez et al. (1999) conducted a two-step inversion process for both slip and rupture timing. In the first step, they inverted synthetic aperture array (SAR) and global positioning

system (GPS) data for the final slip distribution on the fault. Then, taking this slip field as known, they inverted the near-source strong motion data for the rupture time, again using the frequency-domain method without restrictions on rupture speed. Their model shows a rupture process even more complex than inferred in previous studies. Strong variations in rupture speed were observed, but they make no explicit claim of supershear speeds.

Dynamic models do not place any constraint on rupture speed. An examination of the surface velocity field from the dynamic model of the Landers earthquake by Olsen et al. (1997) reveals a feature similar to a Mach front. This indicates that at least the apparent or along-strike phase velocity of the rupture locally exceeded the S-wave speed over sections of the fault. In some sense, the rupture process is similar to that described by Day (1982b) for heterogeneous faults, in which waves radiating ahead of the rupture trigger slip on weak patches ahead of the original front, causing apparent supershear speeds.

1999 Izmit and Duzce, Turkey

The Izmit and Duzce earthquakes were a bilateral events occuring within three months of each other. Rupture propagated at a supershear speed in one direction and at a sub-Rayleigh speed in the opposite direction according to the inversions of Bouchon et al. (2000, 2001). Evidence supporting the claim of supershear speeds

rests heavily on a single near-source accelerogram, for which only one horizontal component functioned properly. This station was located in the direction of supershear propagation and shows the abrupt arrival of large amplitude S waves immediately after the hypocentral P-wave arrival. No hypocentral S-wave arrival is evident. In contrast to this, the hypocentral S wave is clearly visible prior to the rupture front arrival at a station in the opposite direction, supporting the conclusion of sub-Rayleigh rupture speeds in this direction.

2001 Kunlunshan, China

Unlike the other earthquakes discussed here, the Kunlunshan event lacks near-source records due to its location in a remote section of the Tibetan plateau. Evidence of supershear speeds instead rests on analyses of regional and teleseismic data. Bouchon and Vallée (2003) matched regional waveform data, claiming that without supershear speeds, the major wave groups arrived too late at the stations. An analysis of teleseismic records by Antolik et al. (2004) also suggests an average rupture speed slightly higher than the S-wave speed.

2002 Denali Fault, Alaska

Near-source records from the Denali Fault earthquake (Ellsworth et al., 2004; Dunham and Archuleta, 2004) suggest locally supershear speeds over a section of

the fault near the Trans Alaska Oil Pipeline. A study of these records is presented in Chapter 7, so discussion will be deferred until then.

Chapter 3

Elastodynamic Framework

3.1 Governing Equations

The governing equation for an elastic solid is the convervation of momentum

$$\rho \frac{\partial^2 u_i}{\partial t^2} = \frac{\partial \sigma_{ij}}{\partial x_j}, \tag{3.1.1}$$

where ρ is the mass density and u_i and σ_{ij} are components of the displacement and stress fields. Repeated indices are summed. In general, the solid begins in an initially deformed state, characterized by some initial displacement and stress fields u_i^0 and σ_{ij}^0. Due to the linearity of the governing equation (3.1.1), we shall concern ourselves only with solving for the changes in these fields due to some source process. These changes are denoted without a superscript.

For this work, we shall assume that the material is isotropic, for which the stress-strain relation is

$$\sigma_{ij} = \lambda \delta_{ij} \epsilon_{kk} + 2\mu \epsilon_{ij}, \tag{3.1.2}$$

where ϵ_{ij} are components of the strain field and λ and μ are Lame's elastic constants, which we take to be uniform throughout the medium. Combining Eqns. (3.1.1) and (3.1.2) with the strain-displacement relationship,

$$\epsilon_{ij} = \frac{1}{2}\left(\frac{\partial u_i}{\partial x_j} + \frac{\partial u_j}{\partial x_i}\right), \tag{3.1.3}$$

yields the elastodynamic equation

$$\rho \frac{\partial^2 u_i}{\partial t^2} = \lambda \frac{\partial^2 u_j}{\partial x_i \partial x_j} + \mu \frac{\partial}{\partial x_j} \left(\frac{\partial u_i}{\partial x_j} + \frac{\partial u_j}{\partial x_i} \right). \tag{3.1.4}$$

The intial-boundary value problem approach to solving dynamic rupture problems involves specifying the initial values of the displacement and velocity fields (or their equivalents) everywhere within the solid, and possibly time-dependent boundary bonditions on any external surfaces or internal interfaces. These boundary conditions consist of three components of either displacement, traction, or some combination thereof, where traction is defined as

$$T_i = \sigma_{ij} n_j \tag{3.1.5}$$

for unit normal n_j to a surface.

3.2 Source Process

For simplicity, we shall assume that all inelastic material behavior occurs within a localized fault zone whose width is much smaller than any other length of interest. In this case, we treat the fault as an infinitesimally thin interface between two elastic solids. In this work, we shall assume that the fault is a planar interface, which we nominally take to be $z = 0$, although in later Sections dealing

with two-dimensional problems, the $y = 0$ plane will be used.

Certain components of the fields are discontinuous across the fault. In such a case, it is instructive to examine the structure of the momentum conservation equation across a surface of discontinuity within an elastic solid. The jump condition

$$[[\sigma_{ij} n_j + \rho V v_i]] = 0 \tag{3.2.1}$$

applies, where $v_i = \partial u_i / \partial t$ is the particle velocity and V is the speed of the surface in the direction of its normal n_i. The notation $[[\cdot]]$ denotes the difference of field values across the surface. We allow slip between the two sides of the fault, defined as

$$\Delta u_x = [[u_x]] \tag{3.2.2}$$

$$\Delta u_y = [[u_y]]. \tag{3.2.3}$$

The corresponding slip velocities are defined as

$$\Delta v_x = [[v_x]] \tag{3.2.4}$$

$$\Delta v_y = [[v_y]]. \tag{3.2.5}$$

For completeness, we also define the opening and opening velocity as

$$\Delta u_z = [[u_z]] \tag{3.2.6}$$

$$\Delta v_z = [[v_z]]. \tag{3.2.7}$$

For Eq. (3.2.1) to remain valid to first order in the fields, we set $V = 0$. This implies that the components of stress which give rise to tractions on the interface are continuous across it.

Boundary conditions are applied to the elastic solid on either side of the fault. Any variation in time of these conditions causes a change in the deformation of the surrounding material that is transmitted by elastic waves. Our objective throughout this work is to explore connections between physically motivated boundary conditions describing frictional and fracture processes and the resulting elastic wave excitations.

3.3 Elastic Waves

We shall now solve Eq. (3.1.4) using Fourier transform methods. The development in this Section closely follows that given by Willis (1973). Seeking a solution of the form

$$\exp[i(\mathbf{k}\cdot\mathbf{x}-\omega t)] \tag{3.3.1}$$

transforms Eq. (3.1.4) to

$$\rho\omega^2 u_i = \left[(\lambda+\mu)k_i k_j + \mu\delta_{ij}k_k k_k\right] u_j, \tag{3.3.2}$$

which is an eigenvalue equation for ω. The characteristic equation is

$$(\mu\mathbf{k}^2-\rho\omega^2)^2\left[(\lambda+2\mu)\mathbf{k}^2-\rho\omega^2\right]=0, \tag{3.3.3}$$

yielding three eigenvalues:

$$\omega = |\mathbf{k}|c_p \tag{3.3.4}$$

and

$$\omega = |\mathbf{k}|c_s, \tag{3.3.5}$$

repeated twice, where $c_p=\sqrt{(\lambda+2\mu)/\rho}$ is the P-wave speed and $c_s=\sqrt{\mu/\rho}$ is the S-wave speed. Eqns. (3.3.4) and (3.3.5) are the dispersion relations for waves in the bulk. The eigenvalues correspond to P waves and the two polarizations of S waves. The corresponding eigenvectors, denoted by capital U and normalized to unity, are

$$\mathbf{U}^P = \frac{1}{|\mathbf{k}|}\begin{pmatrix} k_x \\ k_y \\ k_z \end{pmatrix} \tag{3.3.6}$$

$$\mathbf{U}^V = \frac{1}{|\mathbf{k}|\sqrt{k_x^2+k_y^2}}\begin{pmatrix} -k_x k_z \\ -k_y k_z \\ k_x^2+k_y^2 \end{pmatrix} \tag{3.3.7}$$

$$\mathbf{U}^H = \frac{1}{\sqrt{k_x^2+k_y^2}}\begin{pmatrix} -k_y \\ k_x \\ 0 \end{pmatrix} \tag{3.3.8}$$

We label the P-wave eigenfunction with a superscript P and the S-wave eigenfunctions with superscripts V for the SV (shear vertical) polarization and H for the SH (shear horizontal) polarization. The degeneracy of the S waves allows us the freedom to align the two polarizations however we wish. We exploit this fact by constraining the particle motion of the SH waves to the lie in the plane of the fault.

It will be convenient to work in cylindrical coordinates in wave-number space. To this end, we define the magnitude of the interfacial wave number

$$k = \sqrt{k_x^2 + k_y^2}, \tag{3.3.9}$$

the propagation angle of the waves within the plane of the interface

$$\phi = \arctan(k_y/k_x), \tag{3.3.10}$$

and the phase velocity of the waves along the interface

$$c = \omega/k. \tag{3.3.11}$$

For notational convenience, we also define

$$\alpha_p = (1 - c^2/c_p^2)^{1/2} \tag{3.3.12}$$

and

$$\alpha_s = (1 - c^2/c_s^2)^{1/2}. \tag{3.3.13}$$

Eqns. (3.3.4) and (3.3.5) fix the magnitude of the z component of the wave number, and we make the following replacements:

$$k_x = k\cos\phi \tag{3.3.14}$$

$$k_y = k\sin\phi \tag{3.3.15}$$

$$k_z = \begin{cases} ik\alpha_p & \text{for } P \text{ waves} \\ ik\alpha_s & \text{for } S \text{ waves} \end{cases} \tag{3.3.16}$$

$$|\mathbf{k}| = \begin{cases} kc/c_p & \text{for } P \text{ waves} \\ kc/c_s & \text{for } S \text{ waves.} \end{cases} \tag{3.3.17}$$

The sign (or Reimann sheet, if we extend c to the complex plane) of the radicals appearing in Eqns. (3.3.12) and (3.3.13) is chosen such that the fields do not diverge as $z \to \pm\infty$. Our choice of sign is for the $z > 0$ half-space only, with the radical interpreted as giving a positive value for real c. Hereafter, unless otherwise noted, we shall restrict our attention to this upper half-space. Expressions for the fields in the lower half-space may be obtained by using symmetry conditions presented in Section 3.4. The eigenvectors for waves in the half-space $z > 0$, Eqns. (3.3.7)-(3.3.8), can be rewritten in these new coordinates as

$$\mathbf{U}^P = \frac{c_p}{c}\begin{pmatrix} \cos\phi \\ \sin\phi \\ i\alpha_p \end{pmatrix} \tag{3.3.18}$$

$$\mathbf{U}^V = \frac{c_s}{c}\begin{pmatrix} -i\alpha_s\cos\phi \\ -i\alpha_s\sin\phi \\ 1 \end{pmatrix} \tag{3.3.19}$$

$$\mathbf{U}^H = \begin{pmatrix} -\sin\phi \\ \cos\phi \\ 0 \end{pmatrix} \tag{3.3.20}$$

A general solution to Eq. (3.3.2) has the space and time dependence

$$\exp[ik(x\cos\phi + y\sin\phi - ct)], \tag{3.3.21}$$

and is a superposition of the eigenvectors:

$$u_i(k,c,\phi,z) = P(k,c,\phi)U_i^P e^{-k\alpha_p z} + \left[V(k,c,\phi)U_i^V + H(k,c,\phi)U_i^H\right] e^{-k\alpha_s z}, \tag{3.3.22}$$

where $P(k,c,\phi)$, $V(k,c,\phi)$, and $H(k,c,\phi)$ are the amplitudes of excited P, SV, and SH waves.

Associated with the deformation field described by (3.3.22) is a stress field. Of particular interest to us are the tractions exerted on the ($z > 0$ side of the) interface, which are readily obtained by combining Eqns. (3.3.19)-(3.3.20), (3.1.3), and (3.1.2):

$$T_i(k, c, \phi) = P(k, c, \phi)T_i^P + V(k, c, \phi)T_i^V + H(k, c, \phi)T_i^H, \tag{3.3.23}$$

where

$$\mathbf{T}^P = \mu k \frac{c_p}{c} \begin{pmatrix} 2\alpha_p \cos\phi \\ 2\alpha_p \sin\phi \\ i(1+\alpha_s^2) \end{pmatrix} \tag{3.3.24}$$

$$\mathbf{T}^V = \mu k \frac{c_s}{c} \begin{pmatrix} -i(1+\alpha_s^2)\cos\phi \\ -i(1+\alpha_s^2)\sin\phi \\ 2\alpha_s \end{pmatrix} \tag{3.3.25}$$

$$\mathbf{T}^H = \mu k \alpha_s \begin{pmatrix} -\sin\phi \\ \cos\phi \\ 0 \end{pmatrix}. \tag{3.3.26}$$

Note that the stresses on the interface are of the opposite sign, since the unit normal in this case is $-\mathbf{e}_z$.

3.4 Symmetry Conditions

At this point, we decompose the deformation field into two symmetry cases: tensile and shear. Tensile deformation has the following symmetries about $z = 0$:

$$\begin{aligned}
u_x(-z) &= u_x(z) \\
u_y(-z) &= u_y(z) \\
u_z(-z) &= -u_z(z) \\
\sigma_{xx}(-z) &= \sigma_{xx}(z) \\
\sigma_{xy}(-z) &= \sigma_{xy}(z) \\
\sigma_{xz}(-z) &= -\sigma_{xz}(z) \\
\sigma_{yy}(-z) &= \sigma_{yy}(z) \\
\sigma_{yz}(-z) &= -\sigma_{yz}(z) \\
\sigma_{zz}(-z) &= \sigma_{zz}(z). \qquad (3.4.1)
\end{aligned}$$

Shear deformation has the following symmetries about $z = 0$:

$$
\begin{aligned}
u_x(-z) &= -u_x(z) \\
u_y(-z) &= -u_y(z) \\
u_z(-z) &= u_z(z) \\
\sigma_{xx}(-z) &= -\sigma_{xx}(z) \\
\sigma_{xy}(-z) &= -\sigma_{xy}(z) \\
\sigma_{xz}(-z) &= \sigma_{xz}(z) \\
\sigma_{yy}(-z) &= -\sigma_{yy}(z) \\
\sigma_{yz}(-z) &= \sigma_{yz}(z) \\
\sigma_{zz}(-z) &= -\sigma_{zz}(z). \qquad (3.4.2)
\end{aligned}
$$

We only consider shear deformations. Combining the shear symmetry conditions (3.4.2) with the continuity of stress across the interface (3.2.1), we find that the two sides of the fault remain in perfect contact and that the normal stress is unaltered by shear deformations; i.e.,

$$[[u_z]] = 0 \qquad (3.4.3)$$

and

$$\sigma_{zz} = 0 \tag{3.4.4}$$

Eq. (3.4.4) is equivalent to $T_z = 0$. This condition is automatically satisfied by *SH* waves, which cause no changes to T_z. For the *P-SV* wave system, Eq. (3.4.4) fixes the relative amplitudes of P and SV waves by

$$T_z = T_z^P + T_z^V = 0 \tag{3.4.5}$$

or

$$V = -i\frac{c_p}{c_s}\frac{1+\alpha_s^2}{2\alpha_s}P. \tag{3.4.6}$$

Consequently the net traction on the interface is

$$T_i(k, c, \phi) = P(k, c, \phi)T_i^{PV} + H(k, c, \phi)T_i^H, \tag{3.4.7}$$

where $\mathbf{T}^H$ is given by Eq. (3.3.26) and

$$\mathbf{T}^{PV} = \mu k\frac{c_p}{c}\frac{R}{2\alpha_s}\begin{pmatrix} \cos\phi \\ \sin\phi \\ 0 \end{pmatrix}, \tag{3.4.8}$$

where

$$R = 4\alpha_s\alpha_p - (1 + \alpha_s^2)^2 \tag{3.4.9}$$

is the Rayleigh function. The Rayleigh function expresses the interference between P and SV waves, the relative amplitude of them such that the vanishing normal stress condition holds on the interface. At the Rayleigh speed, $c = c_R$, $R = 0$.

3.5 Response of the System to Traction Changes

As stated previously in Section 3.2, we shall view the earthquake source as some process which alters the shear traction on the interface, the occurrence of which generates slip. At this point, we shall examine the relationship between changes in shear traction and the resulting slip.

The expressions for the slip eigenvectors, obtained by combining the displacement eigenvector expressions, Eqns. (3.3.19)-(3.3.20), with the shear symmetry conditions, Eq. (3.4.2), are

$$\Delta\mathbf{U}^P = 2\frac{c_p}{c}\begin{pmatrix}\cos\phi\\ \sin\phi\\ 0\end{pmatrix} \tag{3.5.1}$$

$$\Delta\mathbf{U}^V = -2i\frac{c_s}{c}\alpha_s\begin{pmatrix}\cos\phi\\ \sin\phi\\ 0\end{pmatrix} \tag{3.5.2}$$

$$\Delta\mathbf{U}^H = 2\begin{pmatrix}-\sin\phi\\ \cos\phi\\ 0\end{pmatrix}, \tag{3.5.3}$$

and the total slip field is given by

$$\Delta U_i(k,c,\phi) = P(k,c,\phi)\Delta U_i^P + V(k,c,\phi)\Delta U_i^V + H(k,c,\phi)\Delta U_i^H. \tag{3.5.4}$$

An examination of the structure of the expressions for the tractions and slips, Eqns. (3.3.26), (3.4.8), and (3.5.2)-(3.5.3), reveals that the P and SV fields in the interfacial plane are orthogonal to the SH fields. Because of this, we define the fields associated with P and SV waves as the P-SV (or inplane) wave system, and those associated with SH waves as the SH (or antiplane) wave system. This division exists because the shear symmetry conditions on the interface (which

translate to a boundary condition on the normal stress) couple P and SV waves, but not SH waves.

At this point, we wish to examine the structure of the slip response for a given applied shear traction (as we view the earthquake source process). We shall consider the SH and P-SV wave systems separately, which is most easily accomplished by setting $\phi = 0$. In this case, the SH waves generate slip and traction only in the y direction, while the P and SV waves generate slip and traction only in the x direction. Combining Eqns. (3.5.2)-(3.5.3), (3.3.26), and (3.4.8) with $\phi = 0$ yields the following expressions:

$$\mu k \frac{\Delta U_x^P}{T_x^{PV}} = \frac{4\alpha_s}{R} \tag{3.5.5}$$

$$\mu k \frac{\Delta U_x^V}{T_x^{PV}} = -\frac{2\alpha_s(1+\alpha_s^2)}{R} \tag{3.5.6}$$

$$\mu k \frac{\Delta U_y^H}{T_y^H} = \frac{2}{\alpha_s} \tag{3.5.7}$$

These may be viewed as transfer functions, which are functions of the phase velocity c. The amplitude and phase of the response are shown in Fig. 3.1. These responses provide the underlying explanation for the allowed and forbidden rupture velocity regimes, as we discuss in the following Section.

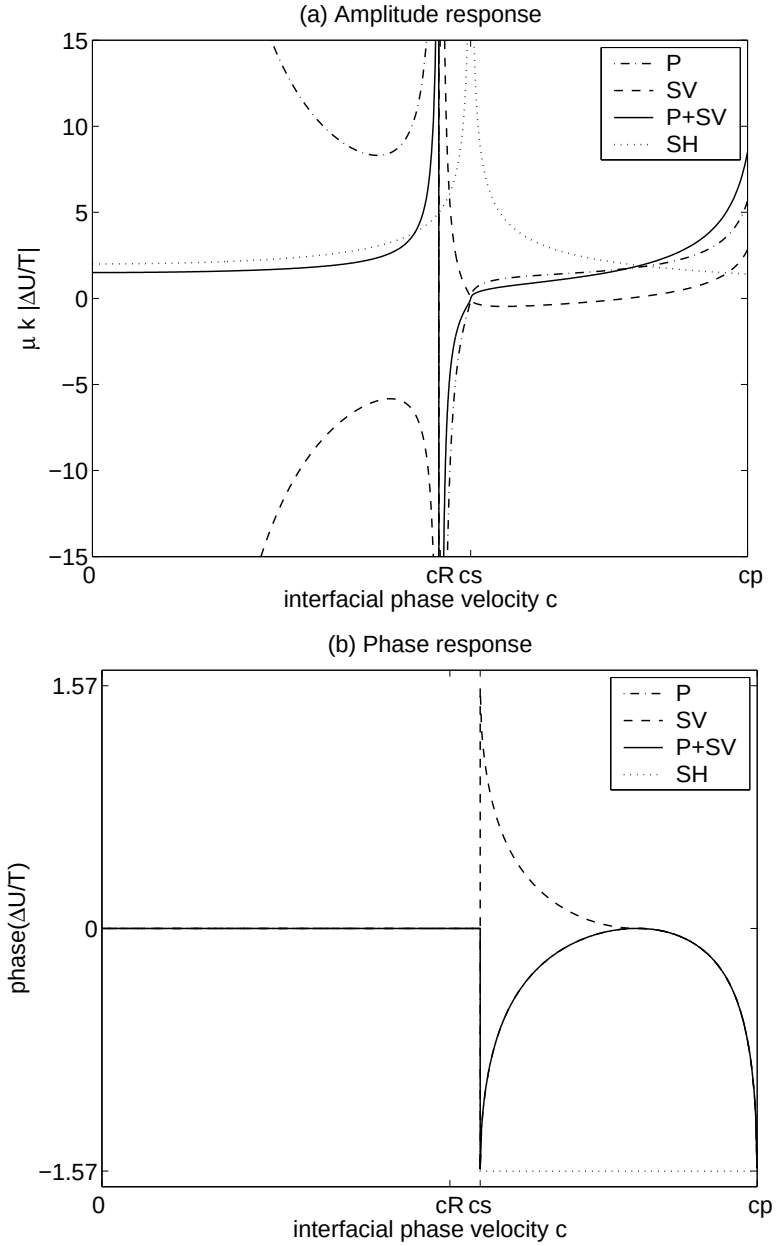

Figure 3.1: Amplitude (a) and phase (b) of the traction-slip transfer functions. The phase is restricted to lie between $-\pi/2$ and $\pi/2$, which introduces a sign to the amplitude. In (b), all lines overlap for $c < c_s$, and the lines denoting P and P+SV overlap for $c_s < c < c_p$.

3.6 Rupture Velocity Regimes

Many problems possess a further symmetry within the interfacial plane, the simplest example being problems having straight rupture fronts loaded either parallel to or perpendicular to the front. In these cases, the *P-SV* wave system remains decoupled from the *SH* wave system, even after taking into account interactions (i.e., diffraction or scattering) between waves and the rupture front. Coupling between the *P-SV* and *SH* wave systems occurs whenever this interfacial symmetry is broken. This occurs whenever the rupture front is curved, or even if it is straight, but with the loading inclined at an arbitrary angle with respect to it. Another example we shall consider in detail in Chapter 4 is the presence of friction on a sliding interface, which couples the *P-SV* and *SH* wave systems.

Two-dimensional rupture geometries occur when the rupture front is straight and the fields are invariant along it. Those in which only the *P-SV* wave system is excited are known as mode II and those in which only the *SH* wave system is excited are known as mode III. Slip is perpendicular to the rupture front for mode II and parallel to it for mode III.

The propagation velocity regimes for mode II and III ruptures follow from the information contained in Fig. 3.1, which characterizes the elastodynamic response of the medium. To obtain a valid solution for a propagating rupture, we need to

specify the source process. As discussed in Chapter 1, the only requirement that we make is that the fault slips due to a decrease in shear stress.

For mode III problems, only the *SH* wave system is excited. We see from Fig. 3.1 that slip occurs in the direction of the applied traction, with no phase shift in the response, for $c < c_s$. Thus, waves with phase velocities up to the *S*-wave speed drive the rupture forward. The limiting velocity is consequently c_s. Propagation velocities in excess of c_s are forbidden by causality (no *P* waves are excited in mode III). The amplitude of the slip response diverges as $c \to c_s$, which is the limit that the *SH* waves travel at grazing incidence with respect to the interface. In this case, they do not alter the shear traction.

The *P*-*SV* wave system drives mode II ruptures. Fig. 3.1 shows that the elastodynamic response changes across the Rayleigh speed and the *S*-wave speed. The static limit ($c \to 0$) displays an interesting feature: The amplitude response of the excited *P* and *SV* waves, considered separately, diverges (in opposite directions), but the combination remains finite. This reveals that elastostatic solutions consist of a precise balance between dilatational (*P*) and shear (*SV*) deformations.

For waves with interfacial phase velocities less than the Rayleigh speed, slip occurs in the direction of the applied traction, with no phase shift in the response (as in the mode III case). Waves in the sub-Rayleigh regime consequently promote rupture. There is a divergence in the amplitude of the slip response as $c \to c_R$.

This indicates that the particular combination of P and SV waves that propagate with phase velocity $c = c_R$ and satisfy the shear symmetry conditions (which keeps the normal traction unaltered) do not alter the shear traction. For frictionless interfaces, this feature manifests itself in the existence of Rayleigh interface waves.

As the phase velocity crosses the Rayleigh speed, the relative sign of slip and traction reverses. This is, in fact, a natural consequence of the existence of Rayleigh waves. In order for Rayleigh waves to exist, the tractions exerted by P and SV waves must precisely balance. However, there are no special velocities other than c_s and c_p at which the character of the waves (specifically the sign of the tractions exerted by them) will change. It thus follows that as the phase velocity crosses c_R (and the tractions come to a precise balance), the relative sign of slip and traction must reverse, at least until $c = c_s$. This is exactly what occurs, as Fig. 3.1 reveals. Waves with phase velocities between the Rayleigh and S-wave speeds thus attempt to halt the rupture process.

When the phase velocity crosses c_s, the S waves change from being evanescent to radiating, or in other words, from inhomogeneous to homogeneous. This introduces a phase shift in the traction-slip response. Slip returns to the same direction as the shear traction, and waves with intersonic phase velocities again promote rupture.

Of particular interest in this intersonic velocity regime is the speed $\sqrt{2}c_s$. As

Fig. 3.1 reveals, no S waves are excited by waves having this phase velocity. This fact plays an important role in character of the seismic radiation, as we discuss in Chapter 5.

3.7 Space-Time Expressions

Elastodynamic solutions in the space-time domain may be obtained by an appropriate superposition of plane waves. The Fourier integral theorem states that

$$u_i(\mathbf{x},t) = \frac{1}{8\pi^3}\int_{-\infty}^{\infty}\int_{0}^{2\pi}\int_{0}^{\infty} u_i(k,c,\phi,z)\exp[ik(x\cos\phi + y\sin\phi - ct)]dcd\phi k^2 dk \tag{3.7.1}$$

where

$$u_i(k,c,\phi,z) = \int_{-\infty}^{\infty}\int_{-\infty}^{\infty}\int_{-\infty}^{\infty} u_i(\mathbf{x},t)\exp[-ik(x\cos\phi + y\sin\phi - ct)]dxdydt. \tag{3.7.2}$$

The expansion of $u_i(k,c,\phi,z)$ into plane wave eigenvectors is given in Eq. (3.3.22).

In later Sections, we shall separate the contributions due to dilatational (P) and shear (SV plus SH) motions, labeling them as $\mathbf{u}^p$ and $\mathbf{u}^s$. It is easy to verify

that $\nabla \times \mathbf{u}^p = 0$ and $\nabla \cdot \mathbf{u}^s = 0$ using the expressions for the eigenvectors, Eqns. (3.3.7)-(3.3.8).

There are two particular classes of elastodynamic solutions that we investigate in this work: steady state and self-similar. Two-dimensional steady state solutions consist of fields that depend on x, y, and t only through the combination $x\cos\phi + y\sin\phi - Vt$, and physically correspond to propagation at the interfacial angle ϕ at constant speed V. In this case, the solution consists only of waves having phase velocities equal to the steady state velocity: $c = V$. Eq. (3.7.1) simplifies to

$$u_i(\mathbf{x}, t) = \frac{1}{2\pi}\int_{-\infty}^{\infty} u_i(k, V, \phi, z)\exp[ik(x\cos\phi + y\sin\phi - Vt)]k^2 dk. \qquad (3.7.3)$$

The self-similar case occurs when the problem lacks a characteristic length or time scale, such that the dependence on $\mathbf{x}$ and t enters only through $\mathbf{x}/t$ and t^n, in the sense that

$$u_i(\mathbf{x}, t) = t^n u_i(\mathbf{x}/t, 1). \qquad (3.7.4)$$

Such solutions are said to be homogeneous of degree n in $(\mathbf{x}, t)$. A similar relationship holds in the Fourier domain, leading to considerable simplification of the integrals in Eq. (3.7.1). This is the subject of Section 4.6.1.

Chapter 4

Excitation of Waves on Frictional Interfaces

This Chapter, essentially in this form except for changes in notation, appeared in:

> Dunham, E. M. (2005), Dissipative interface waves and the transient response of a three-dimensional sliding interface with Coulomb friction, *J. Mech. Phys. Solids*, 53, 327-357.

For consistency with this article, the interfacial phase velocity c will be designated as Ω.

4.1 Abstract

We investigate the linearized response of two elastic half-spaces sliding past one another with constant Coulomb friction to small three dimensional perturbations. Starting with the assumption that friction always opposes slip velocity, we derive a set of linearized boundary conditions relating perturbations of shear traction to slip velocity. Friction introduces an effective viscosity transverse to the direction of the original sliding, but offers no additional resistance to slip aligned with the original sliding direction. The amplitude of transverse slip depends on a nondimensional parameter $\eta = c_s\tau_0/\mu v_0$, where τ_0 is the initial shear stress, $2v_0$ is the initial slip velocity, μ is the shear modulus, and c_s is the S wave speed. As $\eta \to 0$, the transverse shear traction becomes negligible, and we find an azimuthally symmetric Rayleigh wave trapped along the interface. As $\eta \to \infty$, the

inplane and antiplane wave systems frictionally couple into an interface wave with a velocity that is directionally dependent, increasing from the Rayleigh speed in the direction of initial sliding up to the S wave speed in the transverse direction. Except in these frictional limits and the specialization to two dimensional inplane geometry, the interface waves are dissipative. In addition to forward and backward propagating interface waves, we find that for $\eta > 1$, a third solution to the dispersion relation appears, corresponding to a damped standing wave mode. For large amplitude perturbations, the interface becomes isotropically dissipative. The behavior resembles the frictionless response in the extremely strong perturbation limit, except that the waves are damped. We extend the linearized analysis by presenting analytical solutions for the transient response of the medium to both line and point sources on the interface. The resulting self-similar slip pulses consist of the interface waves and head waves, and help explain the transmission of forces across fracture surfaces. Furthermore, we suggest that the $\eta \to \infty$ limit describes the sliding interface behind the crack edge for shear fracture problems in which the absolute level of sliding friction is much larger than any interfacial stress changes.

4.2 Introduction

Boundaries of elastic solids are waveguides along which evanescent modes propagate. Boundary conditions couple the otherwise independently propagating P and S waves. In the case of a free surface, evanescent P and S waves interfere constructively to form the Rayleigh surface wave. Transient disturbances also excite head waves, in which trapped P waves convert to S waves that radiate away from the interface.

In a similar manner, trapped modes may exist along internal interfaces. A variety of possible interfacial conditions leads to an assortment of these waves. For welded contact between dissimilar materials, these are Stoneley waves, which exist as true trapped modes only for a particular range of material contrast (Stoneley, 1924; Cagniard, 1962). Frictionless interfaces (i.e., those for which the sides of the interface remain in contact, but offer no shear restoring tractions) support generalized Rayleigh waves. Achenbach and Epstein (1967); Weertman (1963) studied the existence of modes along such interfaces, which simplify to a pair of Rayleigh waves in the limit that the materials on either side become identical.

The addition of friction complicates the analysis. Even with simple Coulomb friction, to which we restrict our attention in this work, a rich variety of behaviors exist due to the nonlinearity of the system as it undergoes sticking and slipping

events. Much of the previous work has focused on stability properties of frictional sliding. As shown by Adams (1995), steady sliding between a dissimilar material pair under Coulomb friction is unstable with respect to two dimensional (2D) perturbations in the direction of the original motion for a wide variety of material pairs and frictional levels. The nature of this instability is related to the existence of the generalized Rayleigh waves, which cause changes in normal traction (Ranjith and Rice, 2001). The amplitude grows until the interface either sticks or opens. The problem lacks an intrinsic length scale, and there is consequently no bound on the growth rate of short wavelength perturbations. Ranjith and Rice (2001) proposed a regularization scheme based on experiments (Prakash and Clifton, 1993; Prakash, 1998) to fix this ill-posedness by introducing a finite time or length scale with which the system responds to changes in normal stress, providing a limit to how rapidly short wavelength perturbations grow. In the limit that the material pair becomes identical, slip perturbations are stable since they do not alter the normal traction. The solution reduces to the pair of Rayleigh waves found for frictionless contact, independent of the level of friction. From the perspective of a global energy balance, the energy lost as frictional heat is balanced by the additional strain energy associated with the higher level of initial stress. This independence is well known for 2D pure mode shear cracks (Freund, 1989; Broberg, 1999a).

In this work, we restrict our attention to an identical material pair, but extend the analysis to three dimensions (3D) by considering perturbations at an arbitrary angle with respect to the initial sliding direction. For most of the analysis, we restrict our attention to small perturbations under a linearized approximation. In this case, the overall direction of sliding is only slightly altered by the perturbation. In 3D, the vector nature of friction must be taken into account under the assumption that friction directly opposes the instantaneous sliding velocity. This issue was taken up by Cho and Barber (1999) in the context of a frictionally sliding mass elastically coupled to a driving force. Depending on the anisotropy of the coupling and the level of friction, sliding may be stable or unstable.

4.3 Problem Statement

Consider an infinite medium containing a planar interface at $z = 0$ and subject to an initial compressive $-\sigma_0$ and shear τ_0 load, where the x axis is aligned with the shear load and $\sigma_0 > 0$. The medium is isotropic and linear elastic, characterized by a shear modulus μ and P- and S-wave speeds c_p and c_s. For convenience, in this Chapter, we refer to the plane of the interface as horizontal, with the positive z axis extending vertically. Further assume that the two half-spaces are sliding relative to each other along the x axis with velocities $\pm v_0$, for $z > 0$ and $z < 0$,

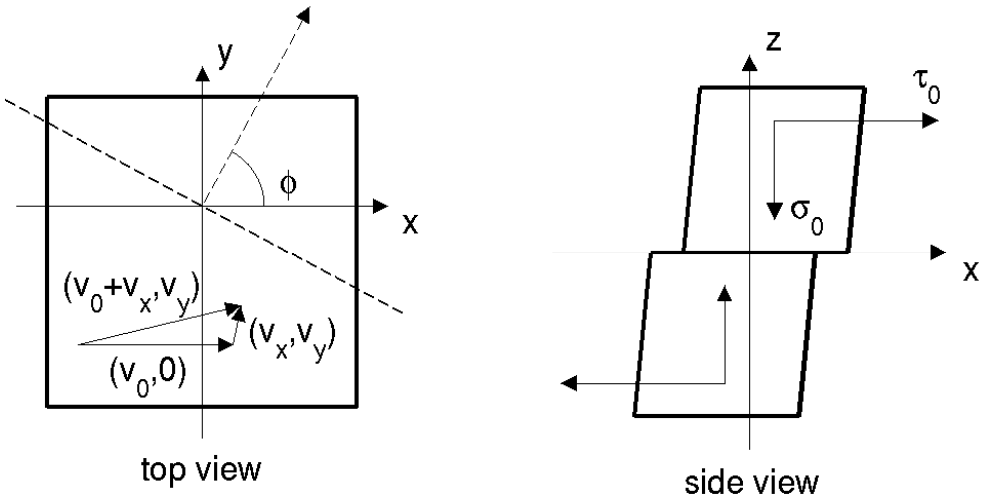

Figure 4.1: Model geometry showing the 3D nature of the problem. A small perturbation (v_x, v_y) about the steady state velocity v_0 is applied. We study these perturbations in the form of plane waves propagating at some angle ϕ with respect to the original sliding direction, as marked by the dashed lines in the top view.

under constant Coulomb friction $f = \tau_0/\sigma_0$. We introduce a perturbation to the system, and seek the response under the requirement that frictional resistance remains constant in magnitude but rotates to remain antiparallel to the local sliding velocity. A schematic diagram of the geometry is given in Fig. 4.1.

For simplicity, we write the boundary conditions for $z = 0^+$ only; a similar form holds for $z = 0^-$. Denoting the perturbation without a subscript and Cartesian unit vectors as $\mathbf{e}_x$ and $\mathbf{e}_y$, we write

$$\frac{(\tau_0 + \sigma_{xz})\mathbf{e}_x + \sigma_{yz}\mathbf{e}_y}{-\sigma_0 + \sigma_{zz}} = -f\frac{(v_0 + v_x)\mathbf{e}_x + v_y\mathbf{e}_y}{\sqrt{(v_0 + v_x)^2 + (v_y)^2}}. \tag{4.3.1}$$

Displacement components of the perturbation are denoted as u_i, particle velocities

as v_i, and stresses as σ_{ij}. Under the assumption that the perturbed fields are small with respect to the initial conditions, this linearizes to

$$(\frac{\sigma_{xz}}{\tau_0} + \frac{\sigma_{zz}}{\sigma_0})\mathbf{e}_x + \frac{\sigma_{yz}}{\tau_0}\mathbf{e}_y = \frac{v_y}{v_0}\mathbf{e}_y. \tag{4.3.2}$$

This assumption represents the main simplification in our study, limitations of which are discussed below. Perturbations to the slip velocity in the direction of the initial sliding decouple from perturbations to stress at first order. Instead, shear and normal stresses couple to maintain the required friction level in the original sliding direction.

This boundary condition may be further simplified by restricting ourselves to the specific class of problems in which slip is antisymmetric across the interface, which sustains a symmetric normal displacement that keeps the two sides in contact. As we have shown in Eq. 3.4.4, this symmetry sets $\sigma_{zz} = 0$. Since there is no change in the normal stress, $\sigma_{xz} = 0$. Of course, this symmetry assumption fails if the medium has some external boundary, for example, near the earth's surface for a dipping fault. Hereafter, we restrict our attention to the half-space $z \geq 0$.

The complete set of linearized boundary conditions we use in this study (with the exception of Section 4.7) is then

$$\begin{aligned} \sigma_{xz} &= 0 \\ \sigma_{yz}/\tau_0 - v_y/v_0 &= 0 \\ \sigma_{zz} &= 0. \end{aligned} \tag{4.3.3}$$

The transverse boundary condition introduces an effective viscosity set by the steady state conditions. We can compare the magnitude of the viscous traction increase to the instantaneous elastodynamic response of the interface to changes in slip velocity. Slip velocity perturbations are accompanied by the release of a pair of horizontally polarized S waves emitted normal to the interface, decreasing the shear traction (Brune, 1970; Rice, 1993). This radiation damping response is expressed in the transverse direction as $\sigma_{yz} = -\mu v_y/c_s$. Thus, we have two competing effects; the relative importance of them is captured by the nondimensional transverse viscosity parameter

$$\eta = c_s\tau_0/\mu v_0. \tag{4.3.4}$$

The special value of $\eta = 1$ corresponds to a precise balance between transverse shear traction decreasing due to radiation damping and increasing due to the effective viscous friction. As $\eta \to 0$, frictional resistance becomes negligible, the transverse boundary condition becomes $\sigma_{yz} = 0$, and the interface is effectively

frictionless with respect to the perturbations. For $\eta \to \infty$, friction dominates, the boundary condition becomes $v_y = 0$, and the interface is constrained to slip only in the original sliding direction. The small perturbation assumption actually fails in the strict $\eta \to \infty$ limit, since for finite τ_0 this implies that $v_0 \to 0$. However, so long as the perturbation amplitude is small enough that second order terms can be neglected, we find that the solution for any $\eta \gg 1$ is effectively identical to that obtained in the strict $\eta \to \infty$ limit.

For shear fracture problems, the value of η roughly measures the ratio of the absolute value of stress to the stress drop, which has qualitatively been shown to determine the amount of transverse slip (Madariaga, 1976; Day, 1982b; Spudich, 1992; Andrews, 1994; Guatteri and Spudich, 1998). This can be understood in the following manner. As a crack propagates along an originally locked interface with stress drop $\Delta\tau$ and sliding friction τ_0, particle velocities at the interface will be of order $v_0 \sim c_s \Delta\tau/\mu$, as required by radiation damping. This velocity will be somewhat uniform over an area on the sliding surface sufficiently removed from the crack edge, where much higher velocities are expected, provided that the rupture process has been relatively homogeneous. Forces are transmitted across this sliding surface by elastic waves, which are appropriately modeled as perturbations of a frictionally sliding interface. Such forces are generated, for example, by the failure of a small heterogeneity or by the extension of some

portion of the crack edge. Transverse resistance is parametrized with $\eta \sim \tau_0/\Delta\tau$, which is much greater than unity when $\Delta\tau \ll \tau_0$. It is consequently appropriate to consider the $\eta \to \infty$ limit under these conditions.

There are several limitations of this model. Our analysis describes the behavior of waves removed from the crack edge; impingement of these waves on the edge results in a complex set of diffractions that we do not consider. Furthermore, the amplitude of the perturbation must be small compared to the original sliding conditions for the linearized analysis to hold. We consider large amplitude perturbations later in this paper (Section 4.7), finding that for extremely strong perturbations the interface responds isotropically, as if frictionless except with the waves being damped. Finally, we have assumed that the original sliding rate is spatially uniform. If it instead varies, then our analysis will apply only to those components of the perturbed fields having a wavelength much smaller than the spatial variation length of the parameter η. In this case, the waves will adapt to the local value of η, as follows from the ideas developed by Woodhouse (1974) on surface wave propagation through regions of slowly varying properties.

This paper is organized in the following manner. The analysis begins by decomposing the elastodynamic response in terms of plane waves (Section 4.4). We continue in Section 4.5 with a study of the homogeneous (source-free) problem. We prove the existence of two nondispersive interfacial modes, similar to the Rayleigh

waves found along frictionless interfaces. The two modes correspond to forward and backward propagating waves, but are otherwise identical. Friction couples the inplane and antiplane wave systems, making the phase velocity dependent on the direction of propagation with respect to the original sliding direction. The effective viscous friction in the transverse direction damps the modes. For $\eta > 1$, a third root to the dispersion relation comes into existence, corresponding to a dissipative standing wave mode. In Section 4.6, we extend this analysis by solving for the transient response to point and line sources applied directly on the interface. The self-similar solutions are obtained using the method of Willis (1973). The solution consists of direct P and S waves, the interface waves studied in Section 4.5, and head waves resulting from P to S conversion along the interface. We conclude in Section 4.7 with a discussion of the fully nonlinear boundary conditions (4.3.1) for large amplitude perturbations.

4.4 Plane Wave Decomposition

Our analysis is carried out by representing the solution as a superposition of plane waves. This decomposition was discussed in detail in Chapter 3. The perturbations to the displacement and stress fields are given by Eqns. (3.3.19)-(3.3.20) and (3.3.25)-(3.3.26).

We keep k real and positive, but extend Ω to the complex plane as required by the Laplace transform. The branch cuts of the square roots lie in the complex phase-velocity plane such that $\Re\alpha_p > 0$, $\Re\alpha_s > 0$ for all Ω to satisfy the radiation condition at infinity (i.e., that all fields vanish as $z \to \infty$), consequently extending from c_p to ∞, $-c_p$ to $-\infty$ for α_p, and from c_s to ∞, $-c_s$ to $-\infty$ for α_s.

4.5 Interface Waves

Let us begin our analysis by studying the source-free problem with the set of boundary conditions defined in Eq. (4.3.3). Applying these boundary conditions yields a homogeneous system of equations. For a nontrivial solution to exist, the determinant of the coefficient matrix, given by

$$D(\Omega, \phi) = \zeta R + R\cos^2\phi + \alpha_s^2(1-\alpha_s^2)\sin^2\phi, \tag{4.5.1}$$

where $\zeta = \mathrm{i}\alpha_s c_s/\eta\Omega$ and $R = 4\alpha_s\alpha_p - (1+\alpha_s^2)^2$ is the Rayleigh function, must vanish. Since the problem lacks a characteristic length or time scale, the dispersion relation (4.5.1) is independent of k and the waves are nondispersive. As we shall show, Ω is complex except in certain limits, making the waves unstable if $\Im\Omega > 0$ or dissipative if $\Im\Omega < 0$. We note that if $D(\Re\Omega + \mathrm{i}\Im\Omega, \phi) = 0$, then $D(-\Re\Omega + \mathrm{i}\Im\Omega, \phi) = 0$ as well, corresponding to the equivalence of wave propagation in

either direction. In contrast to other problems, the roots do not occur in complex conjugate pairs.

The waves are dissipative and the sliding is stable to perturbations in all directions, except in special limits for which the waves are neutrally stable and nondissipative. Using the argument principle of complex analysis, we show that two roots always exist, and when the effective transverse viscosity becomes sufficiently large ($\eta > 1$) a third root comes into existence (as described in appendix A.1). We label this third root Ω_0 and the previous two $\Omega_\pm$.

4.5.1 Propagating Waves

First we concern ourselves with the two roots that always exist. A numerical solution of the dispersion relation shows that these roots lie in the stable region of the complex phase-velocity plane. They correspond to forward and backward propagating modes, and are a generalization of the Rayleigh waves that exist for frictionless contact.

Let us examine the condition for neutral stability. For this to occur, $\Im\Omega = 0$. Our solution is a superposition of evanescent P and S waves decaying exponentially away from the interface and has a phase velocity less than both wave speeds. Under these restrictions, the term of the dispersion relation (4.5.1) containing η is imaginary, while the remaining terms are real. Since both the real and imaginary

parts of this equation must separately be zero, a solution exists only if $\zeta R = 0$ and $R\cos^2\phi + \alpha_s^2(1-\alpha_s^2)\sin^2\phi = 0$. For arbitrary η, this is the case only when $\phi = 0$ or $\phi = \pi/2$. These correspond to the standard 2D inplane and antiplane loading geometries, respectively. As is well known, the inplane loading geometry supports interfacial Rayleigh waves (Achenbach and Epstein, 1967; Weertman, 1963, 1980). The antiplane solution is $\Omega = c_s$, showing that a horizontally polarized S wave may propagate at grazing incidence to the interface without altering any traction components. However, this does not correspond to a trapped wave, since its amplitude is independent of distance from the interface. In both of these geometrical limits, the coefficient of friction no longer enters into the elastodynamics of the problem, as occurs in the analytical solutions for 2D cracks (Freund, 1989; Broberg, 1999a).

For any other values of ϕ, we must place restrictions on η to obtain nondissipative modes. This occurs in the limiting cases $\eta \to 0$ and $\eta \to \infty$. As discussed earlier, the $\eta \to 0$ limit reduces the interface to a frictionless surface with respect to the perturbations. The antiplane wave system decouples from the inplane wave system, and we find two solutions to the dispersion relation, both independent of ϕ and the geometry of the loading system. The first, $\Omega = c_s$, is the antiplane solution like that found when $\phi = \pi/2$. The second solution occurs when $R = 0$, and the interface wave is the usual Rayleigh wave, as for the inplane loading geom-

etry. When $\eta \to \infty$, the antiplane wave system does not decouple and the phase velocity of the interface wave depends on the direction of propagation, increasing monotonically from the Rayleigh speed at $\phi = 0$ to the S wave speed at $\phi = \pi/2$, as shown in Fig. 4.2.

The particle motion for these modes is proportional to

$$\begin{aligned} u_x &\propto \cos\phi \left[\mathrm{e}^{-k\alpha_p z} - \frac{R + \alpha_s^2(1+\alpha_s^2)}{2\alpha_s^2} \mathrm{e}^{-k\alpha_s z} \right] \\ u_y &\propto \sin\phi \left[\mathrm{e}^{-k\alpha_p z} + \frac{\cot^2\phi R - \alpha_s^2(1+\alpha_s^2)}{2\alpha_s^2} \mathrm{e}^{-k\alpha_s z} \right] \\ u_z &\propto \mathrm{i}\alpha_p \mathrm{e}^{-k\alpha_p z} - \mathrm{i}\frac{1+\alpha_s^2}{2\alpha_s} \mathrm{e}^{-k\alpha_s z}, \end{aligned} \tag{4.5.2}$$

which is valid for arbitrary ϕ and η. We specifically focus on the interface waves in the $\eta \to \infty$ limit. Similar to Rayleigh waves, the motion is retrograde elliptical at the interface and prograde elliptical at depth. The depth at which the horizontal component goes to zero is roughly independent of ϕ. As ϕ increases, more of the inplane wave motion, which acts against the effective viscosity, converts to antiplane motion. This is illustrated in Figs. 4.3 and 4.4. For these, and all remaining plots, the material is a Poisson solid ($c_p = \sqrt{3}c_s$).

Except in the special limits discussed previously, the interface waves are dissipative. Fig. 4.5 shows the numerical solution of the dispersion relation (4.5.1). We see that the decay rate is most pronounced for $\eta \approx 1$ and ϕ approaching $\pi/2$.

These figures reveal an interesting feature, namely that the phase velocity can exceed the S wave speed within a certain region of parameter space. This occurs close to the region of maximum damping, but for larger η. Unlike the nondissipative cases discussed previously in which the fields exponentially decayed away from the interface with no oscillation (purely evanescent modes), extension to complex values of phase velocity introduces oscillations that modulate the exponential decay.

4.5.2 Damped Standing Wave

As shown in the previous Section, two roots of the dispersion relation (4.5.1) correspond to frictionally damped Rayleigh waves. Here we show that the third root, which comes into existence for $\eta > 1$ (see appendix A.1 for a proof of this), is a frictionally damped standing wave. As noted earlier, if $\Re\Omega + \mathrm{i}\Im\Omega$ is a solution, so is the backward propagating mode $-\Re\Omega + \mathrm{i}\Im\Omega$. It follows that for only one root to exist, it must be nonpropagating (i.e., $\Re\Omega = 0$). We restrict our search to the imaginary axis and again numerically solve the dispersion relation (4.5.1). Fig. 4.6 shows the dependence of $\Im\Omega$ on ϕ and η. The dissipation rate increases as η decreases and appears to diverge at $\eta = 1$, abruptly vanishing below this critical value.

We can understand the physical significance of $\eta = 1$ by comparing the effec-

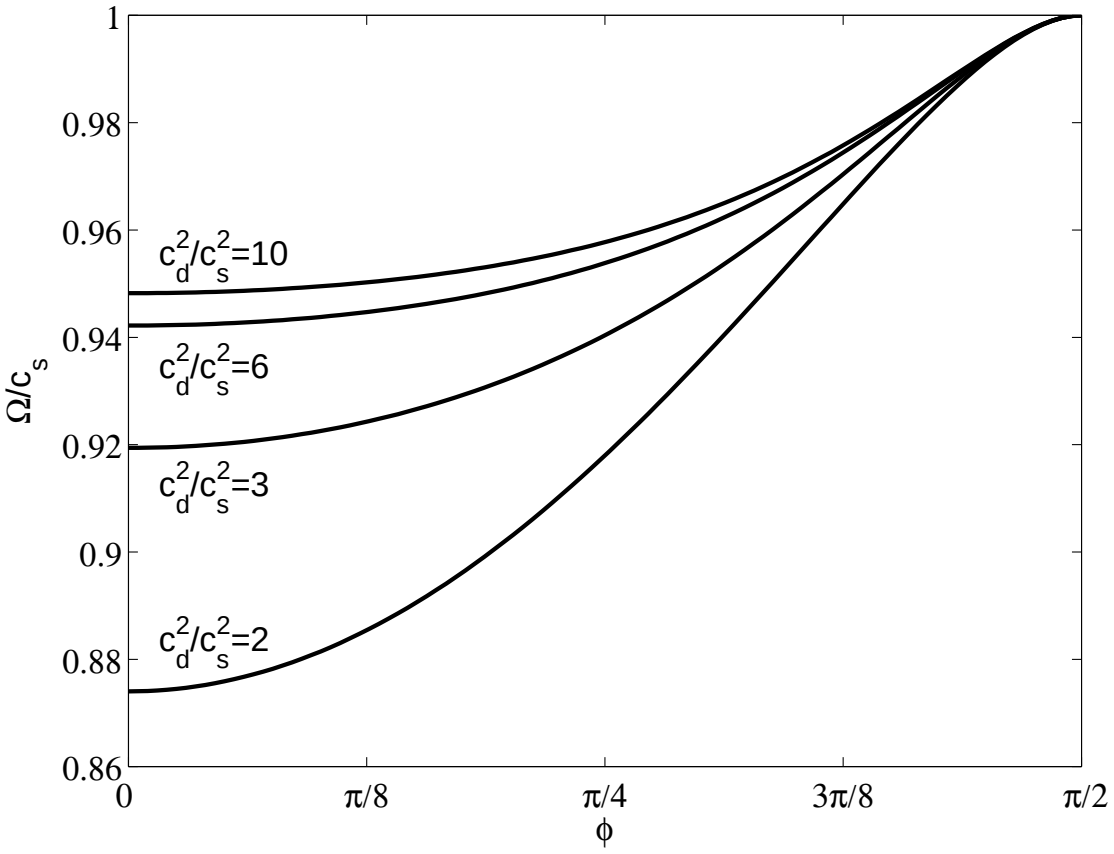

Figure 4.2: Interface wave speed as a function of azimuthal angle ϕ in the $\eta \to \infty$ limit. The speed at $\phi = 0$ corresponds to the Rayleigh wave speed for the material.

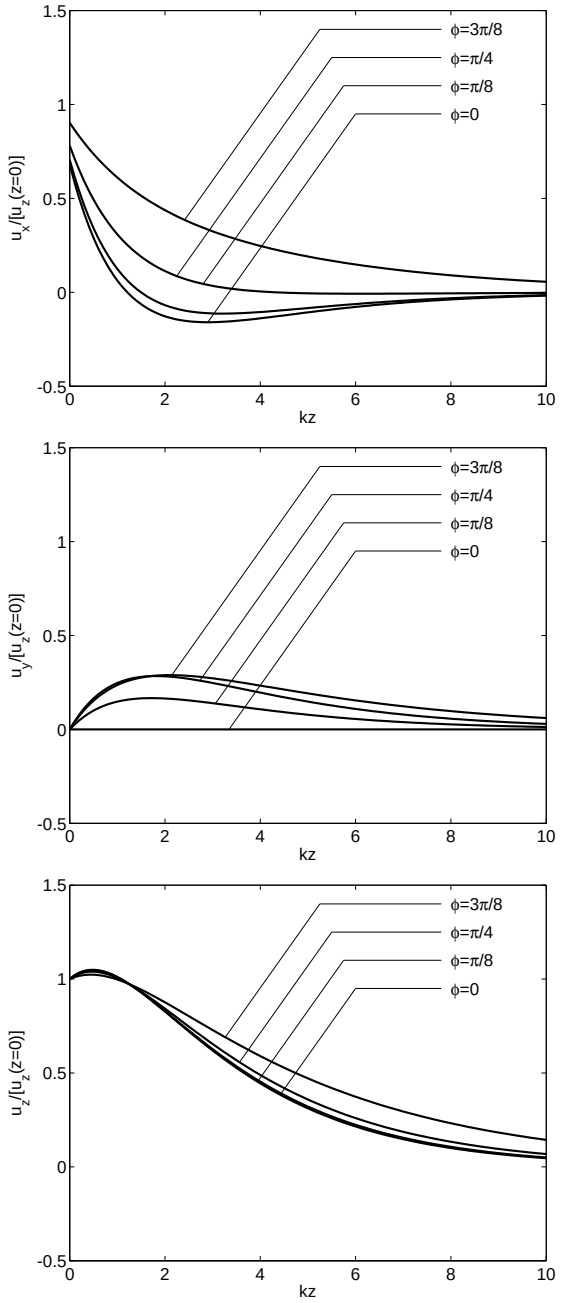

Figure 4.3: Displacement amplitudes, normalized by $u_z(z=0)$, as a function of distance from the interface in the $\eta \to \infty$ limit for various ϕ. At $\phi = \pi/2$, the interface wave becomes a purely antiplane S wave with amplitude independent of distance from the interface.

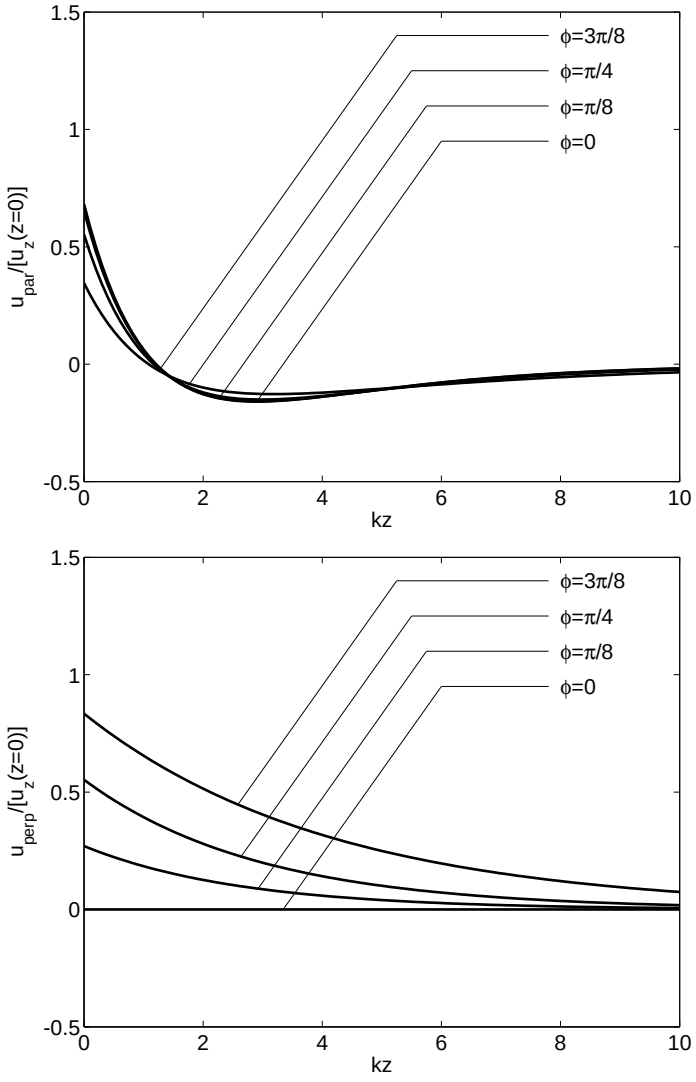

Figure 4.4: Horizontal displacement amplitudes, normalized by $u_z(z = 0)$, as a function of distance from the interface in the $\eta \to \infty$ limit for various ϕ. The fields are rotated to show the parallel (u_{par}) and perpendicular (u_{perp}) components, which would represent the inplane and antiplane wave systems in the free surface limit. As $\phi \to \pi/2$, the perpendicular component increases in amplitude, revealing the coupling between the wave systems.

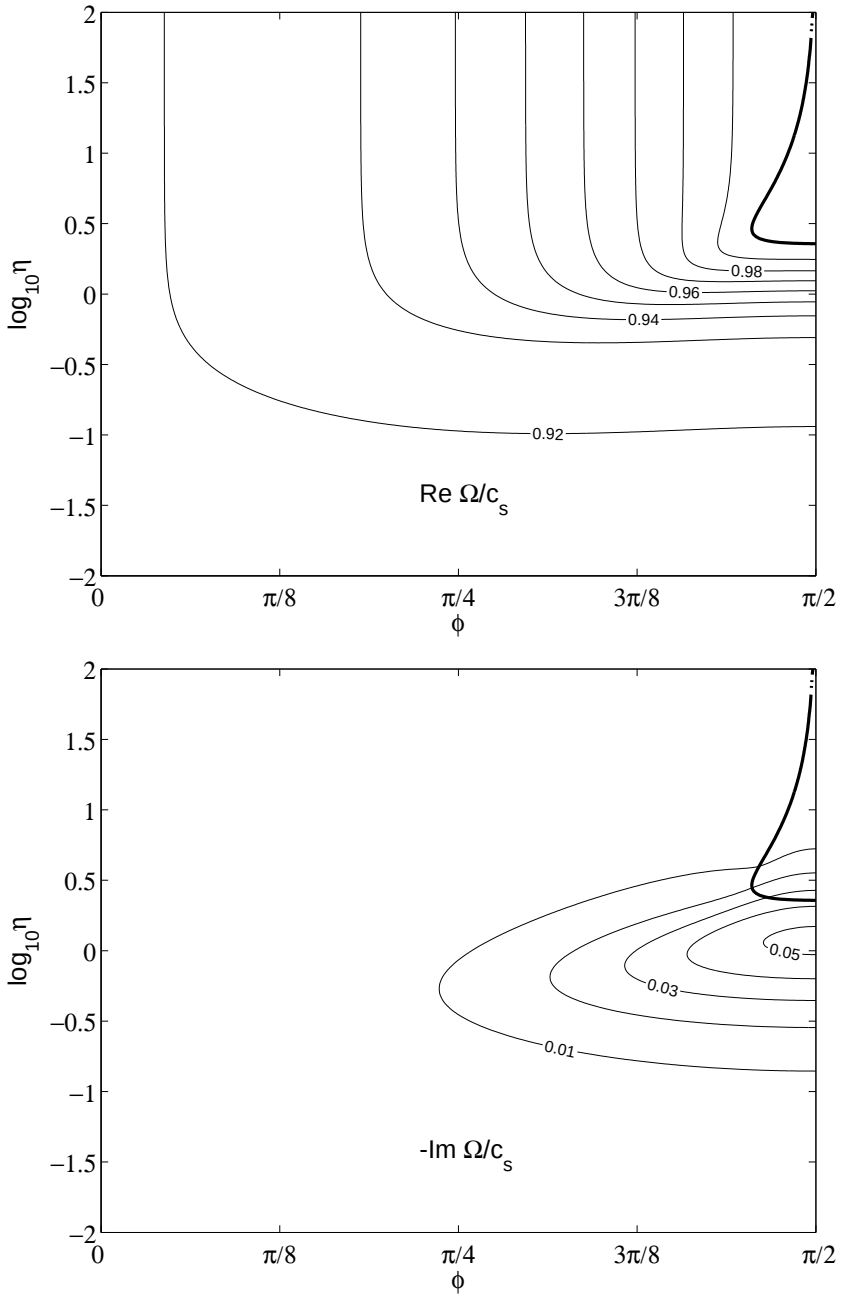

Figure 4.5: Real and imaginary parts of the phase velocity. The heavy contour delimits the boundary at which $\Re\Omega = c_s$; to the right of this, the waves have supershear phase velocities.

tive transverse viscosity to the instantaneous radiation damping response. This special value corresponds to an exact balance of radiation damping and friction. Increasing levels of friction ($\eta > 1$) force an instantaneous increase in transverse traction with transverse slip. A flow of energy from the steady state driving is required to satisfy this condition, resulting in a net dissipation within the system.

The decay rate is typically larger for this mode than for the two propagating modes, particularly when η is less than approximately 10. Consequently, it has little signature in the long-time response of the system to transient excitations, but does influence how rapidly the system decays into its asymptotic limit. We investigate this mode further in appendix A.2.

4.6 Transient Response

We now turn to the transient problem in which the interface is subject to an excitation in the form of point step-function stress drop of amplitude S (having units of force). The resulting displacement field serves as the Green function for a general time-dependent shear traction distribution on the interface. A similar solution was constructed by Harris and Day (1997) in their study of inplane shear cracks along a 2D bimaterial interface, and the application of the related solution for free surfaces to shear fractures is discussed by Richards (1979).

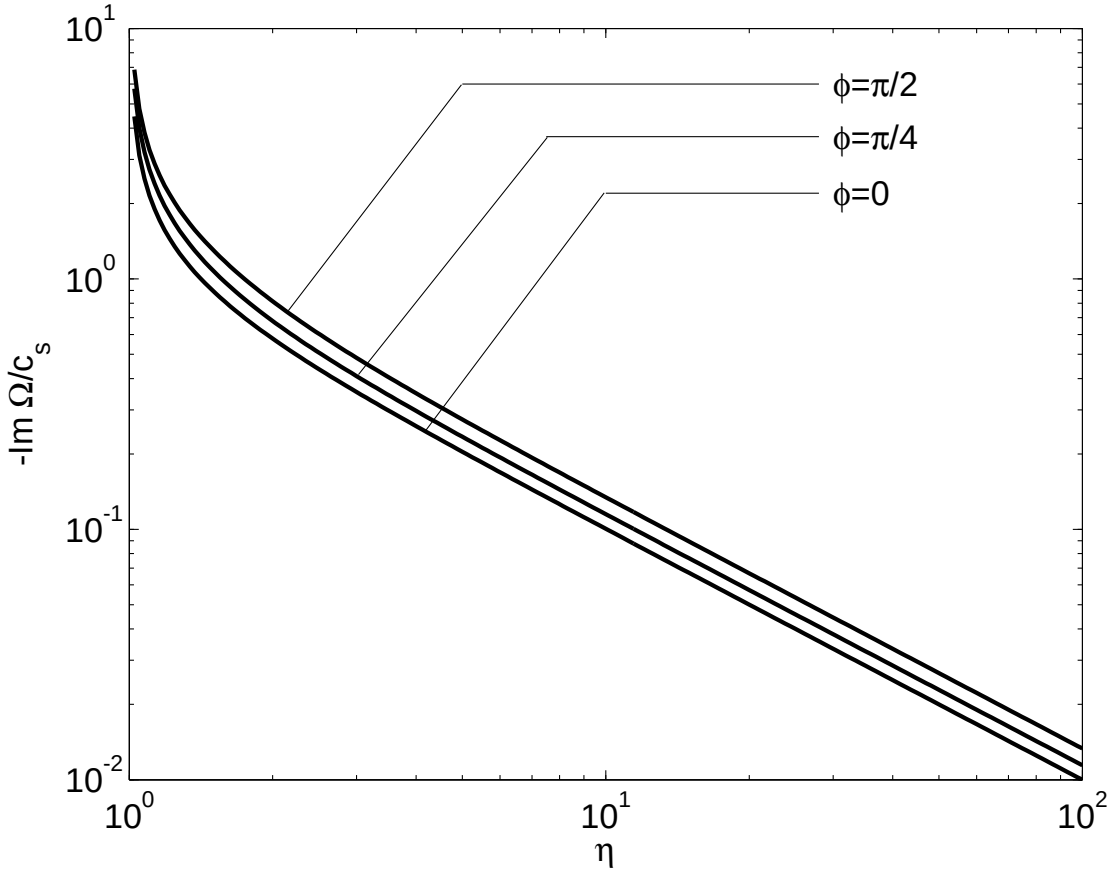

Figure 4.6: Dissipation rate for the standing wave mode as a function of η for various ϕ.

Our boundary conditions on the interface are now

$$\begin{aligned} \sigma_{xz} &= -SH(t)\delta(x)\delta(y) \\ \frac{\sigma_{yz}}{\mu} - \eta\frac{v_y}{c_s} &= 0 \\ \sigma_{zz} &= 0, \end{aligned} \tag{4.6.1}$$

where $H(\cdot)$ is the Heaviside step function and $\delta(\cdot)$ is the Dirac delta function. Applying the boundary conditions in Fourier-Laplace space yields

$$\begin{aligned} P &= -\frac{S}{\mu k^2 c_p D(\Omega,\phi)} 2\mathrm{i}\cos\phi(1+\zeta)\alpha_s \\ V &= -\frac{S}{\mu k^2 c_s D(\Omega,\phi)} \cos\phi(1+\zeta)(1+\alpha_s^2) \\ H &= \frac{S}{\mu k^2 \Omega D(\Omega,\phi)} \mathrm{i}\sin\phi[\zeta R + \alpha_s^2(1-\alpha_s^2)]. \end{aligned} \tag{4.6.2}$$

These results are used with the expressions (3.3.19) -(3.3.20)to find the dilatational and shear components of the displacement fields. For notational convenience, we write these as

$$u_i(\Omega,k,\phi,z) = \frac{S}{\mu k^2 \Omega D(\Omega,\phi)} \left[f_i^d(\Omega,\phi)\mathrm{e}^{-k\alpha_p z} + f_i^s(\Omega,\phi)\mathrm{e}^{-k\alpha_s z} \right], \tag{4.6.3}$$

where $i = x, y, z$. The relevant expressions are

$$
\begin{aligned}
f_x^d(\Omega,\phi) &= 2\mathrm{i}\cos^2\phi(1+\zeta)\alpha_s \\
f_x^s(\Omega,\phi) &= -\mathrm{i}\{\cos^2\phi(1+\zeta)\alpha_s(1+\alpha_s^2) - \sin^2\phi[\zeta R + \alpha_s^2(1-\alpha_s^2)]/\alpha_s\} \\
f_y^d(\Omega,\phi) &= 2\mathrm{i}\sin\phi\cos\phi(1+\zeta)\alpha_s \\
f_y^s(\Omega,\phi) &= -\mathrm{i}\sin\phi\cos\phi\{(1+\zeta)\alpha_s(1+\alpha_s^2) + [\zeta R + \alpha_s^2(1-\alpha_s^2)]/\alpha_s\} \\
f_z^d(\Omega,\phi) &= -2\cos\phi(1+\zeta)\alpha_s\alpha_p \\
f_z^s(\Omega,\phi) &= \cos\phi(1+\zeta)(1+\alpha_s^2). \qquad (4.6.4)
\end{aligned}
$$

4.6.1 Inversion of Transforms

To invert the transforms to the space-time domain, we use the inversion technique of Willis (1973). The Fourier-Laplace domain solution for any field is broken into dilatational and shear contributions. Only the inversion for the S wave term will be presented; the P term is similar. Writing this contribution as $U(\Omega,k,\theta)e^{-k\alpha_s z}$, the inversion formula can be written as

$$
\begin{aligned}
u(t,x,y,z) &= (2\pi)^{-3}\lim_{\epsilon\to 0}\int_{-\infty+\mathrm{i}0}^{\infty+\mathrm{i}0} d\Omega \int_0^{2\pi} d\theta \int_0^{\infty} dk k^2 \\
&\qquad U(\Omega,k,\theta)\exp[\mathrm{i}k(x\cos\theta + y\sin\theta - \Omega t) - k\alpha_s z - k\epsilon]. \qquad (4.6.5)
\end{aligned}
$$

The factor of $\mathrm{e}^{-k\epsilon}$ ensures convergence of the integral and becomes particularly

useful when evaluating a later result numerically. By virtue of the self-similarity of u (it is homogeneous of degree -2), we have $k^2U(\Omega,k,\theta) = U(\Omega,1,\theta)$. This permits us to evaluate the k integral to get

$$u(t,x,y,z) = \mathrm{i}(2\pi)^{-3}\lim_{\epsilon\to 0}\int_0^{2\pi} d\theta \int_{-\infty+\mathrm{i}0}^{\infty+\mathrm{i}0} d\Omega \frac{U(\Omega,1,\theta)}{x\cos\theta + y\sin\theta - \Omega t + \mathrm{i}\alpha_s z + \mathrm{i}\epsilon}. \tag{4.6.6}$$

The Ω integral can be evaluated by closing the contour with a semicircle at infinity in the upper half of the complex phase-velocity plane and using the residue theorem. We denote this path Γ. The poles of U lie on or below the real axis; hence, the only singularity of the integrand within the contour is possibly a pole from the denominator at $\Omega = \Omega_s$ where Ω_s is the solution to $\Omega_s t - X - \mathrm{i}(1-\Omega_s^2/c_s^2)^{1/2}z = \mathrm{i}\epsilon$ with $X = x\cos\theta + y\sin\theta$. This is recognized as the equation defining the well-known Cagniard path C, which is traditionally expressed in terms of the horizontal slowness or ray parameter Ω_s^{-1}, and physically corresponds to generalized ray arrivals. The relevant solution is

$$\Omega_s = \frac{t(X+\mathrm{i}\epsilon) + \mathrm{i}z\{t^2 - [(X+\mathrm{i}\epsilon)^2 + z^2]/c_s^2\}^{1/2}}{t^2 - z^2/c_s^2}; \tag{4.6.7}$$

the other root lies either outside Γ or on the Riemann sheet that does not satisfy the radiation condition.

The path of this pole through the complex phase-velocity plane occurs as follows, where the observer position (X, z) is assumed fixed and the path is parametrized by t. At $t = 0$, $\Omega_s = -c_s\sqrt{X^2+z^2}/z - i0$ below the real axis. As t increases to $t_s = z/c_s$, the pole moves left just below the real axis out to $\Omega_s = -\infty - \mathrm{i}0$. For t infinitesimally greater than t_s, Ω_s moves into the contour Γ at $\Omega_s = \infty + \mathrm{i}0$. The pole then moves to the left just above the real axis with increasing t until $t = \sqrt{X^2+z^2}/c_s$. At this point, $\Omega_s = c_s\sqrt{X^2+z^2}/X + \mathrm{i}0$. When inverting for the P wave contribution, this is always to the right of the rightmost branch point. For the S wave contribution, however, this path crosses the P wave branch point when $c_s\sqrt{X^2+z^2}/X = c_p$, which defines the locus of observer positions at which head waves begin to appear. At this point, the pole leaves the real axis and moves up and to the left until $\Im\Omega_s$ reaches a maximum at $t = \sqrt{2X^2+z^2}/c_s$ and $\Omega_s = (\sqrt{2X^2+z^2} + \mathrm{i}z)c_s/2X$. The pole then begins approaching the origin, asymptotically following the path $\Omega_s = (X + \mathrm{i}z)/t$ as $t \to \infty$. Fig. 4.7 shows the section of the path within Γ.

Use of the residue theorem to evaluate the Ω integral forces us onto this path, leaving

$$u(t,x,y,z) = \frac{1}{4\pi^2}\int_0^{2\pi} d\theta \frac{U(\Omega_s,1,\theta)H(t-t_s)}{t + \mathrm{i}z\frac{\Omega_s}{c_s^2}(1-\frac{\Omega_s^2}{c_s^2})^{-1/2}}. \tag{4.6.8}$$

This remaining integral, physically corresponding to a superposition of 2D solu-

tions at azimuthal angle θ, must be performed numerically.

We can also extract the 2D response to a line force using the 3D formula. We rotate our system of coordinates (x, y) in the plane of the interface by the angle ϕ to (x', y'). The force is still applied along the x-axis, but the solution is now independent of y' (i.e., the boundary condition $\sigma_{xz} = -SH(t)\delta(x)\delta(y)$ is replaced by $\sigma_{xz} = -SH(t)\delta(x')$, where S now has units of force/length). The 2D limit in the Fourier-Laplace domain is obtained by multiplying the 3D solution by $2\pi\delta(k_{y'})$, which changes the degree of homogeneity of the displacement field to -1. We thus invert instead for the velocity field, which is given by $V(\Omega, k, \theta) = -2\pi \mathrm{i}\Omega k^{-2}\delta(k_{y'}/k)U(\Omega, 1, \theta)$, where U is the 3D solution for the point force.

Inserting this into Eq. (4.6.8) (replacing displacement with velocity) collapses the azimuthal integral. The two contributions occur when $\theta = \phi$ and $\theta = \phi + \pi$, which are complex conjugates of each other. Hence,

$$v(t, r, z) = \frac{1}{\pi}\Im\frac{\Omega_s U(\Omega_s, 1, \phi)H(t - t_s)}{t + \mathrm{i}z\frac{\Omega_s}{c_s^2}(1 - \frac{\Omega_s^2}{c_s^2})^{-1/2}}, \tag{4.6.9}$$

where $r = \sqrt{x^2 + y^2}$ replaces X in Eq. (4.6.7).

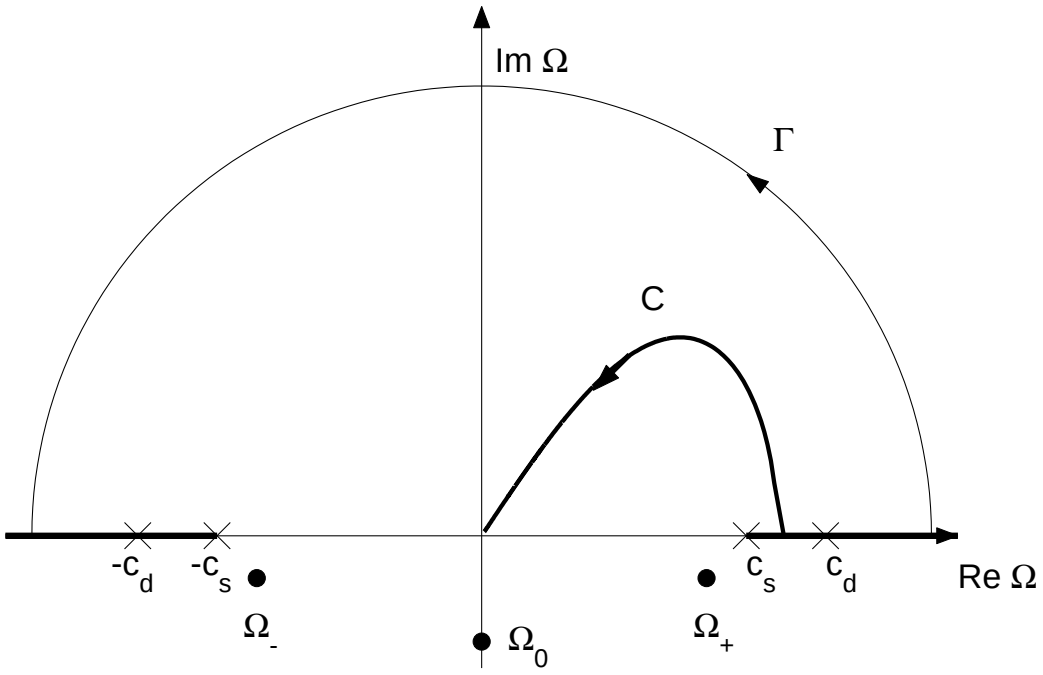

Figure 4.7: Representation of the integration contour Γ and the Cagniard path C in the complex phase-velocity plane. Branch points, branch cuts, and interface wave poles are also shown. The Cagniard path encounters the P wave branch point if the observation point lies within the region where head waves are present.

4.6.2 Line Source

We present the results of the line source first, which do not require any integration to compute. The pattern of wavefronts for a frictionless interface is shown in Fig. 4.8. Four arrivals occur for the inplane geometry. These are the cylindrical dilational and S wavefronts, the Rayleigh wave, and head waves. In the antiplane geometry, only the cylindrical S wavefront exists. For $z \geq 0$, particle velocities are obtained using Eqs. (4.6.3) and (4.6.9) as

$$v_i(t,r,z) = \frac{S}{\mu\pi}\Im\Bigg[\frac{f_i^d(\Omega_p,\phi)H(t-z/c_p)}{D(\Omega_p,\phi)[t+\mathrm{i}\frac{\Omega_p}{c_p^2}(1-\frac{\Omega_p^2}{c_p^2})^{-1/2}z]} + \frac{f_i^s(\Omega_s,\phi)H(t-z/c_s)}{D(\Omega_s,\phi)[t+\mathrm{i}\frac{\Omega_s}{c_s^2}(1-\frac{\Omega_s^2}{c_s^2})^{-1/2}z]}\Bigg] \tag{4.6.10}$$

with the f_i given in Eq. (4.6.4). There are two limits in which the solutions are independent of η; these occur when $\phi = 0$ and $\phi = \pi/2$, corresponding to pure inplane and pure antiplane geometries for which the solution to our problem is well known. For mixed-mode cases the dependence on η emerges, as shown in Fig. 4.9. The four wave arrivals characteristic of the inplane free surface are slightly modified, with the interface wave discussed previously taking the place of the Rayleigh wave.

We have verified these 2D results using the spectral boundary integral methodology proposed by Geubelle and Rice (1995) to calculate the interfacial particle

velocity. Results are computed using 512 spatial grid points with the point force distributed over the central two nodes, and the interfacial friction obeying the linearized boundary condition (4.3.3). Fig. 4.10 shows agreement between the numerical and analytical solutions for $\phi = \pi/4$ and variable η. Small values of η, approaching the frictionless limit, show a distinct separation between S and Rayleigh wave arrivals resulting from the independent propagation of the inplane and antiplane wave systems. As η increases, the increasing transverse resistance couples the antiplane wave system into the interface wave, which dominates the arrivals.

4.6.3 Point Source

For the 3D point force problem, the displacement fields are obtained using Eqs. (4.6.3) and (4.6.8) as

$$u_i(t,x,y,z) = \frac{S}{4\mu\pi^2}\int_0^{2\pi} d\theta \Bigg[\frac{f_i^d(\Omega_p,\theta)H(t-z/c_p)}{\Omega_p D(\Omega_p,\theta)[t+\mathrm{i}\frac{\Omega_p}{c_p^2}(1-\frac{\Omega_p^2}{c_p^2})^{-1/2}z]} + \frac{f_i^s(\Omega_s,\theta)H(t-z/c_s)}{\Omega_s D(\Omega_s,\theta)[t+\mathrm{i}\frac{\Omega_s}{c_s^2}(1-\frac{\Omega_s^2}{c_s^2})^{-1/2}z]}\Bigg], \quad (4.6.11)$$

Figs. 4.11 and 4.12 show the displacement fields at $z = 0$. Again, the analytical solutions are verified numerically with a boundary integral solution. In this case, only 256 grid points were used in each direction, with the point force distributed

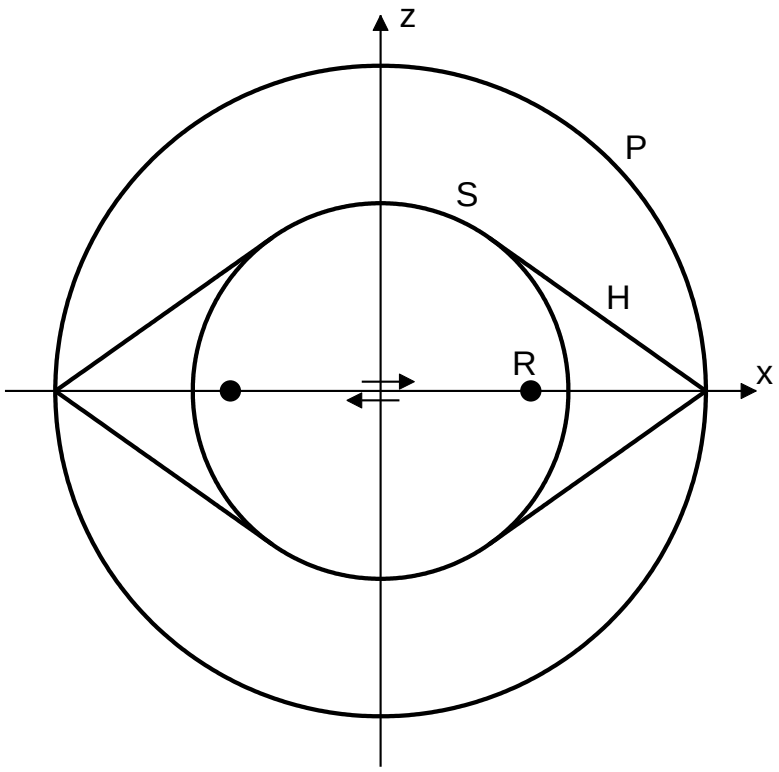

Figure 4.8: Wavefronts radiating from a line stress drop through the origin for a frictionless interface at $z = 0$ in inplane geometry. P and S denote the cylindrical P and S waves, R is the Rayleigh wave, and H is the S head wave excited by evanescent P waves along the interface. For the antiplane geometry, only the S wave is present.

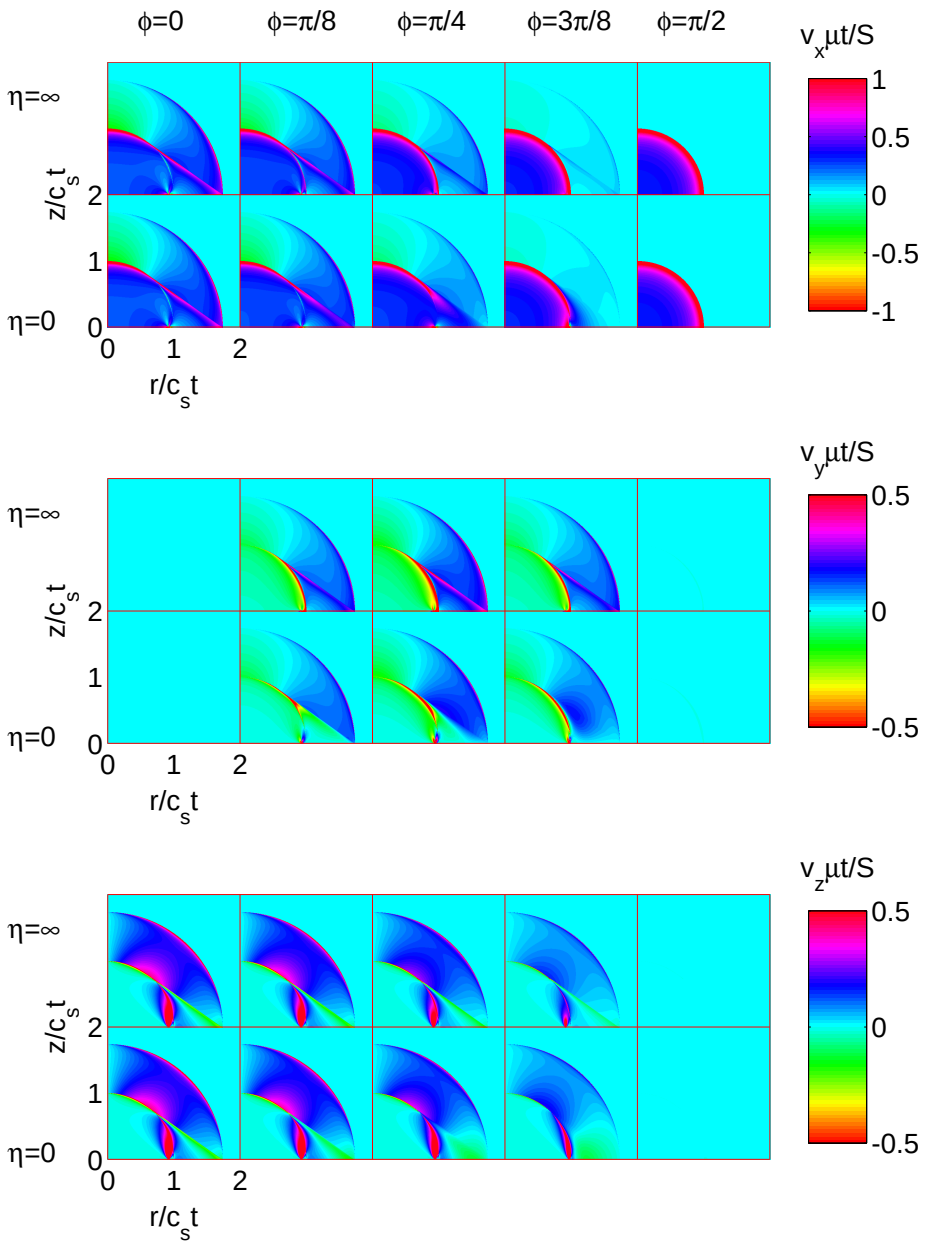

Figure 4.9: Particle velocities for a 2D line source with step-function time dependence for various ϕ and η. A comparison with the wavefronts generated along a frictionless interface (Fig. 4.8) reveals that increasing η couples the inplane and antiplane wave systems. This is particularly evident at intermediate angles close to the interface.

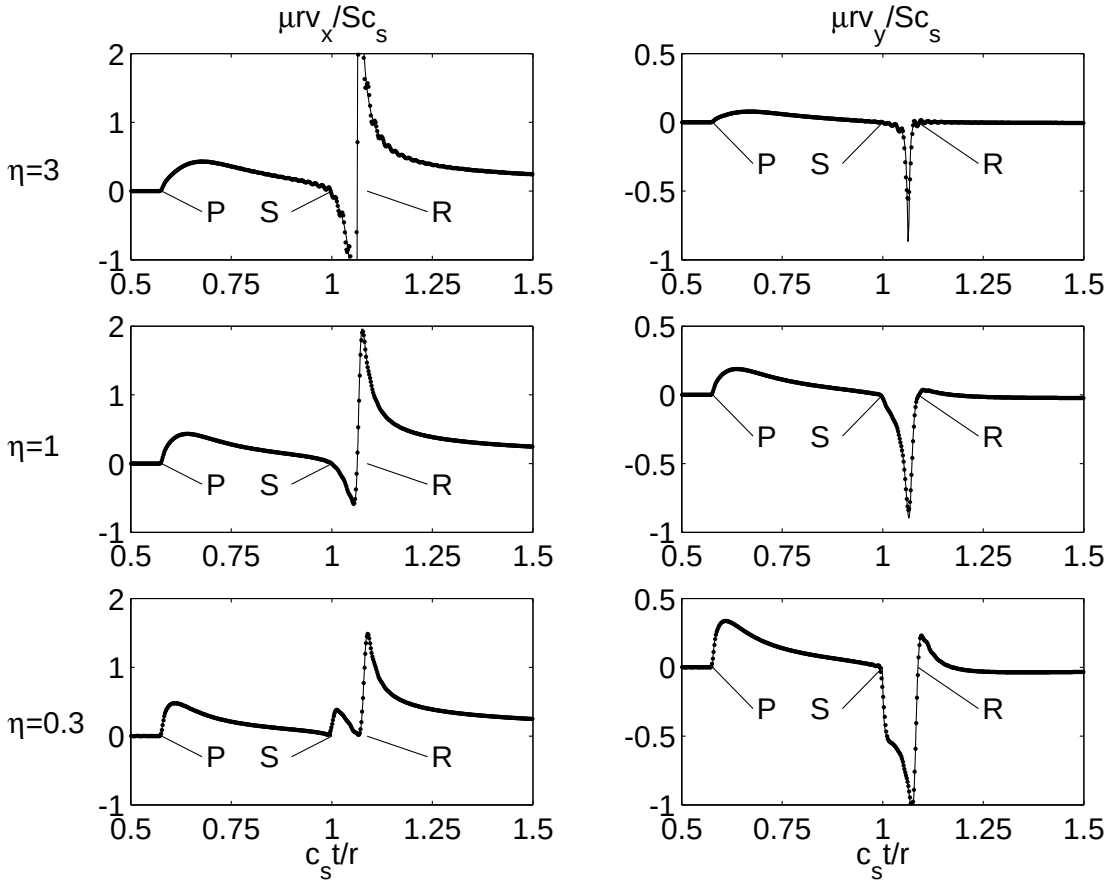

Figure 4.10: Interfacial particle velocities for a 2D line source with step-function time dependence for $\phi = \pi/4$ and various η. The solid line is the analytical solution; the points are computed using a boundary integral methodology. Wave arrivals are labeled as in Fig. 4.8. At this angle, the coupling between the inplane and antiplane wave systems is most evident. For small η, the S and Rayleigh arrivals are distinctly separated. As η increases, the wave systems couple and these arrivals merge into a single interface wave.

over the central four nodes.

The nature of the 3D solution as a superposition of 2D plane waves is evident. For small values of η, antiplane S waves increasingly decouple from the inplane solution and separate arrivals at the S and Rayleigh speeds appear. As η increases, the waves coalesce into the direction-dependent interface wave that appeared during the study of the homogeneous problem. These waves carry the static displacement field for the x and y-components on the interface. In contrast, the vertical component shows a gradual approach to the static solution. In addition to the interface waves, head waves begin at the P wave arrival. Increasing η focuses more energy into the head waves.

4.7 Nonlinear Effects

Our investigation has thus far been limited to the assumption that the perturbations are small enough that the linearization of Eq. (4.3.1) to Eq. (4.3.3) is valid. Departures from the linearized friction law will be most pronounced near the interface wave arrival, where the largest amplitudes of slip velocity occur. The point and line force solutions investigated previously are singular at the arrival of the interface wave, consequently violating the small amplitude assumption. Of course, these solutions should be used in the context of constructing a finite

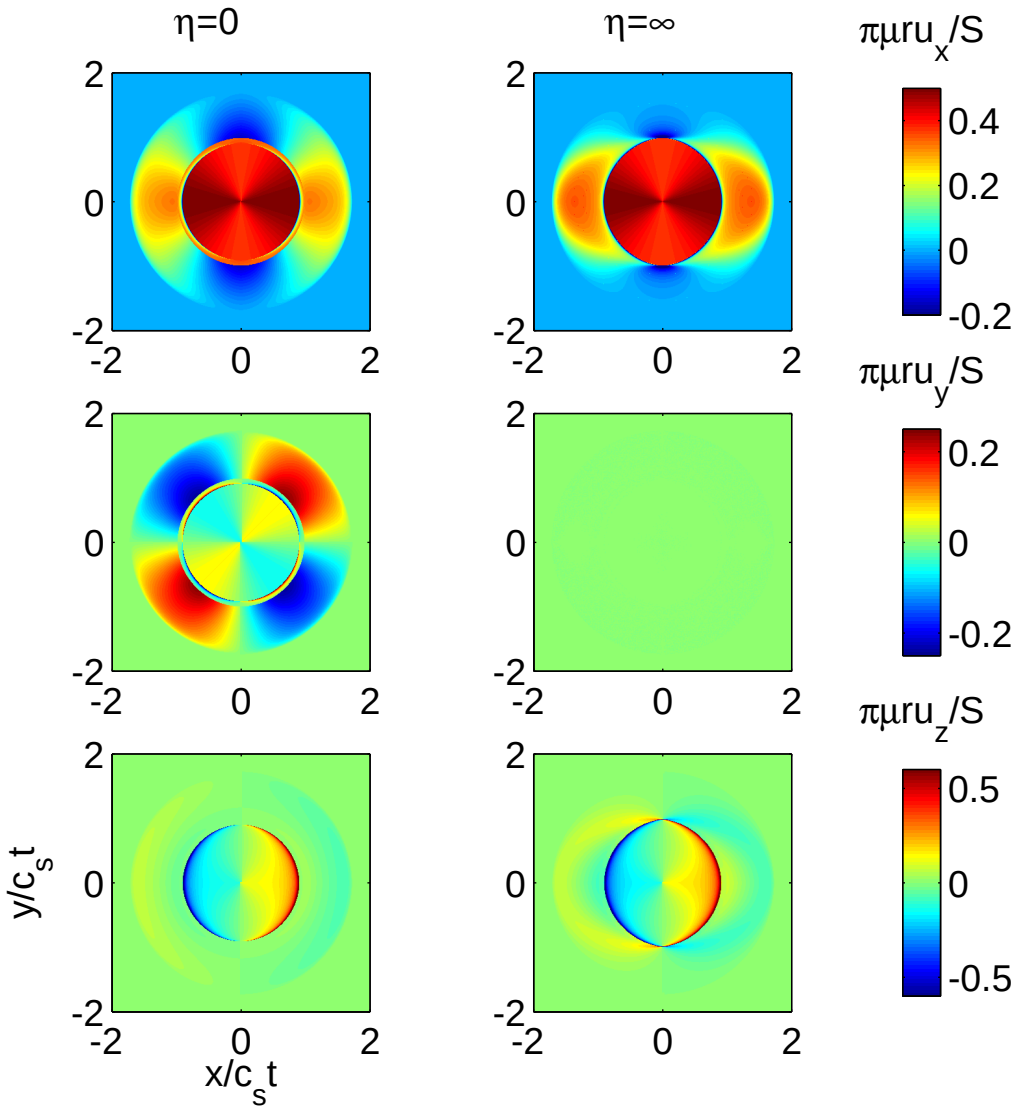

Figure 4.11: Interface displacement for a 3D point source at the origin with step-function time dependence. In the $\eta \to \infty$ limit, the head wave pattern elongates along the original sliding direction, as seen for u_x and u_z. A close examination of the figures, particularly u_x, shows that two distinct S and Rayleigh wavefronts exist for $\eta \to 0$, while only one wavefront, corresponding to the directionally dependent interface wave, appears as $\eta \to \infty$.

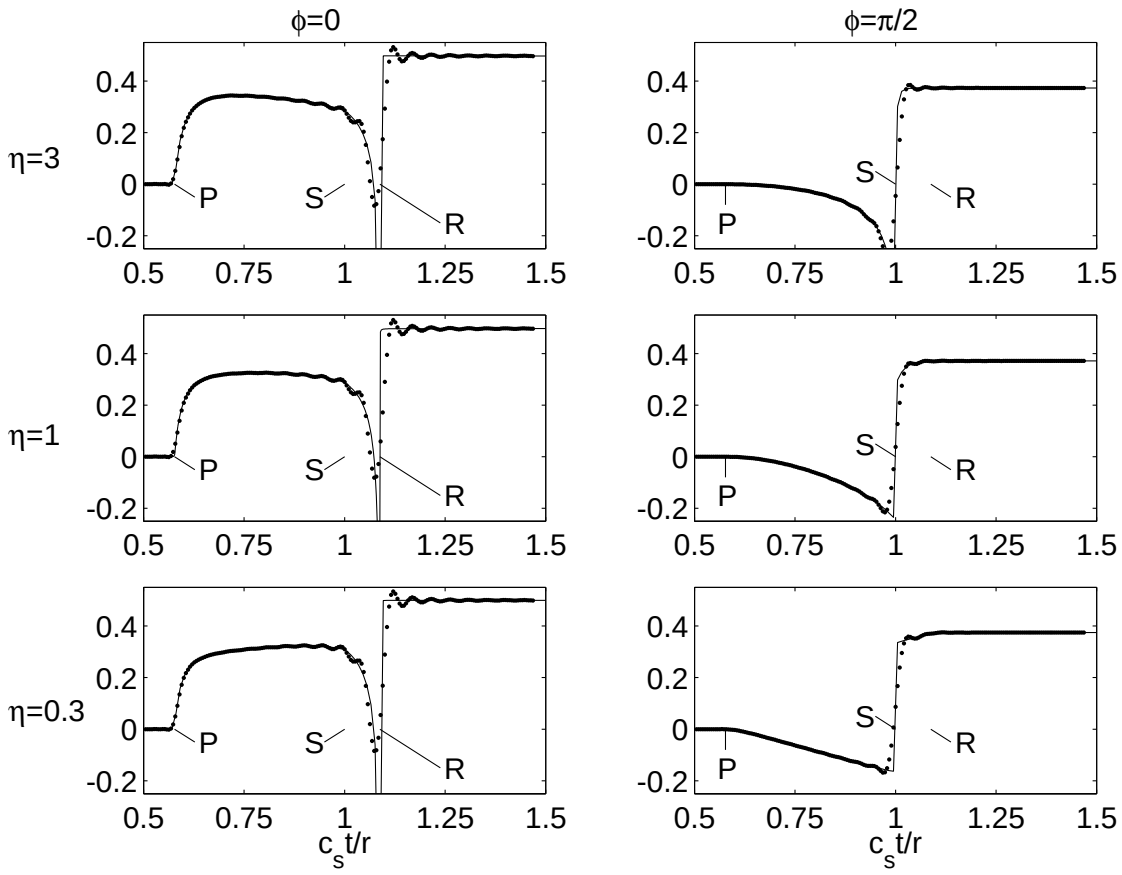

Figure 4.12: Interfacial displacement history $\mu\pi r u_x/S$ for a 3D point source with step-function time dependence for various ϕ and η. The solid line is the analytical solution; the points are computed using a boundary integral methodology. Wave arrivals are labeled as in Fig. 4.8. In contrast to intermediate angles (Fig. 4.10), the effect of varying η is more subtle in these standard inplane and antiplane directions.

source by superposition, which renders the linear analysis valid for sufficiently small amplitude sources of sufficient extent.

To study the nonlinear problem, we consider applying a large perturbation $\sigma_{xz}^{\text{load}} \gg \tau_0$. The corresponding velocities at the interface will be much larger than v_0, which we consequently neglect. In this case, the shear boundary conditions reduce to

$$\begin{aligned} \tau_0 + \sigma_{xz} &= \tau_0 \frac{v_x}{\sqrt{v_x^2 + v_y^2}} \\ \sigma_{yz} &= \tau_0 \frac{v_y}{\sqrt{v_x^2 + v_y^2}}. \end{aligned} \tag{4.7.1}$$

The response is now isotropically dissipative, with the total shear traction vector aligned antiparallel to the slip velocity perturbation, irrespective of the initial sliding direction. Because of the isotropy, we expect the response to be similar in nature to the frictionless response, except that the perturbations will be damped. The dissipation rate will increase with perturbation amplitude, since slip velocities will increase while the magnitude of the total shear traction remains equal to τ_0.

Having established the accuracy of our numerical methodology in the previous Sections by comparison to our analytical solutions, we are in the position to test our ideas by applying perturbations of arbitrary amplitude with the nonlinear boundary condition (4.3.1). For simplicity, we restrict ourselves to 2D and

consider the step function application of a spatially distributed shear load in the x-direction having a gaussian shape, i.e., $\sigma_{xz}^{\text{load}}(t, x, y) = S \exp(-x'^2/L^2)H(t)$, where the primed coordinates and the line load are inclined at an angle $\phi = \pi/4$ with respect to the unprimed coordinates and the unperturbed motion.

Fig. 4.13 shows the slip velocity on the interface as a function of load amplitude. As expected, the interface behavior changes from the linearized response to a frictionless response as the amplitude grows.

4.8 Discussion

We have shown that steady state sliding between two identical elastic halfspaces is stable with respect to slip perturbations at any orientation with respect to the original sliding. The basic effect of friction is to introduce a preferred direction of slip along which the energy driving the steady state motion is precisely balanced by the energy dissipated during slip. Transverse motions encounter an effectively viscous frictional resistance that increases with transverse slip velocity, leading to additional dissipation of energy from the system. Friction influences wave propagation by coupling the antiplane and inplane wave systems. The source-free response is characterized by the existence of damped interface waves, whose phase velocity depends on both the steady state conditions and the direction of propa-

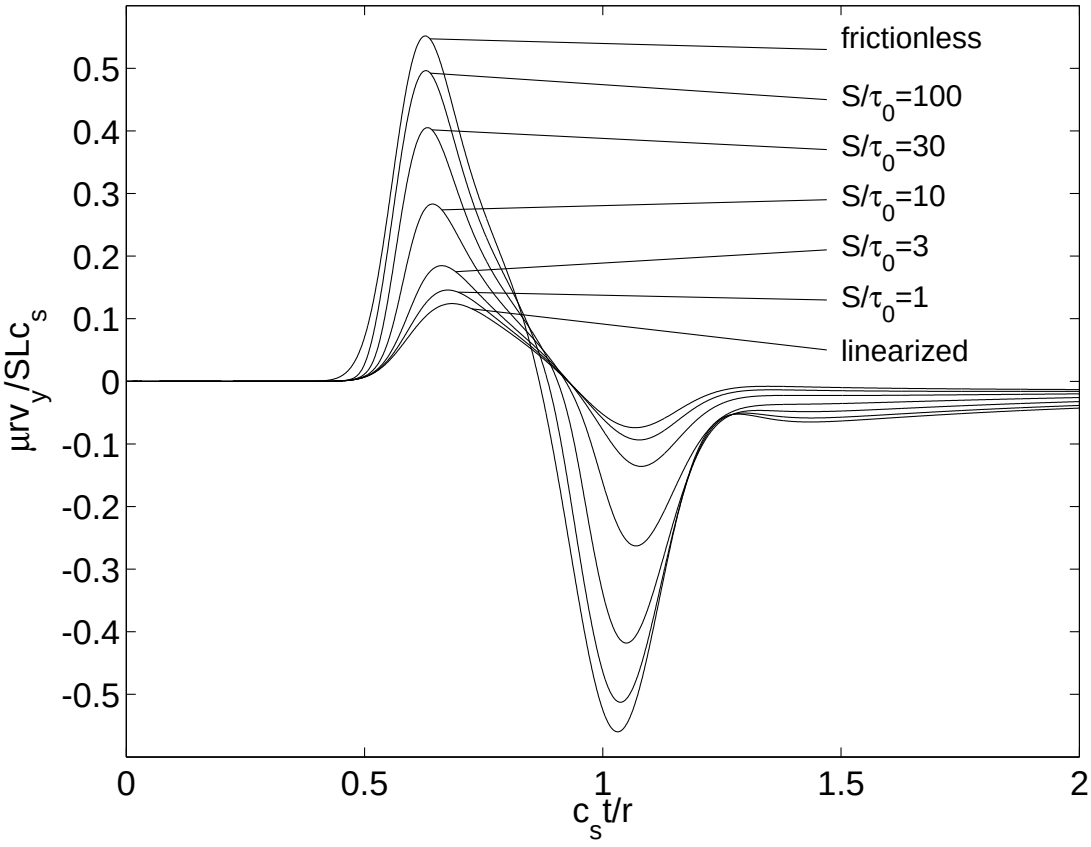

Figure 4.13: Comparison of the interfacial velocity history $\mu v_y/Sc_s$ for a 2D gaussian load with step-function time dependence for various load strengths S at $x'/L = 4$ with the nonlinear boundary condition (4.3.1). The load is inclined at the angle $\phi = \pi/4$ with respect to the direction of original sliding. The initial conditions are such that $\eta = 3$. As the load strength is increased, the interface behavior changes from the linearized response to a frictionless response.

gation with respect to the initial sliding direction. We find that for higher levels of friction, corresponding to $\eta > 1$, a third root of the dispersion relation comes into existence and is related to whether or not the instantaneous response of the system to transverse slip is a decrease or increase in transverse traction. This is a standing wave mode with a rapid decay rate; consequently, it has little signature in the long-time response of the system.

We also solved the transient problem corresponding to the application of point and line tractions on the interface, showing that the response consists of P and S waves, interface waves, and head waves. The solutions provide insight into the speed at which shearing forces are transmitted across the interface to drive decohesion or failure of as yet locked areas. For cracks with a stress drop that is small compared to the absolute value of stress, the transmission of these forces is best understood not by decomposing the response into inplane and antiplane components, but instead by considering the directionally dependent phase velocity of the interface waves in the large η limit. An example of these waves appears in the form of slip pulses emitted from the failure of localized asperity contacts when the surrounding interface is frictionally sliding, as may occur during dynamic fracture (Dunham et al., 2003).

Direct application of the linearized results is limited to small perturbations occurring within an area of nearly constant slip velocity, and to motions preced-

ing the arrival of waves diffracted off of the crack edge. For large perturbations, the linearized analysis breaks down. In the nonlinear regime, the interface becomes isotropically dissipative, yielding a response similar to that of a frictionless interface, except that the waves are damped.

This study raises the question of whether or not the viscous damping that characterizes the 3D response is sufficient to stabilize sliding along a bimaterial interface, at least within some range of parameter space. This will require a study of the appropriate dispersion relation.

Chapter 5

Steady State Ruptures

This Chapter, essentially in this form except for minor changes, appeared in:

Dunham, E. M., and R. J. Archuleta (2005), Near-source ground motion from steady state dynamic rupture pulses, *Geophys. Res. Lett.*, 32, L03302, doi: 10.1029/2004GL021793.

5.1 Abstract

Ground motion from two-dimensional steady state dynamic ruptures is examined for both subshear and supershear rupture velocities. Synthetic seismograms demonstrate that coherent high-frequency information about the source process rapidly attenuates with distance from the fault for subshear ruptures. Such records provide almost no resolution of the spatial extent of the stress breakdown zone. At supershear speeds, S waves radiate away from the fault, preserving the full source spectrum and carrying an exact history of the slip velocity on both the fault-parallel and fault-normal components of motion, whose amplitudes are given by a function of rupture speed that vanishes at $\sqrt{2}$ times the S-wave speed. The energy liberated from the strain field by the passage of a supershear rupture is partitioned into fracture energy dissipated within the fault zone and far-field S-wave radiation. The partition depends on both the rupture velocity and the size

of the breakdown zone.

5.2 Introduction

Evidence for ruptures exceeding the S-wave speed continues to mount, most recently in the 2002 M_w 7.9 Denali Fault earthquake (Ellsworth et al., 2004; Dunham and Archuleta, 2004). The ground motion recorded 3 km from the fault at Pump Station 10 exhibited a set of pulses unlike any previously recorded. In light of this record and to further explain features appearing in the model of this event by Dunham and Archuleta (2004), we turn our attention to the near-source ground motion of dynamic ruptures. In particular, we discuss how the resolution of dynamic rupture parameters from near-source records depends on rupture speed.

As a starting model, we investigate two-dimensional (2D) rupture pulses of finite length L, propagating at some steady state velocity V in the positive x direction along the fault plane $y = 0$. We shall refer to the x and y directions as fault parallel (FP) and fault normal (FN). The material on either side of the fault is identical, isotropic, and linear elastic, with shear modulus μ and P- and S-wave speeds c_p and c_s. The steady state assumption implies that we are modeling only the coherent portion of the fields due to a smooth rupture process, and not the incoherent high-frequency radiation that results from breaking through small-scale

heterogeneities.

We specify the shear traction $\tau(x)$ within the slip zone (unlike kinematic models, which would specify slip). Following Broberg (1978, 1989), expressions for the velocity and stress fields, both on and off of the fault, are written in terms of a single integral expression of $\tau(x)$ over the slip zone, weighted by a singular kernel. The expressions are derived in appendix B. Rice et al. (2005) has recently evaluated the integral in closed form for the specific case of subshear ruptures in which the shear traction decreases linearly with distance behind the rupture front. In order to accommodate any general $\tau(x)$ and to extend the model to supershear speeds, we numerically evaluate this integral at each observation point, requiring quadrature routines specifically designed to handle integrable and Cauchy-type singularities in the integrand (Piessens et al., 1983).

The elastic fields may be separated into dilatational and shear parts, each governed by the wave equation with the appropriate wave speed. Under steady state conditions, the governing equations become two-dimensional in $x - Vt$ and y. A general field f at speed V may be written as

$$f(t, x, y) = f^p(x - Vt, y) + f^s(x - Vt, y), \tag{5.2.1}$$

where f^p and f^s result from a displacement field $\mathbf{u} = \mathbf{u}^p + \mathbf{u}^s$ satisfying $\nabla \times \mathbf{u}^p = 0$ and $\nabla \cdot \mathbf{u}^s = 0$. Using Fourier analysis, we write

$$f^j(x - Vt, y) = \int_{-\infty}^{\infty} \hat{f}^j(k_x) e^{ik_x(x-Vt)} e^{-k_x \alpha_j y} dk_x, \tag{5.2.2}$$

where $\alpha_j = \sqrt{1 - V^2/c_j^2}$ and $j = p$ or s. This decomposes the response into plane waves $e^{i(k_x x + k_y y - \omega t)}$, subject to the dispersion relation $\omega = c_j \sqrt{k_x^2 + k_y^2}$, and to the condition that the FP phase velocity equals the steady state velocity: $\omega/k_x = V$. For $V < c_s$, both the P and S waves are inhomogeneous. Their amplitude decays exponentially with distance as the observation point moves away from the fault, with the decay length set by the FP wave number k_x and the velocity-dependent factor α_j. When $c_s < V < c_p$, α_s becomes imaginary, and the S waves radiate away from the fault; i.e.,

$$f^s(x - Vt, y) = \int_{-\infty}^{\infty} \hat{f}^s(k_x) e^{ik_x(x+\beta_s y - Vt)} dk_x, \tag{5.2.3}$$

where $\beta_s = \sqrt{V^2/c_s^2 - 1}$. The shear field on the fault is transported without attenuation to observation points off of the fault, enabling a precise determination of the source properties from near-source records of supershear ruptures.

5.3 Subshear Ruptures

Let us begin with subshear ruptures. We take $t = 0$ such that $x - Vt \to x$ and place the origin of our coordinate system at the leading edge of the slip zone. We

use the linear distance-weakening model of Palmer and Rice (1973) in which

$$\tau(x) = \begin{cases} \tau_p + (\tau_p - \tau_r)x/R, & -R < x < 0 \\ \tau_r, & -L < x < -R. \end{cases} \tag{5.3.1}$$

Fig. 5.1 shows the velocity field and synthetic seismograms. The motion is predominantly in the FN direction, and the synthetics are virtually identical to those from steady state kinematic models (e.g., (Luco and Anderson, 1983)). As expected on the basis of the Fourier decomposition, increasing the distance between the observer and the fault filters the high frequency components of the wavefield excited by the source process (e.g., (Aki and Richards, 2002), p.524). We can estimate the minimum resolvable wavelength for the shear component of the fields $\lambda^s_{\min}$ at some distance y away from the fault in the following manner: Information at a particular frequency becomes irresolvable when its amplitude drops to some fraction, say 5%, of its amplitude on the fault, leading to the condition $e^{-2\pi\alpha_s y/\lambda^s_{\min}} \sim 0.05$. For $V \sim 0.85c_s$, $\lambda^s_{\min} \sim y$. An even stricter restriction exists for the dilatational fields. This echoes a similar conclusion by Guatteri and Spudich (2000), and demonstrates the fundamental difficulty inversions face when using records from subshear ruptures, even without finite bandwidth limitations. On the other hand, our analysis supports the use of kinematic modeling for sub-Rayleigh ruptures, and emphasizes that the parameterization of the slip velocity

function will have little effect on the ground motion, so long as the final slip and rise time are preserved.

5.4 Supershear Ruptures

The ground motion from supershear ruptures is shown in Fig. 5.2. Planar wavefronts emanate from the leading and trailing edges of the slip zone. Preceding the arrival of the Mach front is the dilatational field, characterized by a circular pattern of rotation around the slip zone. Unless the observer is on the fault, this results in predominantly FP motion, particularly as $V \to c_p$. In this limit, the P waves become homogeneous and propagate at grazing incidence to the fault with a purely FP particle motion.

The fields change character as V crosses $\sqrt{2}c_s$, the speed at which the S-wave radiation vanishes (Eshelby, 1949). This follows from the expression for the shear traction on the fault in terms of the displacement fields:

$$\sigma_{xy} = \mu \left(\partial u_x / \partial y + \partial u_y / \partial x \right), \tag{5.4.1}$$

or in the plane wave basis:

$$\sigma_{xy} = \mu \left(i k_y u_x + i k_x u_y \right). \tag{5.4.2}$$

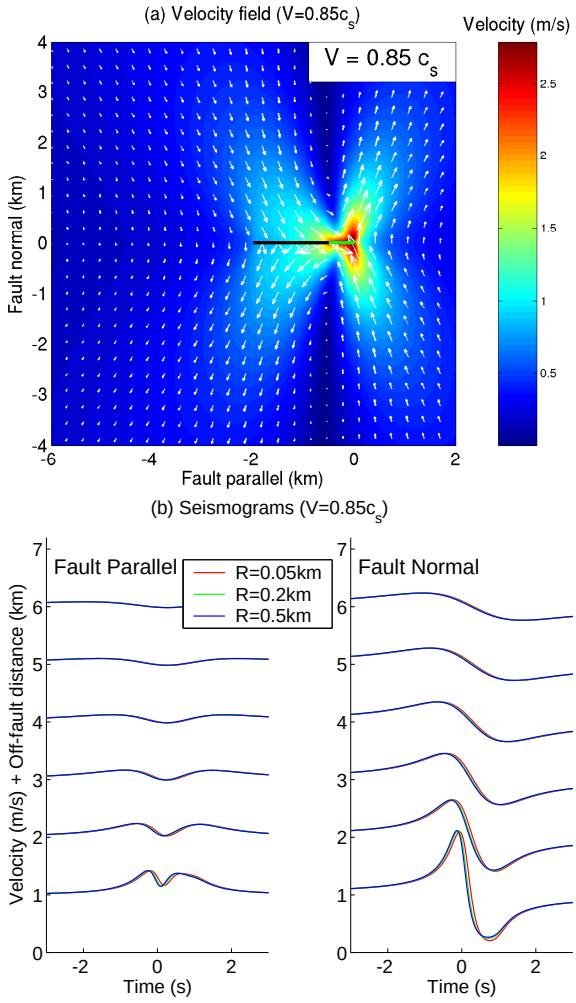

Figure 5.1: Velocity field (a) and synthetic seismograms (b) for a subshear rupture ($V = 0.85c_s$). In (a) the heavy black line denotes the slip zone and the heavy green line the breakdown zone. We take $\tau_p - \tau_r = 20$MPa, $\mu = 30$GPa, $L = 2$km, $c_p = 6$km/s, $c_p = \sqrt{3}c_s$, and $R = 0.5$km. In (b) synthetic seismograms are computed for several values of R as labeled, holding the final slip fixed by varying $\tau_p - \tau_r$. For $R = 0.5$, 0.2, and 0.05km, the equivalent slip-weakening distances (i.e., the slip at $x = -R$) are $D_c = 0.744$, 0.465, and 0.231m, the strength drops are $\tau_p - \tau_r = 20.0$, 30.0, and 58.71MPa, and the fracture energies are $G = 6.66$, 6.23, and 6.03MJ/m^2. Beyond several km from the fault, the records from all cases are indistinguishable.

Choosing a particular V sets both the relative amplitudes of k_x and k_y and the ratio between u_x and u_y since it determines the propagation angle of the radiating wave with respect to the fault. At $V = \sqrt{2}c_s$, a precise balance occurs ($k_x = k_y$ and $u_x = -u_y$), implying that such a wave exerts no shear force on the interface. Conversely, a change in shear traction on the fault (as we model the source process) does not excite S waves. As V crosses $\sqrt{2}c_s$, the relative sign of stress and displacement reverses, resulting in a reversal of the S-wave particle motion.

The ground motion from supershear ruptures contains a wealth of information. The shear field carries an exact history of the slip velocity that appears in both the FP and FN velocity components, as well as in all of the stress components. The velocity fields carried by the S waves are given by

$$v_x^s(x + \beta_s|y|) = \frac{\mathrm{sgn}(y)}{2}\frac{\beta_s^2 - 1}{\beta_s^2 + 1}\Delta v(x + \beta_s|y|) \tag{5.4.3}$$

and

$$v_y(x + \beta_s|y|) = -\frac{1}{2\beta_s}\frac{\beta_s^2 - 1}{\beta_s^2 + 1}\Delta v(x + \beta_s|y|), \tag{5.4.4}$$

where $\Delta v(x)$ is the slip velocity on the fault. The record from even a single station determines both V (from the FP to FN ratio) and Δv.

The direct transport of the slip velocity function off of the fault results in

large amplitudes of both velocity and acceleration, particularly if $R/L \ll 1$, as laboratory measurements seem to indicate. As discussed in the previous Section, R cannot be reliably estimated from current (sub-Rayleigh) ground motion records. Consequently, the use of large values of R to resolve the breakdown process in numerical models will result in an underprediction of the peak ground velocity and acceleration when the rupture process is supershear.

5.5 Energy Balance

The energy balance for dynamic ruptures changes considerably at supershear speeds. For subshear speeds, steady state pulses excite only inhomogeneous waves that do not radiate into the far field. Consequently, all of the strain energy liberated by allowing slip to temporarily relax the stress field dissipates within the fault zone as fracture energy (Rice et al., 2005). At supershear speeds, the S waves radiate and the flux of energy carried by these waves must be taken into account. The proper balance of energy (per unit area advance of the rupture) is $(\tau_0 - \tau_r)\delta = G + G_s$, where τ_0 is the initial (and final) shear traction far in front of (and behind) the slip zone, δ is the final slip, G is the fracture energy, and G_s is the radiated S-wave energy (absent for $V < c_s$). The left member of this equation is the work done by the remote stress field in excess of the residual stress, which

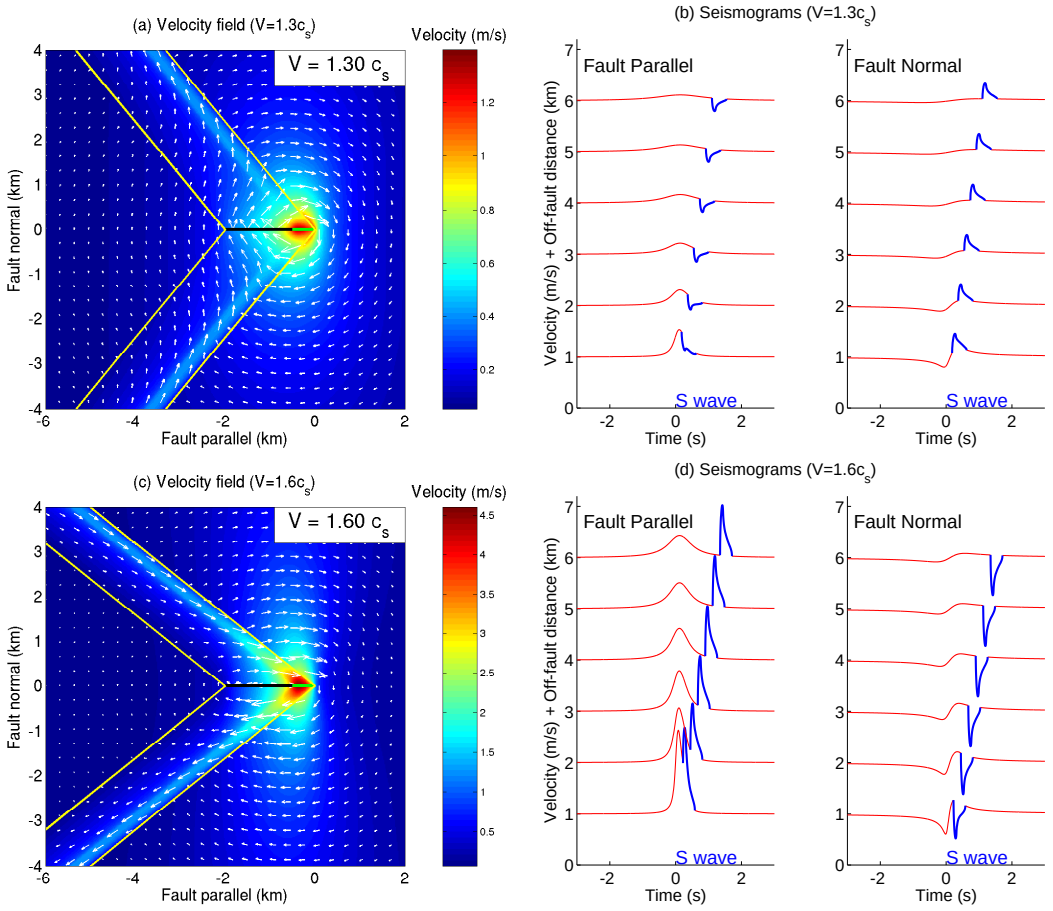

Figure 5.2: Velocity field (a and c) and synthetic seismograms (b and d) for supershear ruptures having speeds $V = 1.3c_s$ and $1.6c_s$. In (a) and (c) the heavy black line denotes the slip zone and the heavy green line the breakdown zone. The heavy blue lines in the seismograms mark the portions of the records during the passage of the radiated S waves. Parameters are given in the caption of Fig. 5.1.

is the energy available for rupture from the elastic medium. The radiated S-wave energy can be calculated by integrating the FN flux of energy over the slip zone:

$$G_s = 2g_s(V/c_s)\rho \int_{-L}^{0} v_x^2(x, y = 0)dx, \tag{5.5.1}$$

where

$$g_s(V/c_s) = [(\beta_s^2 - 1)/(\beta_s^2 + 1)]^2/\beta_s. \tag{5.5.2}$$

Dimensional arguments require G (and G_s) to take the form $h(V/c_s, R/L)(\tau_p - \tau_r)^2 R/\mu$. For subshear ruptures h factors into two terms, the first dependent on V/c_s and the second on R/L. This factorization does not carry over to supershear ruptures (Broberg, 1989). Fig. 5.3 shows the partition of energy as a function of R/L and V/c_s. As R/L decreases, most of the energy is radiated, with the exception of a small range of velocities surrounding $\sqrt{2}c_s$, since no S waves are excited at this speed.

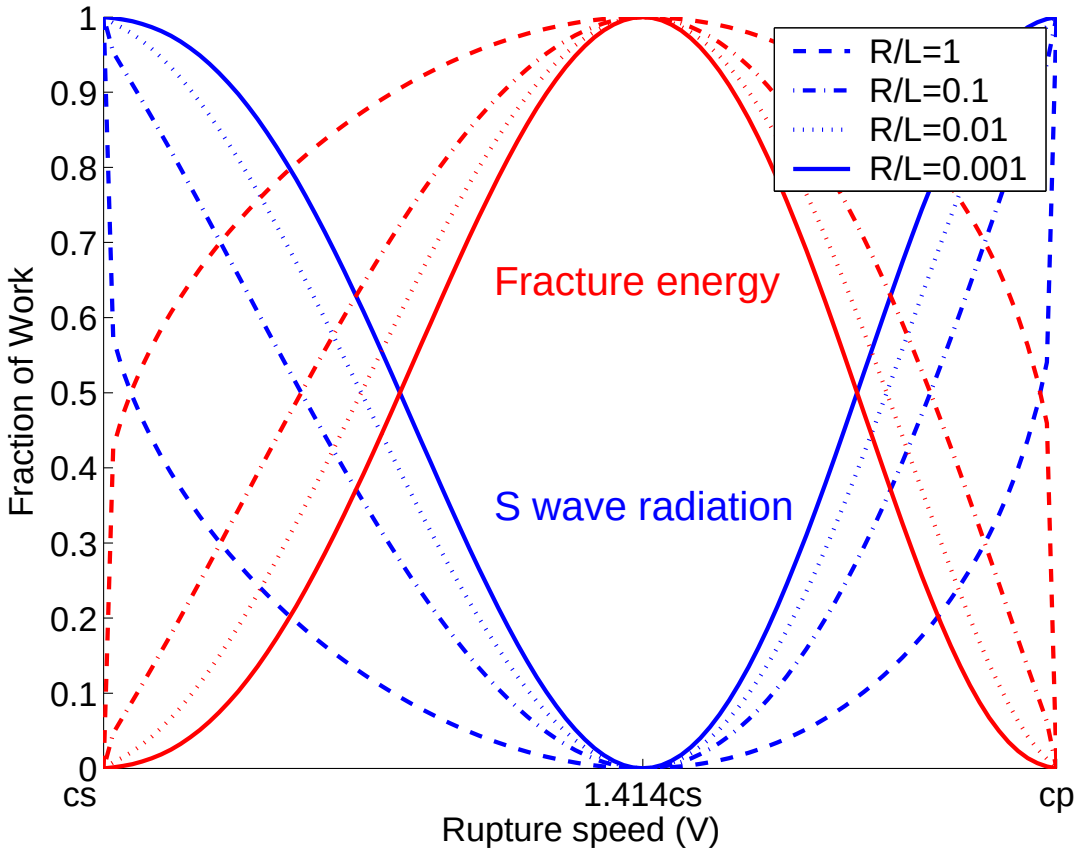

Figure 5.3: Energy partition between fracture energy and far-field S-wave radiation for supershear ruptures as a function of V and R/L for Poisson's ratio $\nu = 1/4$.

Chapter 6

The Supershear Transition

This Chapter, essentially in this form except for minor changes, appeared in:

Dunham, E. M., and R. J. Archuleta (2004), Evidence for a supershear transient during the 2002 Denali Fault earthquake, *Bull. Seismol. Soc. Am.*, 94, S256-S268.

and

Dunham, E. M., P. Favreau, and J. M. Carlson (2003), A supershear transition mechanism for cracks, *Science*, 299, 1557-1559.

6.1 Diffraction Effects

The allowed velocity regimes and supershear transition mechanism follow from a study of the waves that transmit shearing forces from within the breakdown zone to the unbroken material ahead of the rupture front. To illustrate this, we consider a semi-infinite mode II crack constrained to the plane $y = 0$ in a homogeneous elastic medium, with fields depending on x and y only. The medium is characterized by a shear modulus μ and P- and S-wave speeds c_p and c_s. At time $t = 0$, the crack tip, which is moving along the positive x-axis at velocity V, passes the origin.

To solve for the fields within the medium, we must specify boundary conditions on the material directly on either side of the fault. In order that the fault does

not open, we require continuity of normal displacement. Continuity of shear and normal tractions across the interface follows from momentum conservation. Furthermore, at each point on the fault, we must specify either slip or shear traction. In contrast to a kinematic source representation, in which the slip field is specified at every point on the fault, we follow the usual dynamic representation by specifying shear traction behind the moving crack tip and slip (identically zero) ahead. We require the stress field to be nonsingular at the tip, which is accomplished by introducing a finite length or time scale over which the breakdown in stress occurs, as in the cohesive zone models of Ida (1972); Palmer and Rice (1973); Andrews (1976).

We then consider an advance of the crack tip over an infinitesimal time interval $\mathrm{d}t$. As the crack extends, the shear traction relaxes behind the crack tip. The exact process by which this occurs depends on the specific friction law or fracture criterion. The linearity of the governing equations allows us to construct the breakdown in stress as a superposition of line tractions (extending infinitely in the z-direction), each applied at some distance $x = -L$ behind the crack tip with amplitude F (force/length) and having step-function time dependence. Since the shear traction at time $t = \mathrm{d}t$ is specified, then $F(x) = [\sigma_{xy}(t = 0, x) - \sigma_{xy}(t = \mathrm{d}t, x)]\,\mathrm{d}x$, where $\mathrm{d}x = V\mathrm{d}t$ and σ_{ij} are the components of the stress field created by slip. This is illustrated in Fig. 6.1. The region of nonzero stress drop, in contrast to

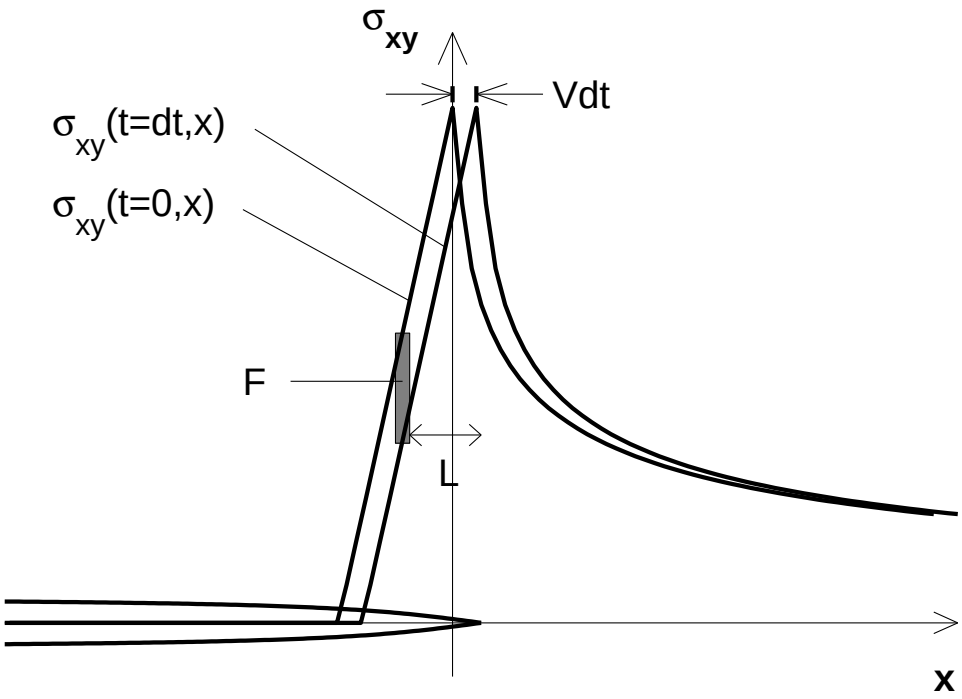

Figure 6.1: Schematic diagram illustrating the superposition of line tractions (stress drops) for $x < 0$. The fault is locked for $x > 0$ and the crack advances at velocity V over an infinitesimal time interval dt.

the actively slipping area in the kinematic representation, is the only source of elastic waves in the dynamic representation.

Letting u_i be the components of the displacement field created by slip, we formally define this mixed boundary value problem as

$$\begin{aligned} u_x(t, x, y = 0) &= 0 \text{ for } Vt < x < \infty \\ \sigma_{xy}(t, x, y = 0) &= -FH(t)\delta(x + L) \text{ for } -\infty < x < Vt \\ \sigma_{yy}(t, x, y = 0) &= 0 \text{ for } -\infty < x < \infty, \end{aligned} \tag{6.1.1}$$

where $H(t)$ is the step function and $\delta(x)$ is the delta function. The last equation, which states that the normal stress is unchanged by slip, follows from symmetry conditions that arise when requiring the continuity of both normal stress and normal displacement.

Our approach to understanding dynamic crack growth is similar to that taken by Freund (1972a,b), and our problem is related to his so-called fundamental solution in the limit that $L \to 0$. The advantage to keeping L finite is conceptual, affording us an insight into the elastodynamic processes occurring within the breakdown zone.

We could further generalize this model by placing the stress drop some distance off of the fault within a damage zone. In this case the superposition would be over the volume containing the off-fault damage, rather than localized to the area of the fault within the cohesive zone. Considering the problem from this perspective, the transmission of forces to the unbroken area ahead of the crack tip occurs with the broken fault behind the crack tip playing the role of an interfacial waveguide for

the elastic waves emitted from within the damage zone. Since we have posed the problem within the framework of a mixed boundary value problem, the transition between the regions in which we specify shear traction and those in which we specify that slip vanishes (i.e., the crack edge) acts as a diffracting boundary. The waves released by the stress drop overtake the crack tip and diffract off of it (see Fig. 6.2).

The solution to our problem defines the Green function for some distribution of shear tractions applied on the sliding surface of a moving crack. Known as a transient weight function, it has a known analytical solution in the Fourier-Laplace domain (Freund, 1974; Brock, 1982; Kuo and Chen, 1992; Freund, 1989; Broberg, 1999a). However, since the problem possesses a characteristic length, the solution is not self-similar and requires multiple integrations to invert the transforms and extract the space-time history of the velocity and stress fields. Inversion of these transforms is, to the best of our knowledge, absent from the literature except for the use of asymptotic theorems to study the evolution of the stress intensity factor. Consequently, we present instead a numerical solution using the boundary integral methodology proposed by Geubelle and Rice (1995). The slip velocity and shear traction on the interface are shown as a function of position and time in Fig. 6.3 for a stationary crack tip. A similar solution is obtained for sub-Rayleigh crack speeds; only when the crack velocity exceeds some wave speed does the wavefront

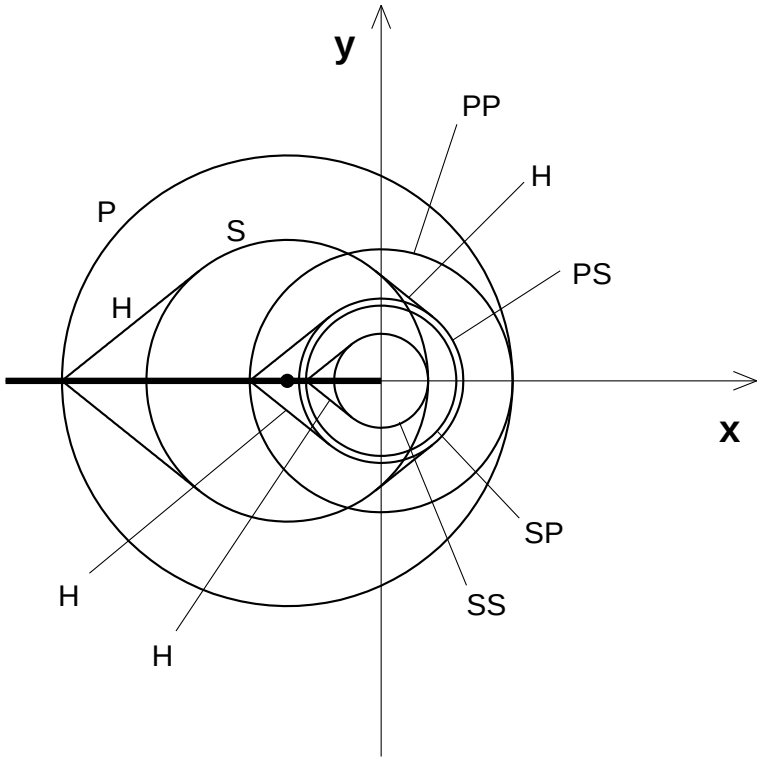

Figure 6.2: Wavefronts generated by a stress drop (marked by the circle) located some distance behind a stationary crack tip, after both P and S waves overtake the crack tip. Rayleigh waves and body waves generated by Rayleigh waves diffracting off of the crack tip are not shown to avoid excessive complication. The crack, denoted by the heavy line, lies in the half-plane $y = 0$, $x < 0$. Direct and diffracted waves are labelled, and H denotes a head wave resulting from P to S conversion on the crack face.

pattern change since these waves will no longer overtake the crack tip.

Up until the arrival of the P wave at the crack tip, the solution is self-similar and identical to that of Lamb's problem (a shear line force applied on the surface of a traction-free half-space), which is used to validate the numerical method (see the inset in Fig. 6.3). As such, the main features are well known. The line force emits P and S waves with cylindrical wavefronts, as well as planar head waves and an interfacial Rayleigh wave. A point on the fault begins to slip in the direction of the applied traction at the simultaneous arrival of the P wave and a head wave traveling along the interface at the P wave speed. This head wave is a radiating S wave excited by evanescent P waves trapped on the fault surface. Forward sliding continues until the arrival of the S wave, at which point slip reverses, with the interface sliding in the direction opposite the applied traction. Reverse sliding ceases when the Rayleigh wave arrives; positive slip velocity peaks at and decays after its arrival, with slip reaching the steady-state value only asymptotically as is characteristic in two dimensions.

There is a direct correlation between the allowed propagation velocity regimes and the direction of slip relative to the applied traction, as pointed out by Das (2003). For a given distribution in time and space of shear tractions (i.e., a prescribed rupture history), we could calculate the slip velocity history, which would be equivalent to that generated in Lamb's problem plus a correction to

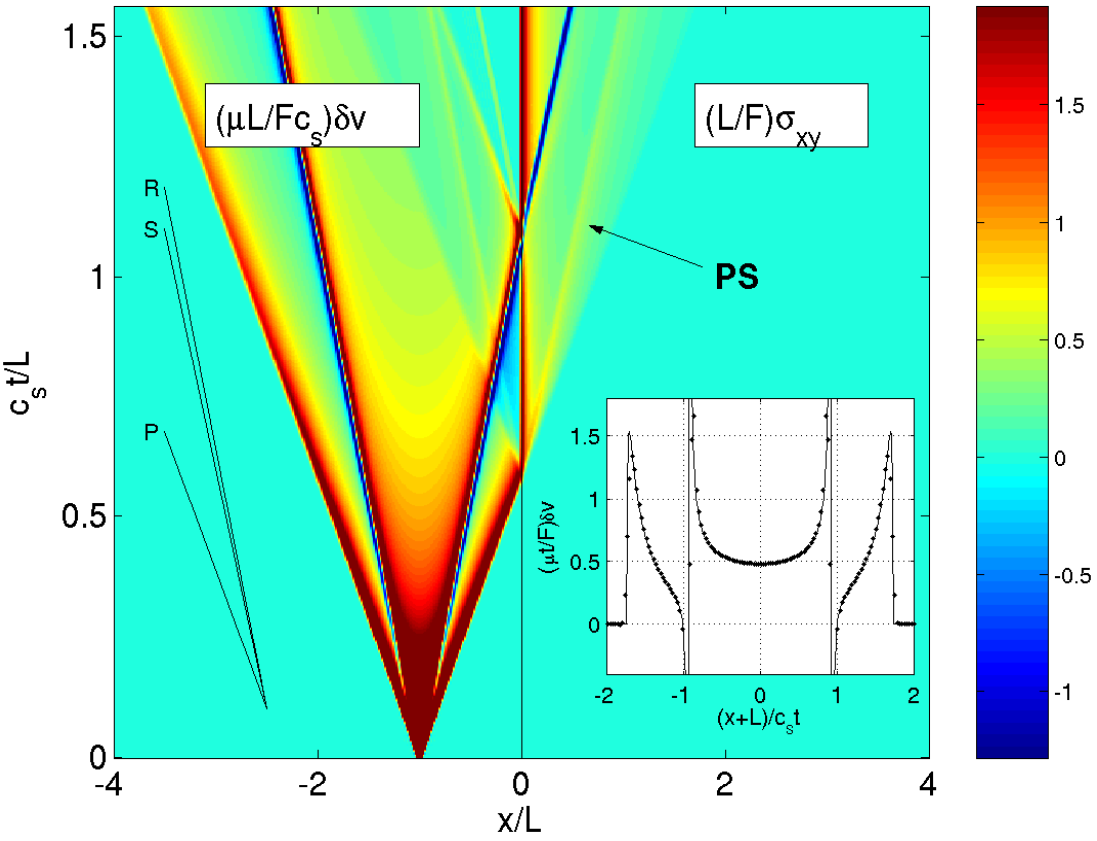

Figure 6.3: Evolution of slip velocity ($x < 0$) and shear traction ($x > 0$) after the step-function application of a line stress drop of magnitude F at $x = -L$ behind a stationary crack tip. The color scale measures the non-dimensionalized slip velocity and shear traction labeled at the top. The inset compares the numerical slip velocity (points) just prior to wave arrivals at the crack tip to the analytical solution for Lamb's problem (solid line). The peak in shear traction associated with the P to S wave conversion is labeled PS.

account for diffractions off of the crack tip, which are further discussed below. The rate of energy dissipation at each point on the fault is the product of the shear traction and slip velocity, from which we see that only when the fault slips in the direction of the applied traction is energy dissipated. Reverse motions, which we have allowed in our problem to render it linear, are typically prevented by friction; otherwise, this process would unphysically create energy.

Let us now take the steady-state limit of our problem. In this case, it is more appropriate to consider fixing the distance L in a frame that moves with the crack tip; such an analysis was conducted by Burridge et al. (1979) in their study of the stability of supershear propagation velocities. In the steady-state limit, only motions for which the apparent velocity along the fault matches that of the crack tip remain (i.e., those having a ray parameter of V^{-1}). For sub-shear propagation velocities, this implies that the driving force is carried only by evanescent P and S waves on the fault surface. A reversal in the direction of the shearing force carried by these waves occurs at the Rayleigh speed, resulting in the velocity range between the Rayleigh and S wave speeds becoming forbidden. In the supershear regime, the P wave remains evanescent but the S wave switches from evanescent to radiating. The angle that the S wavefront makes with the fault is the Mach angle $\arcsin(c_s/V)$. The associated shear fields retain a finite amplitude at infinity along the Mach cone. The only velocity at which the S

wave vanishes is the well known $\sqrt{2}$ times the S wave speed (Eshelby, 1949). The significance of this velocity appears clearly in the expression for the traction components on a flat surface due to incident plane waves (e.g., (Aki and Richards, 2002, p.132)). In our case, the situation is reversed, with traction changes on the surface exciting some superposition of plane waves. Our source is the application of a shear traction, with the normal traction remaining constant. It follows from the expressions in Aki and Richards (2002) that changes in shear traction moving at $V = \sqrt{2}c_s$ will not excite S waves.

We now return to the general transient problem and consider the diffraction pattern that emerges when steady-state conditions are not satisfied. This can occur when the crack tip accelerates between two steady-state regimes or when the magnitude of the stress drop is spatially heterogeneous. A simple illustration of this phenomenon is the growth of an initially steady-state crack into a region of increased stress drop (an asperity), as in the numerical study of Fukuyama and Olsen (2002). If we constrain the crack velocity to remain constant through this process, then the resulting fields can be constructed as a superposition of the fields carried by the original steady-state crack and the fields generated by the additional stress drop within the asperity applied some distance behind the moving crack tip, the remainder of the fault behind the tip being traction-free. This additional solution is exactly the transient diffraction problem we have solved. If we relax the

constant velocity condition and allow the crack to grow spontaneously according to some fracture criterion, then provided that the additional energy released within the asperity is sufficient, the diffracted P and S waves will initiate supershear growth. If this energy is sufficiently concentrated (by an abrupt large amplitude asperity), then the crack tip will be driven forward continuously by these diffracted waves to a supershear velocity. If the asperity amplitude is smaller, yet still large enough to provide sufficient energy to power the supershear rupture, then the diffracted S wave peak will build up gradually ahead of the crack tip and the supershear transition will be discontinuous.

Another source of these transient features is the presence of an additional diffracting boundary, such as the second crack tip (see, e.g., Fig. 1 of Eshelby (1969)) or the healing front in a rupture pulse model. The multiple diffractions between the two expanding crack tips generate the S wave stress peak that appears in analytical self-similar solutions for sub-Rayleigh cracks (Burridge, 1973; Broberg, 1994, 1995; Freund, 1989; Broberg, 1999a). The supershear transition appearing in the numerical experiments of Andrews (1976) on a bilaterally extending crack with homogeneous stress drop occurs by this mechanism. For an expanding crack, these diffractions have significant amplitude only during nucleation, where the characteristic length controlling the development of these features is the nucleation zone size, as found by Andrews (1976). In this case the S wave

peak builds up gradually, resulting in a discontinuous triggering of the supershear rupture some distance ahead of the original sub-Rayleigh rupture.

For supershear propagation velocities, the Rayleigh and S waves released within the breakdown zone will not overtake the crack tip. As self-similar analytical solutions in this velocity regime reveal (Burridge, 1973; Broberg, 1994, 1995), slip is not concentrated uniquely at the rupture front, as it is for sub-Rayleigh ruptures. A second peak in slip velocity travels at the Rayleigh speed. Similarly, spontaneously propagating cracks that accelerate from sub-Rayleigh to supershear velocities leave behind a secondary slip pulse at the Rayleigh speed. This feature emerges naturally from our representation of crack growth as Rayleigh waves generated within the breakdown zone that never reach the faster-moving crack tip. If the supershear transition is triggered by an asperity, then these Rayleigh waves derive their energy from the additional stress release within the asperity. As we later discuss, the signature of these Rayleigh waves in seismic radiation manifests almost entirely in ground motions perpendicular to the fault plane.

The effect of friction on the fault will be to disperse these Rayleigh waves. The dispersion relation for a linearized version of rate and state friction is given by Rice et al. (2001). Depending on frictional parameters and sliding conditions, larger wavelengths may unstably grow into the nonlinear regime until a stress drop

occurs. In this way, the Rayleigh wave could be viewed as a secondary rupture.

Extension of this analysis to three dimensional crack propagation is complicated. The representation of the breakdown zone consists of a superposition of point shear tractions applied some distance behind an arbitrarily shaped moving crack edge. Curvature of the crack edge focuses or defocuses the radiation released by the tractions (Achenbach and Harris, 1978). Such focusing alone can be sufficient to trigger localized supershear bursts (Dunham et al., 2003). Furthermore, the driving force provided by the stress drop becomes directionally dependent. Including friction and rotation of the slip vector introduces another nonlinearity into the problem. An exact solution for a point stress drop in three dimensions, neglecting any diffractions but including a linearized treatment of rake rotation under constant friction, is given by Dunham (2005).

6.2 Transient Supershear Bursts

Seismic data indicate fault ruptures follow complicated paths with variable velocity due to inhomogeneities in initial stress or fracture energy. We report a phenomenon unique to three dimensional cracks: locally stronger fault sections, rather than slowing ruptures, drive them forward at velocities exceeding the shear wave speed. This supershear mechanism differentiates barrier and asperity models

of fault heterogeneity, previously regarded as indistinguishable. High strength barriers concentrate energy, producing potentially destructive pulses of strong ground motion.

Earthquakes are modeled as shear cracks propagating along fault planes. Heterogeneous stress and strength distributions lead to complex rupture histories. Because elastic waves radiate from the concentrated region of maximum sliding velocity at the rupture front, perturbations to its motion, particularly those inducing propagation faster than the shear wave speed, are the source of high frequency ground motions (Madariaga, 1983). Material heterogeneity is characterized by regions of increased fracture energy, i.e., cohesive resistance to sliding, known as barriers (Das and Aki, 1977a). Alternatively, ruptures in the asperity model follow regions of high initial stress close to failure (Kanamori and Stewart, 1978). This prestress variability is set by the residual stress field remaining from past events combined with tectonic loading.

Spontaneous rupture occurs when the flux of kinetic and strain energy from the prestress field into the rupture front (i.e., the energy release rate) overcomes the local fracture energy. The trade-off between energy supplied from the prestress field and fracture energy results in an underdetermined problem, making it difficult to establish the source of fault heterogeneities (Guatteri and Spudich, 2000; Peyrat et al., 2001). In fact, radiation from dynamic two dimensional (2D) cracks is

identical for barrier and asperity models (Madariaga, 1983). Recent advances in parallel computing enable us to investigate complex three dimensional (3D) dynamic rupture propagation.

Large strike-slip earthquakes occur predominantly in mode II (slip parallel to the direction of rupture propagation), for which the limiting velocity is usually the Rayleigh surface wave speed, c_R. However, for a homogeneous medium with high prestress or low fracture energy, speeds between the shear wave speed, c_s, and longitudinal wave speed, c_p, are allowed (Burridge, 1973; Andrews, 1976; Broberg, 1994, 1995). Intersonic propagation, while theoretically predicted (Burridge, 1973), was only recently observed (Rosakis et al., 1999). Stable velocities are centered around $\sqrt{2}c_s$, a peculiar speed at which crack growth is similar to subsonic propagation (e.g., the Mach cones extending from the rupture front vanish) (Burridge et al., 1979; Freund, 1979; Broberg, 1994, 1995).

Seismic data indicate that most earthquakes occur slightly below c_R. With the advent of strong motion seismograph networks in the near-field, inversions and modeling of several major earthquakes suggest that supershear bursts occur on sections of the fault close to failure. These include the 1979 Imperial Valley (Archuleta, 1984), 1992 Landers (Olsen et al., 1997), and 1999 Izmit, Turkey (Bouchon et al., 2000, 2001) earthquakes.

We model bilaterally expanding ruptures (shear cracks) by solving the elasto-

dynamic wave equation in a 3D medium surrounding a rectangular planar fault. Slip, the relative shear displacement between the two sides of the fault, is constrained to be horizontal. We nucleate ruptures by initially overstressing a vertical section of the fault. We place periodic boundary conditions in the vertical direction to simulate an infinite width mode II crack, and absorbing boundary conditions on all other sides. Perturbations to the rupture front introduce a component of mode III failure (i.e., slip parallel to the rupture front).

A uniform compressive stress acts on the fault, which is governed by a fracture criterion relating shear traction to slip. In particular, we use a slip-weakening cohesive zone model that constrains material failure processes to the fault plane (Ida, 1972; Andrews, 1976). The fault starts at a prestress value, σ_0. Slip initiates when the shear stress reaches a critical static friction stress level, σ_s, normalized to unity. The stress then decreases linearly with increasing slip over a characteristic distance (i.e., the slip-weakening distance, d_c), after which the surfaces are left at a constant sliding friction value, σ_f, that we scale to zero. For unit area of new fracture, the work done against cohesion is the fracture energy, $G = \sigma_s d_c/2$.

The supershear transition for 2D mode II cracks on homogeneous faults occurs only if the prestress is sufficiently high. A stress peak traveling at c_s ahead of a sub-Rayleigh rupture exceeds the static stress, allowing the crack to jump to intersonic velocities (Burridge, 1973; Andrews, 1976). Cracks become supershear

after a distance (proportional to d_c) that diverges as the prestress approaches a numerically obtained critical value: $\sigma_0 = 0.38$ (Andrews, 1976). For lower prestress values, the crack's terminal velocity is c_R. This mechanism does not apply to 3D cracks. Instead, the dimensionless ratio κ of the energy release rate ($\sim \sigma_0^2 \lambda/\mu$, where μ is the shear modulus) to fracture energy controls the supershear transition (Madariaga and Olsen, 2000; Madariaga et al., 2000). The length scale λ determines stress concentration at the rupture front (i.e., the stress intensity factor) and is specific to the geometry of the problem (e.g., fault width for a rectangular planar fault).

We investigate cracks with prestress $0.3 \leq \sigma_0 \leq 0.4$, which remain sub-Rayleigh in the absence of any perturbations over the length of our fault. We introduce a circular obstacle to the fault, either a barrier, which requires more energy to break, or an anti-asperity: a region of lower prestress that decreases the energy release rate. Either obstacle locally reduces κ, suggesting that the energy balance would favor slower propagation or even arrest of the rupture. Model parameters, including obstacle size, are consistent with observations.

We measure distances in terms of the uniform grid spacing, and scale $\mu = 1$ and $c_s = 1$. We set the obstacle diameter to $D = 40$ and slip-weakening distance to $d_c = 10$. When rescaling to physically realistic values, note that displacement requires an additional factor of $(\sigma_s - \sigma_f)/\mu$. Thus, our barriers are

1.2km(μ/30GPa)(10MPa/($\sigma_s - \sigma_f$))(d_c/10cm) in diameter.

The anti-asperity model only slightly delays the rupture front, which moves to regain its unperturbed shape after breaking the obstacle (Fig. 1 and movie S1). The barrier model is much more complex (Fig. 1 and movie S2). The stress concentration at the rupture front is initially insufficient to break the barrier. The rupture temporarily halts as the stress grows to the higher static level inside. Meanwhile, the faster-moving rupture front outside of the barrier encircles it, breaking it from all sides. This is similar to the rupture of a single asperity of high prestress, initiated from a point on the edge of the asperity (Das and Kostrov, 1983). The rupture fronts within the barrier converge to nearly a point, resulting in a concentrated region of high slip velocity at the far side of the barrier. When the barrier breaks, it emits an elliptical slip velocity pulse moving at c_R in the direction parallel to slip and at c_s in the perpendicular direction, as well as a weaker pulse moving at c_p in the forward direction. Furthermore, the energy concentration induces the transition to a rupture velocity slightly less than $\sqrt{2}c_s$ (Fig. 2).

To explore this phenomenon, we varied both initial stress and barrier strength. We found that maximum slip velocities within the barrier scale linearly with static stress, rather than prestress as found in homogeneous models and assumed for all ground motion predictions (Brune, 1970; Aki and Richards, 2002). We refer to

this effect, resulting in slip velocities over an order of magnitude larger than at the unperturbed front, as barrier focusing.

Barriers slightly stronger than the surrounding fault ($1 < \sigma_s < 1.3$) only mildly perturb the rupture front, which returns toward the stable planar configuration at a sub-Rayleigh speed (Fig. 3). Above a critical strength ($\sigma_s^* \approx 1.3$), the restoring motion becomes supershear with a duration that, like the slip velocity, increases linearly with barrier strength until $\sigma_s \approx 3.5$.

At the opposite extreme with the strongest barriers ($\sigma_s \geq 7$), the rupture front splits as it breaks the material above and below the obstacle, coalescing on the far side into a region of high slip velocity. This is caused by rupture front focusing, in which two colliding fronts cause rapid stress drop (Fukuyama and Madariaga, 2000). This split-front focusing effect causes a burst of supershear propagation, with a duration independent of the barrier strength.

When the barrier breaks, it releases a slip velocity pulse travelling at c_p. If the rupture has not moved too far past the barrier, this pulse carries sufficient energy to enhance the duration of supershear propagation, already activated by split-front focusing. Precise timing, occuring for $3.5 < \sigma_s < 7$, results in a resonance during which the supershear front moves ahead of the unperturbed front.

Further numerical experiments showed that weak anti-asperities ($\sigma_0 \leq 0$) induce a supershear transition due to split-front focusing. Low prestress values are

necessary because the energy release rate into the rupture front is a non-local function of the prestress history (Freund, 1989). The size of the anti-asperity relative to the crack length precludes large variations of the energy release rate, making anti-asperities dynamically much less of an obstacle than barriers. An anti-asperity taking the same time to break as a barrier with $\sigma_s = 5$ has $\sigma_0 = -1.2$, and produces only 0.65 times the spatial duration of supershear propagation. Furthermore, formation of a high slip velocity region within the anti-asperity does not occur as it does within the barrier (for which maximum slip velocity scales with the barrier strength). The anti-asperity with $\sigma_0 = -1.2$ produces only 13% of the maximum slip velocity observed within the barrier. This limits the amplitude of seismic waves released from the anti-asperity, preventing the rupture front from overtaking its unperturbed position.

Our results show that existing parameters governing the supershear transition on a homogeneous fault cannot characterize the complex dynamics of heterogeneous faults. Despite such idealizations as a perfectly circular barrier with uniform properties, our simulations reveal unexpected phenomena that may be common at many scales. Because ground motion is proportional to slip velocity (Aki and Richards, 2002), barrier focusing releases intense seismic waves. Near-field seismograms from the 1984 Morgan Hill earthquake show, in addition to the usual phases from the hypocenter, a second large pulse in ground motion arriving about

8 s later, traced to a region 14 km along strike from the hypocenter (Hatzell and Heaton, 1986; Beroza and Spudich, 1988). Kinematic inversions suggest that the region failed after being encircled by the rupture front (Beroza and Spudich, 1988), making this a likely candidate for our mechanism. The extreme amplitudes of these pulses make them potentially destructive, suggesting that identifying currently unbroken barriers (from inversions of past events) must become a part of seismic hazard analysis.

On a much smaller scale, our results apply to dynamic shear fracture of brittle engineering materials. Laboratory experiments provide a convenient framework for analysis of our phenomena. Furthermore, barrier focusing, and the corresponding scaling of slip velocity with static stress rather than prestress, is unique to three dimensional cracks. This scaling, which implies a local independence from external loading, runs counter to fundamental fracture mechanics assumptions and likely extends to dynamic tensile failure of brittle materials common in engineering applications.

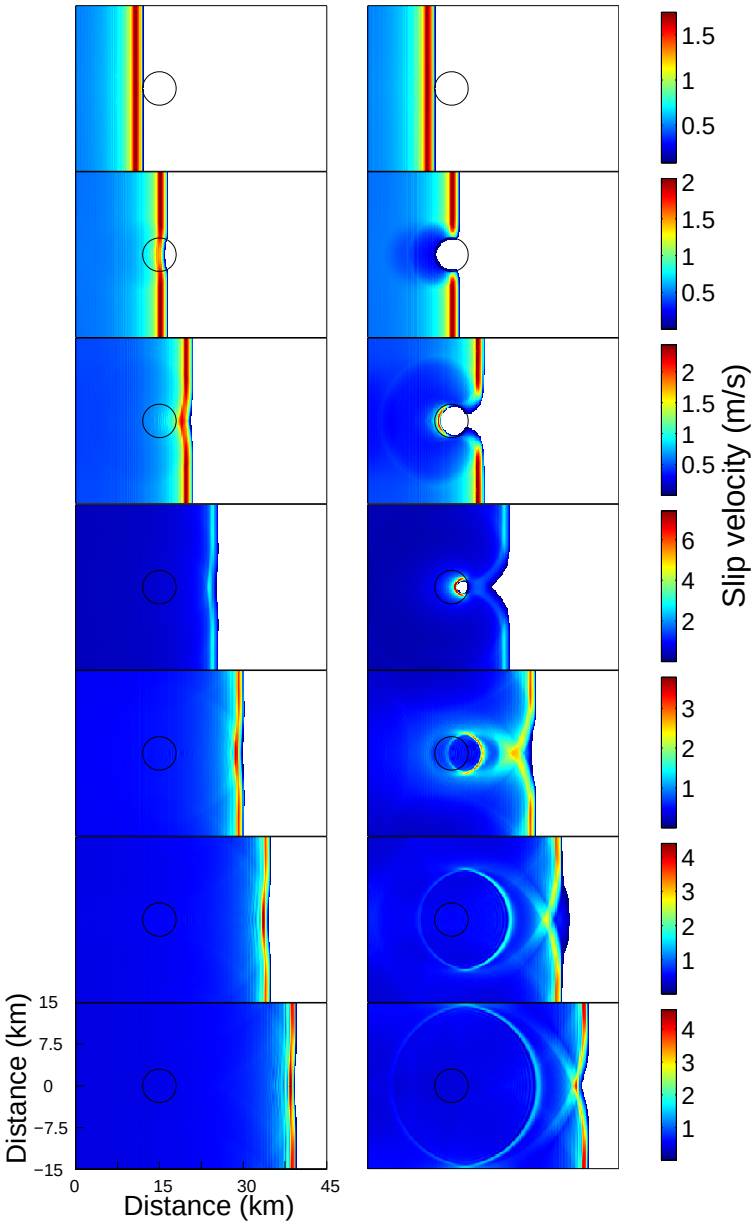

Figure 6.4: Consecutive snapshots showing slip velocity on the fault plane for the anti-asperity (**left**) and barrier (**right**) models, both having κ locally decreased by a factor of 5. Locked regions of the fault are uncolored, and the black circle marks the obstacle's perimeter. Note that the color scale changes at each time step.

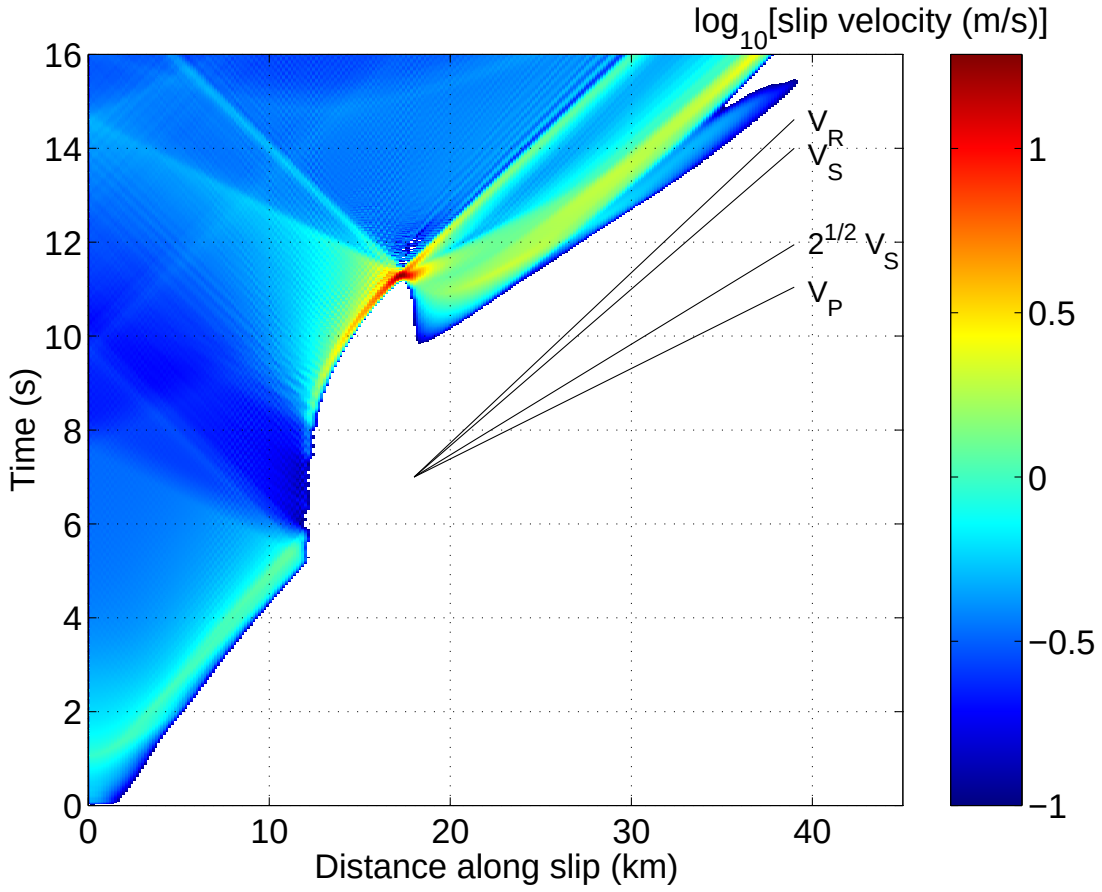

Figure 6.5: Space-time plot of slip velocity along the symmetry axis through the center of the barrier, which lies at $x = 15$km. The four black lines show wave speeds. Locked regions of the fault are uncolored.

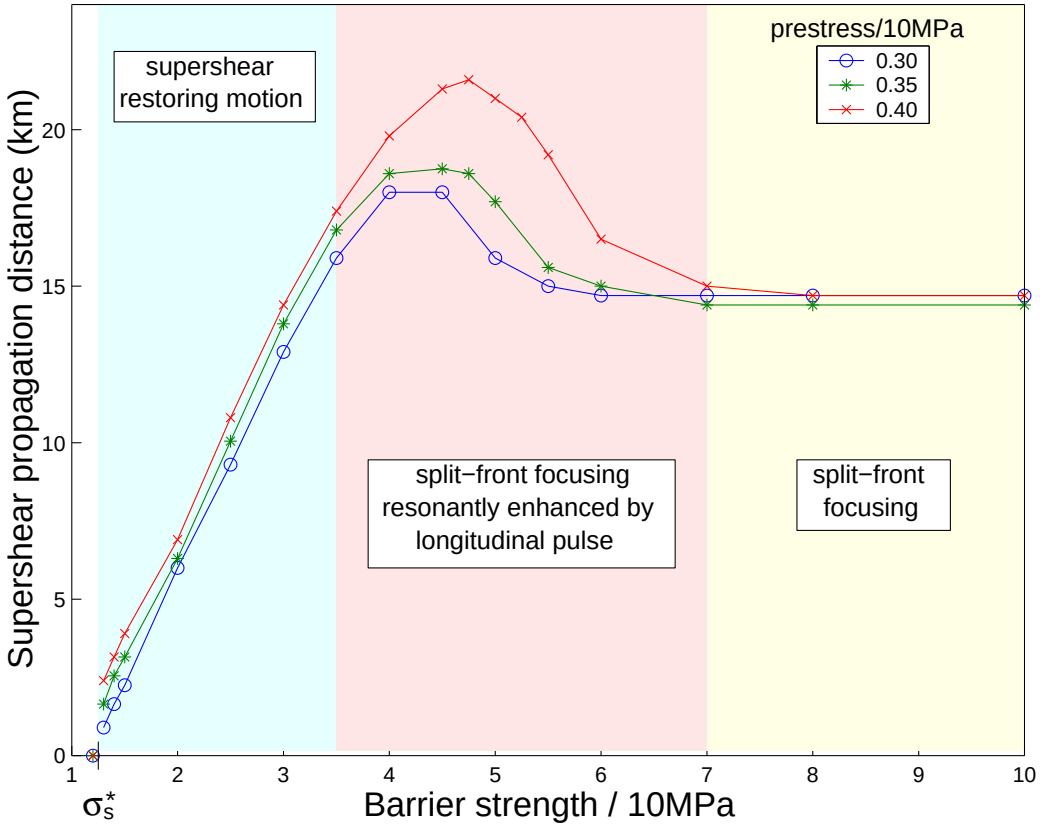

Figure 6.6: Dependence of supershear propagation on barrier strength and prestress. The background colors indicate the mechanism governing the supershear transition.

Chapter 7

Seismic Observations of Supershear Ruptures

This Chapter, essentially in this form except for minor changes, appeared in:

Dunham, E. M., and R. J. Archuleta (2004), Evidence for a supershear transient during the 2002 Denali Fault earthquake, *Bull. Seismol. Soc. Am.*, 94, S256-S268.

and

Dunham, E. M., and R. J. Archuleta (2005), Near-source ground motion from steady state dynamic rupture pulses, *Geophys. Res. Lett.*, 32, L03302, doi: 10.1029/2004GL021793.

7.1 Abstract

Elastodynamic considerations suggest that the acceleration of ruptures to supershear velocities is accompanied by the release of Rayleigh waves along the fault from the stress breakdown zone. These waves generate a secondary slip pulse trailing the rupture front, but manifest almost entirely in ground motion perpendicular to the fault in the near-source region. We construct a spontaneously propagating rupture model exhibiting these features, and use it to explain ground motions recorded during the 2002 Denali Fault earthquake at pump station 10, located

3 km from the fault. We show that the initial pulses on both the fault normal and fault parallel components are due to the supershear stress release on the fault while the later arriving fault normal pulses result from the trailing subshear slip pulse on the fault.

7.2 Introduction

On November 3, 2002, a M_{w} 7.9 earthquake shook central Alaska. Rupture initiated at 22:12:41.0 UTC on the Susitna Glacier thrust fault before subsequently transferring onto the Denali fault. After propagating 240 km east on this fault, the rupture branched onto the Totschunda fault. Only one instrument, pump station 10 (PS10), maintained by the Alyeska Pipeline Service Company, recorded near-source ground motions. PS10 is located approximately 70 km east of the epicenter along the Denali fault near the Trans Alaska Pipeline. Fig. 7.1 provides a schematic map of the fault geometry. Finite fault inversions and geological considerations support a right-lateral strike-slip mechanism on a nearly vertical fault near PS10 (Eberhart-Phillips et al., 2003). Situated only 3 km north of the fault, the station recorded a particularly interesting sequence of strong ground motion pulses as the rupture extended past it. Fig. 7.2 shows the instrument-corrected records, which have been rotated into fault normal (FN) and parallel

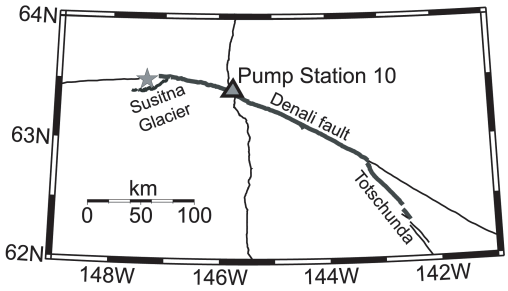

Figure 7.1: Fault geometry around PS10 (after Ellsworth et al. (2004)).

(FP) components (Ellsworth et al., 2004).

A single one-sided pulse (labeled A in Fig. 7.2) characterizes the FP component. The pulse is narrow (approximately 3 s rise time) and roughly symmetric. The FN component contains two similarly narrow pulses, the first (B) concurrent with A. The second (C) arrives 2.6 s later and is only slightly smaller in amplitude. Furthermore, about 6.5 s after the initial pulse, a broad motion (D) begins on the FN component, comprising of motion toward and then away from the fault.

We focus on several features. First, the FP amplitude is approximately 1.5 times larger than FN. This is not typical of large strike-slip earthquakes, as discussed by Archuleta and Hartzell (1981); Hall et al. (1995). As several authors have suggested (Ellsworth et al., 2004; Aagaard and Heaton, 2003) and we corroborate, this is accounted for by supershear rupture speeds. However, kinematic analyses which allow slip only once at the rupture front have failed to explain pulses C and D. We show that these pulses arise naturally in dynamic models

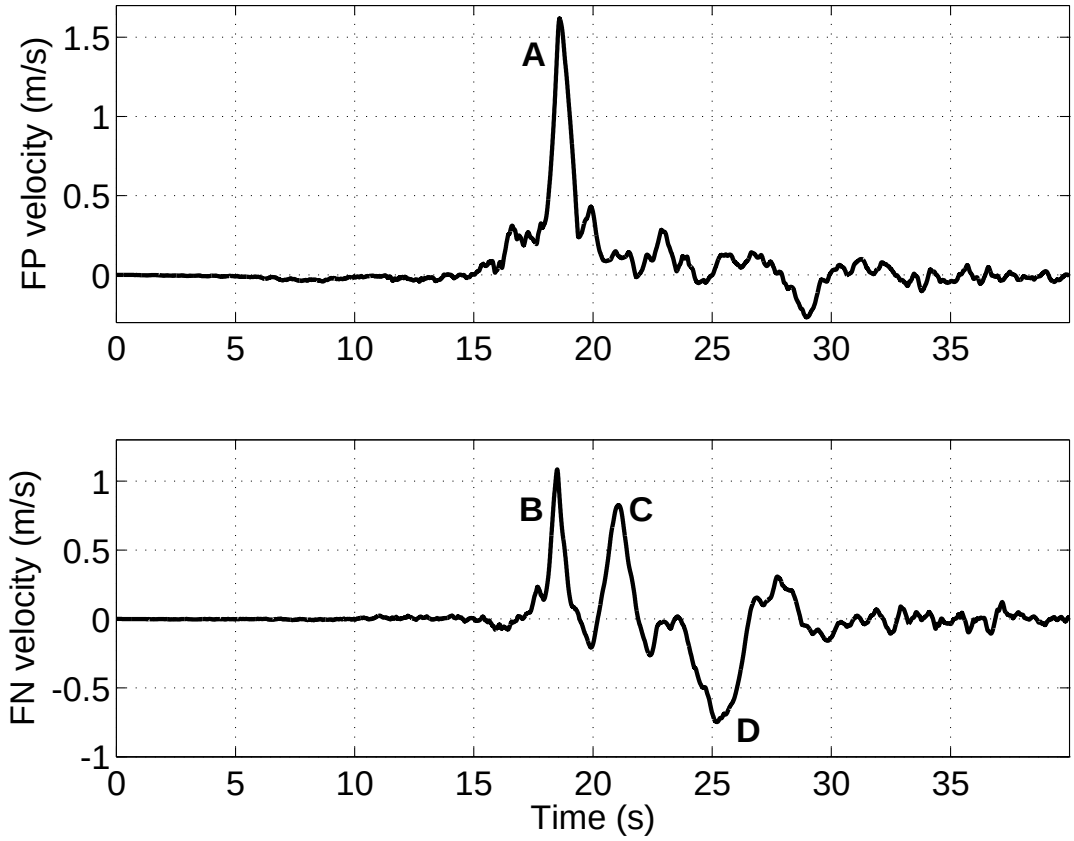

Figure 7.2: Instrument-corrected ground motions for PS10. The main velocity pulses are labeled to clarify discussion in the text. The record begins at the P wave arrival from the thrust event at 22:12:56.36 UTC (Ellsworth et al., 2004).

that exhibit a transition from sub-Rayleigh to supershear rupture speeds; as such, they are a uniquely transient feature not present in steady-state solutions. A consideration of the dynamics of such a transition suggests that the breakdown in stress occurring behind the rupture front releases interface waves along the weakened fault that trail the faster-moving supershear front. These are essentially Rayleigh waves dispersed by friction, although, depending on the stability of the frictional sliding and rupture pulse width, these may be accompanied by a stress drop. These interface waves cause additional slip but carry almost all of their energy in FN motion (pulse C), hence their absence from the FP component.

As is well known, mode II cracks are allowed to propagate within two steady-state velocity regimes: either below the Rayleigh wave speed (sub-Rayleigh) or between the S and P wave speeds (supershear). Propagation between the Rayleigh and S wave speeds is associated with energy generation rather than dissipation within the breakdown zone, indicating that these velocities should be rejected as unphysical. Theoretical studies suggested the possibility of supershear ruptures, beginning over three decades ago with a study by Burridge (1973) of the self-similarly expanding mode II crack with a critical stress fracture criterion. His analytical solution showed that as a sub-Rayleigh crack extends, a peak in shear stress traveling at the S wave speed develops ahead of the crack tip. For prestress levels sufficiently close to the critical stress, this peak exceeds the critical level and

could initiate a supershear rupture. This was later confirmed by the numerical experiments of Andrews (1976), which extended the fracture criterion to a more realistic condition requiring finite energy dissipation for crack growth.

Seismological observations suggest that supershear propagation has occurred, at least locally, in a number of crustal strike-slip events. Archuleta (1984) concluded that rupture velocities exceeding the *S*-wave speed were necessary to explain records from the 1979 Imperial Valley event. Strong motion recordings of the 1999 Izmit and Düzce events suggest supershear growth, at least in one direction (Bouchon et al., 2000, 2001). Waveform modeling of regional records from the 2001 Kunlunshan earthquake also indicates supershear velocities (Bouchon and Vallée, 2003).

Recent laboratory studies by Rosakis and coworkers (Rosakis et al., 1999; Xia et al., 2004) provided experimental verification of supershear crack growth. Several numerical (Geubelle and Kubair, 2001; Fukuyama and Olsen, 2002; Dunham et al., 2003) and analytical (Huang and Gao, 2001, 2002; Samudrala et al., 2002; Kubair et al., 2002; Guo et al., 2003b) studies have focused on properties of and mechanisms for triggering supershear propagation.

7.3 Spontaneous Modeling

We construct a simple rupture model exhibiting a transition from sub-Rayleigh to supershear propagation, and show that the ground motion explains several features recorded at PS10. We use a staggered-grid finite difference code with second order explicit time stepping (Favreau et al., 2002). The method converges spatially at eighth order away from the fault and has perfectly matched layer absorbing boundaries on all sides, except the free surface, to prevent artificial reflections from contaminating the solution. Slip is constrained to be horizontal, rendering the dynamics insensitive to the absolute stress level. Reverse slip is prohibited.

Since the station is located only 3 km from the Denali fault and many tens of kilometers from the Susitna Glacier and Totschunda faults, we model the rupture process on only one straight fault segment. The dynamic inverse problem pushes the limits of current computational capabilities (Peyrat and Olsen, 2004), so we use trial and error forward modeling. For simplicity, and to demonstrate that a supershear transition is the only feature required to match the ground motion, we assume that all material and frictional properties are uniform with depth.

We use a simple friction law that exhibits both slip-weakening and healing behaviors. The two parameter law requires that a slip-weakening distance D

and healing time T be specified at each point on the fault. We define the non-dimensionalized stress as $\theta = (\sigma_{xy} - \sigma_f)/(\sigma_y - \sigma_f)$, where σ_y and σ_f are the yield stress and sliding friction. The stress evolves following

$$\dot{\theta} = -\frac{\theta \delta v}{D} + \frac{1-\theta}{T} \tag{7.3.1}$$

once the fault begins to slip. Slip velocity is defined as $\delta v = v_x(y = 0^+) - v_x(y = 0^-)$ and reverse slip is forbidden. This friction law was introduced by Nielsen and Carlson (2000), and provides a convenient way to include healing. For $T \to \infty$, it reduces to an exponential slip-weakening law. Note that the slip-weakening distance D for this model is twice that used in the standard linear slip-weakening model (Andrews, 1976) having the same fracture energy.

We artificially nucleate the rupture by slightly overstressing a region 61 km from the station, chosen to match the distance to the intersection of the Susitna Glacier and Denali faults. As several models have suggested (Harris et al., 1991; Harris and Day, 1993; Kase and Kuge, 1998; Magistrale and Day, 1999; Anderson et al., 2003), ruptures jump between faults almost exclusively when the initial rupture reaches the edge of the original fault. Dynamic modeling of the transfer from the Susitna Glacier to Denali fault by Aagaard et al. (2004) suggests that this occurs about 10 s after initiation. The arrival time of pulses A and B then places a lower bound on the average rupture velocity from the intersection of

the faults to PS10 of $0.75c_s$, neglecting any time spent during nucleation on the Denali fault. Assuming that pulses A and B are associated with a supershear rupture (propagating at about $1.5c_s$) and pulse C with a Rayleigh wave, then the separation in time between these pulses requires the supershear transition to have occurred about 30 km before PS10. Combined with the assumption that slip transfers from the Susitna Glacier fault to the Denali fault about 10 s after nucleation (Aagaard et al., 2004), we estimate an initial sub-Rayleigh rupture speed of about 0.5-0.6c_s. In our models, the rupture begins bilaterally on the Denali fault, but we introduce a barrier 10 km to the west, consistent with surface slip measurements (Eberhart-Phillips et al., 2003), that arrests propagation in that direction. The initial stress level is selected such that the rupture is sub-Rayleigh, and no healing is used initially.

We distinguish between two types of supershear transitions observed in our simulations. In the first, the S wave stress peak that triggers the transition is released during nucleation (as in Andrews (1976)). Even for a properly resolved nucleation process with the slip-weakening laws used, an overestimate of the critical crack length (due to using an inappropriately large value of the slip-weakening distance) will result in a physically premature transition. If ruptures nucleate from much smaller patches and the slip-weakening distance that governs fully dynamic propagation is much larger than that governing nucleation (as experimental and

numerical work indicates), then numerical results exhibiting this type of transition are incorrect. Instead, a preferable type of transition would be one in which nucleation generates a negligible shear diffraction peak and some other process, such as growth into a region of increased stress drop (Fukuyama and Olsen, 2002) or focusing by rupture front curvature (Dunham et al., 2003), builds the peak to a critical level. To ensure this, we trigger the supershear transition by increasing the initial stress level in an asperity beginning about 30 km from the hypocenter (see Fig. 6), and make sure that diffractions from the nucleation process have negligible influence on rupture growth.

The short rise times at PS10 are inconsistent with a traditional crack model, indicating that the actively slipping region is quite narrow, as appears to be typical in the earth (Aki, 1968; Archuleta and Day, 1980; Heaton, 1990). Several mechanisms are known to generate rupture pulses, which are recognized as an alternative and equally valid solution to the elastodynamic equation (Freund, 1979; Broberg, 1999a; Nielsen and Madariaga, 2004). Strong slip rate weakening is one possibility (Cochard and Madariaga, 1994; Madariaga and Cochard, 1994; Perrin et al., 1995; Zheng and Rice, 1998). A friction law containing restrengthening on a short time scale can also generate rupture pulses (Nielsen and Carlson, 2000). Rupture pulses also result from interaction with geometrical heterogeneities, such as strength heterogeneities or fault borders that transmit arrest phases to initi-

ate healing (Archuleta and Day, 1980; Day, 1982a; Johnson, 1990; Beroza and Mikumo, 1996).

We present three models. The first (I) allows slip to 10 km depth and lacks healing. With these constraints, we were unable to match the short rise time on the FP component. Decreasing the slip-weakening distance does not alter the FP rise time, and actually makes FN pulse B too narrow. Instead, we tried two approaches to decrease the rise time. Our second model (II) allows slip to 10 km depth but adds a healing time of order one second (only within the asperity region). In these first two models, a healing front emanates from the western side of the Denali fault when the rupture arrests there, creating a rupture pulse about 16 km wide. The pulse width remains constant until the rupture encounters the region of high prestress, where the supershear transition begins. The third model (III) lacks healing, but restricts slip to 5 km depth. In this case, the rupture pulse width is about 8 km, and is controlled by the fault width rather than by the stopping phase from the western end of the fault. The model parameters and fault geometry are summarized in Table 7.1 and Fig. 7.3. Snapshots of the rupture history of our models are shown in Fig. 7.4 and Movies 1-3. Fig. 7.5 compares our synthetics to the corrected data. We allow a linear shift in time since the nucleation process is artificial. We scale the amplitude of our synthetics to match pulse A identically; this sets the magnitude of the stress drop $\sigma_y - \sigma_f$ (Table 7.1).

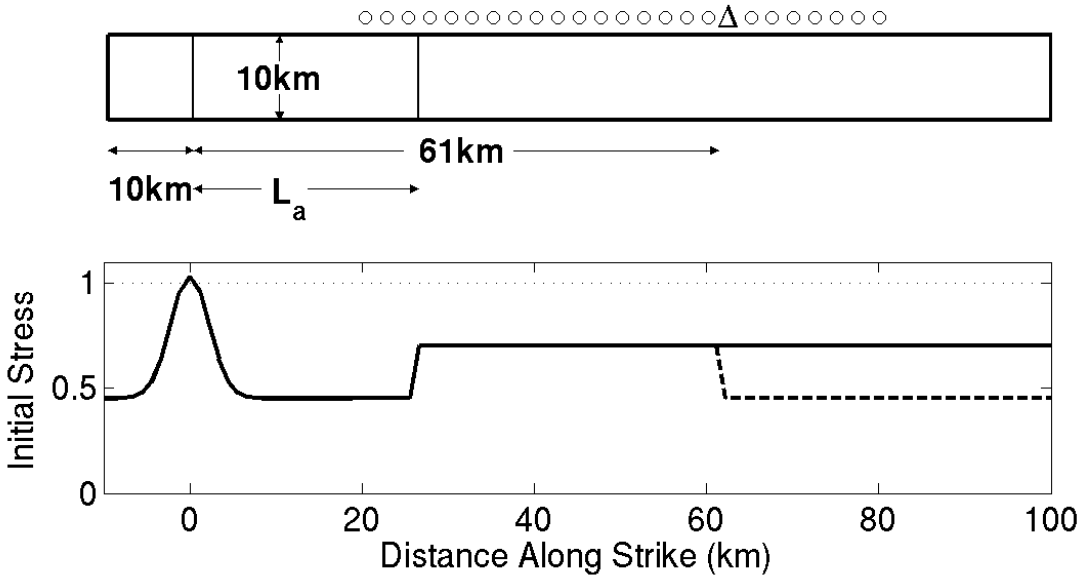

Figure 7.3: Model fault geometry and initial stress conditions (the solid line corresponds to model I; see table 1 for the parameters of the other models) used in the spontaneous rupture calculations. PS10 is marked with a triangle. Hypothetical stations spaced every 2.5 km between 20 km and 80 km, where we also compute ground motions, are denoted by small circles. L_a denotes the distance to the asperity, approximately 30 km. The initial stress profile marked by the dashed line shows the minimum width of the asperity required by the record of PS10, as discussed at the end of the text.

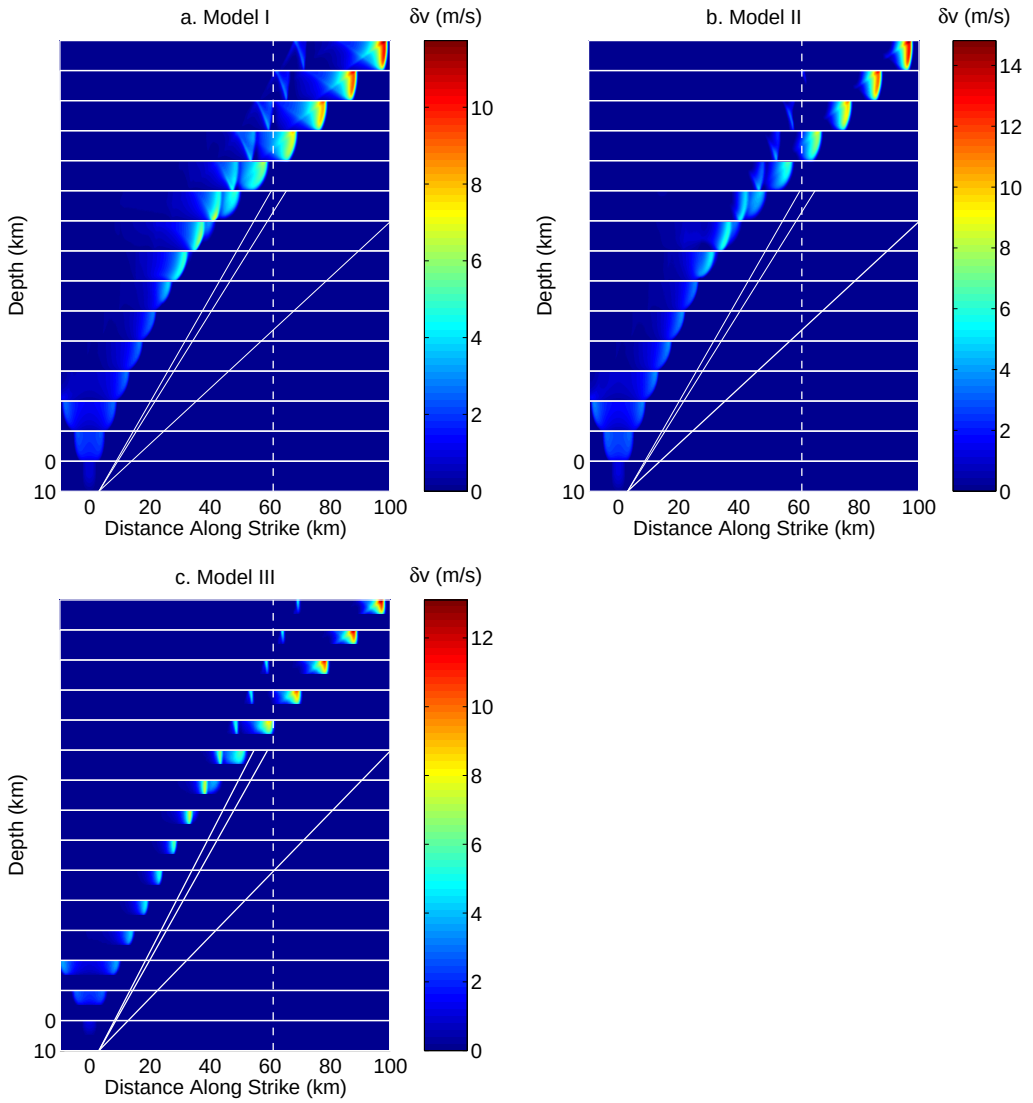

Figure 7.4: Snapshots of the fault surface with the color scale measuring slip velocity for (a.) model I (no healing, slip to 10 km depth, shown every 1.83 s), (b.) model II (including healing, slip to 10 km depth, shown every 1.83 s), and (c.) model III (no healing, slip to 5 km depth, shown every 1.65 s). Time advances from bottom to top. The solid white lines show wave speeds (Rayleigh, S, and P from bottom to top). The dashed white line marks the position of the station.

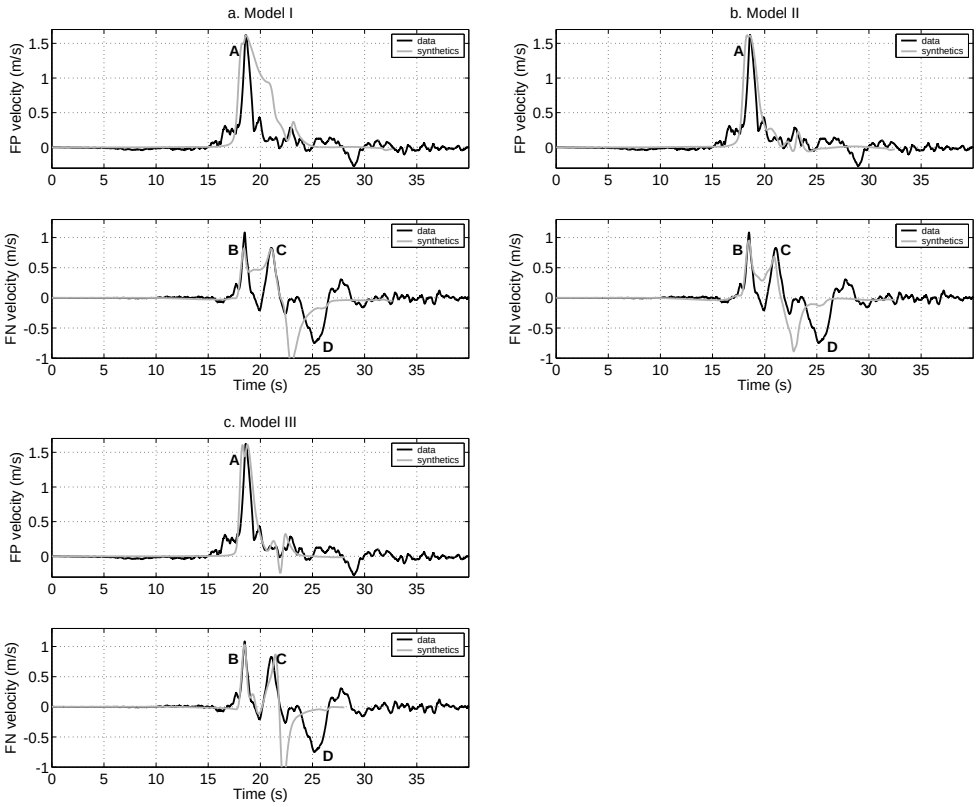

Figure 7.5: Comparison between recorded and synthetic ground motions at PS10 for (a.) model I (no healing, slip to 10 km depth), (b.) model II (including healing, slip to 10 km depth), and (c.) model III (no healing, slip to 5 km depth).

parameter	model I	model II	model III
μ		32.4GPa	
c_s		3.4km/s	
c_p		5.89km/s	
grid spacing Δx		125m	
time step Δt		4.09ms	
distance to station		61km	
distance to asperity L_a	24.375km	27.375km	28.75km
fault width	10km	10km	5km
θ (outside asperity)	0.45	0.45	0.7
θ (within asperity)	0.7	0.77	0.87
$\sigma_y - \sigma_f$	28.4MPa	40.0MPa	31.5MPa
D	1.43m	2.01m	1.58m
T	∞	1.47s	∞

Table 7.1: Parameters for our three models.

Let us begin with model I. When the rupture enters the region of increased prestress, the transient diffractions appear and accelerate the rupture from $0.65c_s$ to $1.6c_s$. It continues at the supershear velocity as it passes the station. The supershear rupture takes the form of a pulse of expanding width, with the healing front trailing at the S wave speed. The fault is locked after this healing front until the Rayleigh arrival, in accordance with the elastodynamic considerations discussed previously. This corresponds to the forbidden velocity region that occurs when the slip direction attempts to reverse itself. Our theoretical model also predicts a Rayleigh wave behind the supershear front, which manifests itself here as a secondary slip pulse. This model gives too large of a rise time on FP to be consistent with the data. In contrast, we find the width of FN pulses B and C to

be far less sensitive to the slip duration. However, the dip in amplitude between these pulses is controlled by the slip duration, and the strong dip seen in the data suggests that the fault has negligible slip between the supershear rupture front and the secondary Rayleigh rupture pulse.

There are several features that are not predicted by the two dimensional theoretical model, which neglects both the finite width of the fault and the free surface. The propensity of ruptures near the free surface to become supershear has been noted by several researchers (Aochi, personal communication, 2002) (Gonzalez, 2003), and is related to phase conversion at the free surface. This phenomenon can be seen in Fig. 7.4 and Movies 1-3, in which the supershear rupture front emerges at the free surface and spreads laterally down the rupture front. Note also the change in the slip velocity pattern across a line extending back from where the rupture front meets the free surface, as well as where it intersects the bottom edge of the fault (particularly evident in the last several snapshots). The angle that this line makes with the horizontal is the S wave Mach angle, indicating that behind this wavefront, S waves converted by the free surface cause increased slip velocity.

In model II, we add frictional healing to decrease the rupture pulse width. In this case, the healing front follows at approximately the same speed as the supershear rupture front. To match the short rise time of pulse A requires a

healing time T of order one second (Table 7.1). This generates a complicated stress history on the fault because there is an additional stress drop associated with the secondary slip pulse. Healing raises the stress levels such that a sufficiently large perturbation (provided by the Rayleigh wave) destabilizes the frictional sliding to generate a secondary rupture. This does not occur in the previous model, where the secondary slip pulse is closer to a true Rayleigh wave that propagates without altering the fault tractions. However, the healing is too strong for the secondary pulse to persist, and it dies out after propagating about 30 km.

This healing time does not necessarily imply a rapid restrengthening, but may be interpreted as evidence of a characteristic time arising from some unmodeled source process that locks the fault. Such a value could be related to a smaller length scale characterizing strength or stress heterogeneities, which has been shown to control the rupture pulse width (Beroza and Mikumo, 1996). We test this hypothesis in model III, which introduces the smaller length scale simply by limiting slip to 5 km depth. This achieves a comparably short rise time without the use of healing. In this case, the rupture pulse width is controlled by the fault depth, as in Day (1982a). The healing front moves at the same speed as the supershear rupture front.

The amplitude and duration of pulses A, B, and C are well matched for models II and III. The simplicity of our models allows us to explain the relationship

between fault processes and the ground motion pulses. We show the evolution of FP and FN ground motions for model III as the rupture transitions to supershear velocities in Fig. 7.6, and for all models in Movies 4-9. We also present seismograms for this model at hypothetical stations before and after PS10 in Fig. 7.7, which highlight the fact that the PS10 record exhibits characteristics of both supershear and sub-Rayleigh ruptures.

Before encountering the high stress region, the radiation pattern is characteristic of steady-state sub-Rayleigh ruptures in that FN dominates FP in amplitude. The FP radiation pattern is characterized by four lobes (nodal on the fault plane) that give rise to two one-sided pulses recorded at a fixed receiver. The pattern is effectively that of a dislocation source. On the right-moving block, the FN motion preceding the rupture is away from the fault and trailing the rupture is in toward the fault. This results in the typical two-sided FN pulse. These characteristic motions are discussed by Archuleta and Hartzell (1981); Hall et al. (1995) and were observed, for example, in the 1966 Parkfield earthquake (Aki, 1968). As the rupture pulse length increases (approaching a crack model), the two trailing lobes on FP coalesce into a large tail. In addition, the downward FN motion arrives later and diminishes in amplitude. The downward motion is thus directly associated with the passage of the healing front.

Evidence of the supershear transition on the FP component comes as the rup-

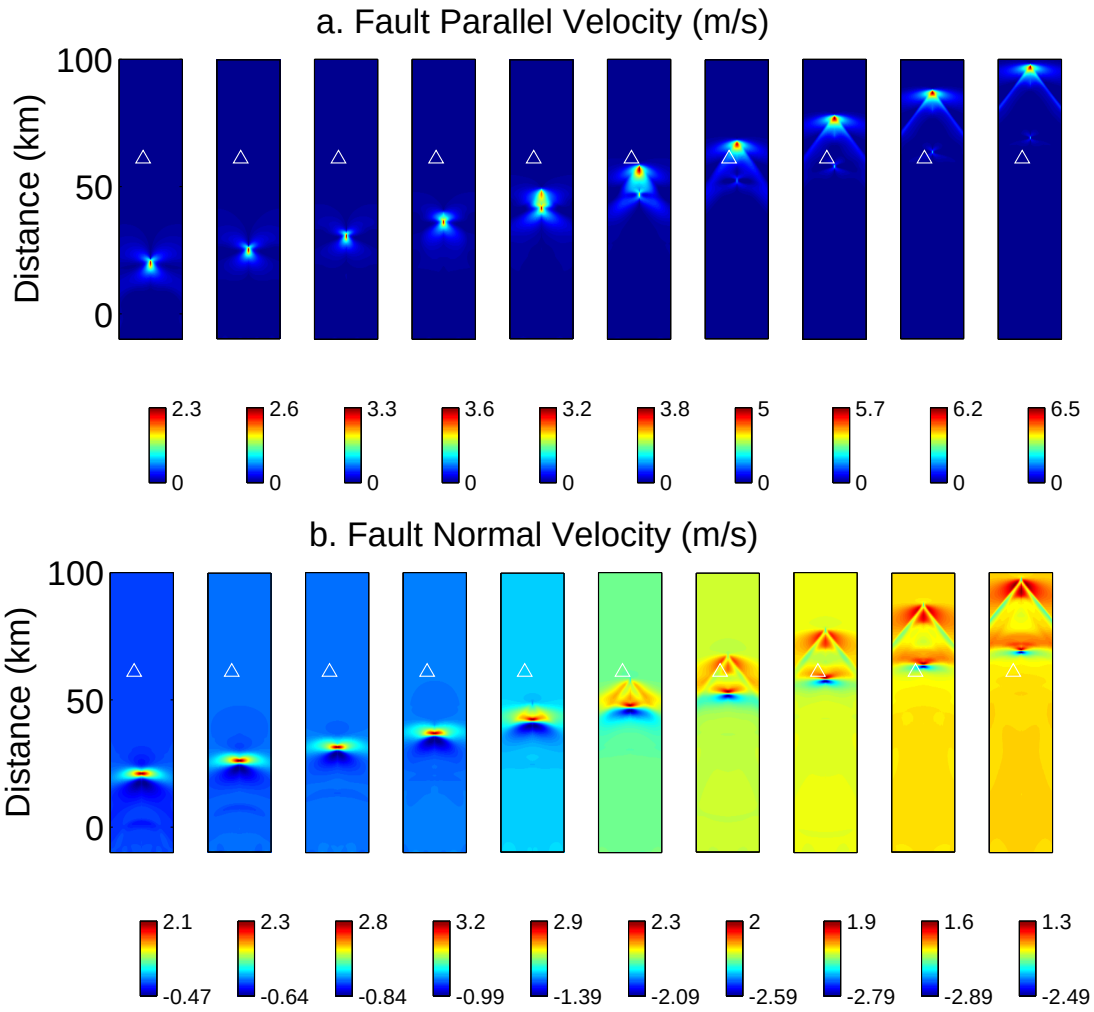

Figure 7.6: Snapshots of of the free surface showing (a.) fault parallel and (b.) fault normal ground motion every 1.28 s from left to right for model III, on an area extending 12.5 km to either side of the fault. Other models produce similar ground motion. The color scale, which changes for each snapshot, measures FP or FN velocity. Although the FP motion is antisymmetric across the fault, it is plotted as symmetric for visualization purposes. The location of PS10 is marked by the white triangle.

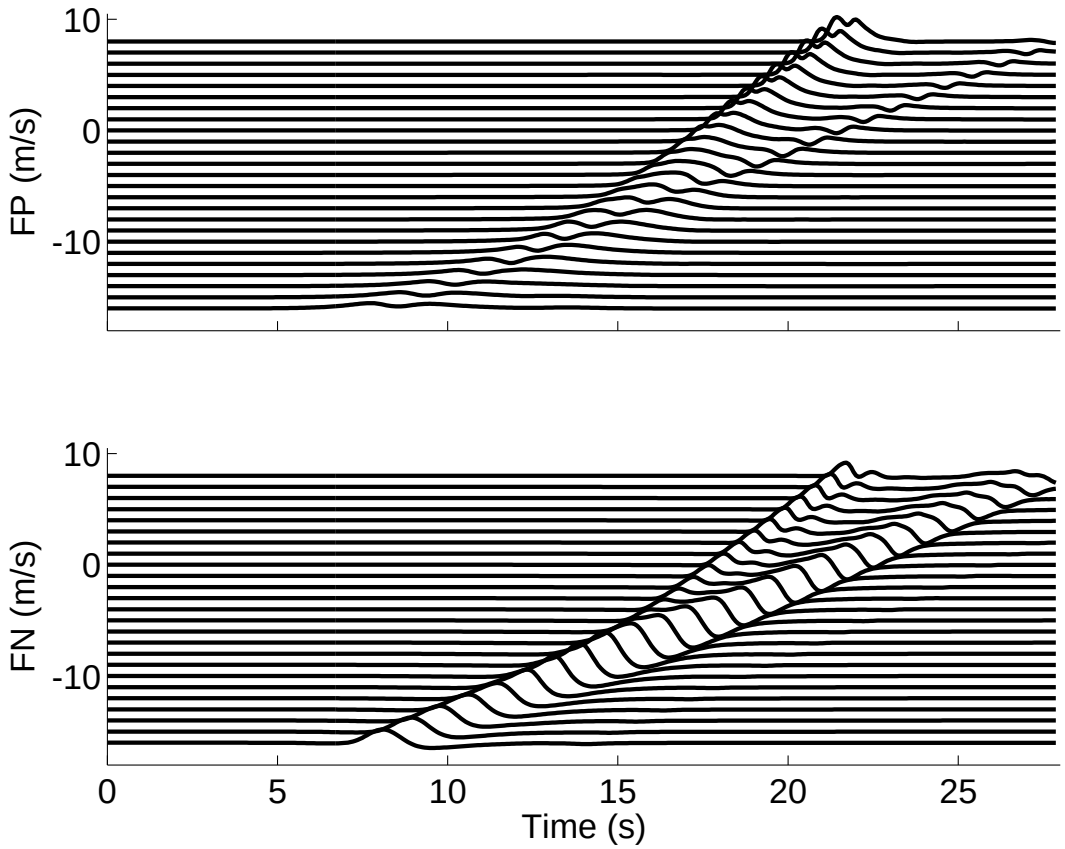

Figure 7.7: Particle velocities for model III recorded at a number of hypothetical stations every 2.5 km from 20 km to 80 km along a line parallel to and 3 km off the Denali fault, as shown in Fig. 7.3. Adjacent traces are offset by 1 m/s with the record corresponding to the station at 60 km centered about zero.

ture begins to outrun the S waves, which ultimately lie behind a planar wavefront emanating from the rupture front in a Mach cone. Arrival of this wavefront gives rise to the large one-sided pulse (A). The amplitude of this feature increases as the supershear rupture develops, until its amplitude dominates the FP motions (see Fig. 7.7). In addition to the planar shear wavefront, the fully developed supershear rupture possesses a two-lobed pattern preceding the main shear wavefronts that must arise from P waves. The lack of a preliminary bump preceding pulse A indicates that the rupture was not in steady-state conditions as it passed the station. The small rise and plateau before pulse A arrives much too early to be an indication of this feature. The trailing Rayleigh wave has negligible signature in the FP ground motion.

The pattern of FN ground motion associated with the supershear transition is more complex. A pair of one-sided pulses, with motion away from the fault on the right-moving block, begin to emanate from the supershear rupture front along the planar S wavefronts. These grow in amplitude as steady-state supershear conditions are reached and correspond to pulse B. Note that the motion actually peaks slightly before FP pulse A, consistent with the observations. This is because the motion actually preceeds the Mach cone. This motion decreases to a minimum between pulses B and C. Pulse C corresponds to the Rayleigh wave, and is similar in characteristic to a typical subshear rupture. The dip between these peaks likely

indicates that the fault has no significant slip between the supershear rupture front and the Rayleigh wave. The amplitude of the trailing Rayleigh wave is particularly sensitive to the frictional evolution of the fault. If accompanied by too large of a stress drop (as could occur if the fault rapidly restrengthens), the Rayleigh wave develops into a strong secondary rupture, accompanied by an amplitude increase in these later motions. Also, if the triggering prestress is too large, the majority of the energy goes into supershear motions at the expense of the Rayleigh pulse. This places a strong constraint on the triggering prestress in our models, and we find it to be just barely above the minimum required to initiate the supershear transition.

We did not find it possible to exactly fit the negative FN pulse D. A similar negative motion appears after the passage of a dislocation, and is associated with the healing front in a rupture pulse model. An examination of the rupture histories shows that our models exhibit an extremely narrow Rayleigh rupture pulse that causes the negative FN pulse to arrive immediately after pulse C. We speculate that pulse D corresponds to the passage of a healing front associated with a Rayleigh pulse roughly twice as wide as observed in our models. In our models, the Rayleigh wave is likely to be narrow because finite difference methods have difficultly resolving surface waves. Furthermore, broadening of the Rayleigh wave could also occur due to frictional dispersion, as is characteristic of any friction

law possessing intrinsic time or length scales. Further work is needed to test this hypothesis, but if true, then this record could provide valuable constraints on the frictional properties of slipping faults.

7.4 Discussion

We have analyzed strong ground motion recordings from the 2002 Denali Fault earthquake and conclude that they provide evidence of supershear rupture propagation past PS10. A study of the waves generated within the stress breakdown zone behind the rupture front sheds light on how the forces that drive supershear propagation are transmitted to the unbroken region ahead of the rupture front. As noted by Ellsworth et al. (2004), a supershear rupture leads to large amplitudes on both the FP and FN components of motion. Rupture growth into a region of increased stress drop triggers a set of transient diffractions that accelerate the rupture from sub-Rayleigh to supershear velocities. This process is accompanied by the release of a Rayleigh wave on the fault surface. This appears as a secondary slip pulse that manifests itself primarily in FN ground motion, explaining late arriving FN pulses recorded at PS10 that are not explained in supershear kinematic models. The separation in time of these FN pulses indicates that the supershear transition occurred about 30 km before PS10.

While our models show persistent supershear rupture well after PS10, this is not required by the records of PS10 and occurs only because the high prestress level used to trigger supershear growth is maintained thereafter. To place a lower bound on the supershear propagation distance required to match the PS10 record, we limited the width of the high stress region (Fig. 7.3). We found that a minimum width of about 35 km is required to match the records. In this case, the supershear rupture is transient. It persists beyond the high stress region and dies out about 30 km past PS10. When the secondary Rayleigh rupture pulse encounters this region, it resumes its role as the only rupture front.

The narrow width of pulse A and the strong dip in amplitude between pulses B and C are incompatible with a traditional crack model, indicating that the supershear rupture took the form of a narrow slip pulse. The same cannot be concluded for the secondary Rayleigh rupture pulse, which we speculate was about twice as broad as the pulse observed in our simulations. Our dynamic models demonstrate that a narrow supershear pulse could arise either from frictional healing over a time scale of 1.5 s or from the presence of a 5 km length scale characterizing the stress distribution. While the rupture histories of these models differ (Fig. 7.4 and Movies 1-3), the resulting ground motion at PS10 is nearly identical (Fig. 7.5). In light of this, we emphasize that our models should not be interpreted as providing an exact slip history of the fault, which cannot be determined uniquely from one

record. Instead, our models contain only the minimum number of parameters required to explain the main features of the record.

The multiple slip pulses that we observe in our dynamic models highlight the difficulty kinematic models may have when fitting or inverting data that result from supershear ruptures, particularly if supershear growth occurs in transient bursts. Dynamical inversion efforts like those by Peyrat and Olsen (2004), while presently extremely expensive computationally, are a possible future solution.

7.5 Relationship to Steady State Solutions

Pump Station 10 from the Denali Fault earthquake offers the best near-source record of a supershear rupture; however, the station captured waveforms resulting from a particularly non-steady rupture process and exhibits motions characteristic of both supershear and subshear ruptures (Fig. 7.8). In the dynamic model by Dunham and Archuleta (2004), the rupture accelerates from $0.6c_s$ to $1.5c_s$ approximately 25km before the station. This process generates a secondary slip pulse moving at the Rayleigh speed. Ground motion pulses A and B (which have a large FP to FN ratio) are generated by the supershear rupture, while pulses C and D (almost entirely on the FN component) arise from the secondary slip pulse. The rapid downward swing in pulse B marks the arrival of the shear field (compare

with Fig. 5.2d). Direct extraction of the slip velocity function from the record is not possible for two reasons. The transient emergence of the supershear rupture just prior to the station causes nearly simultaneous arrival of the dilatational and shear field. Furthermore, motions from the secondary slip pulse appear in the tail of the supershear motions. The two-sided FN motions (C and D) are exactly those expected from a subshear slip pulse (Fig. 5.1b), with C being associated with the leading edge of the slip zone and D with the trailing edge. This constrains the width of the slip pulse to approximately 15 km, much larger than appears in the model by Dunham and Archuleta (2004), who chose parameters to match the narrowness of pulses A and B (at the expense of truncating the width of the secondary slip pulse). The record leaves an open question: What type of rupture process or friction law results in a remarkably narrow supershear rupture pulse but quite broad subshear slip pulse?

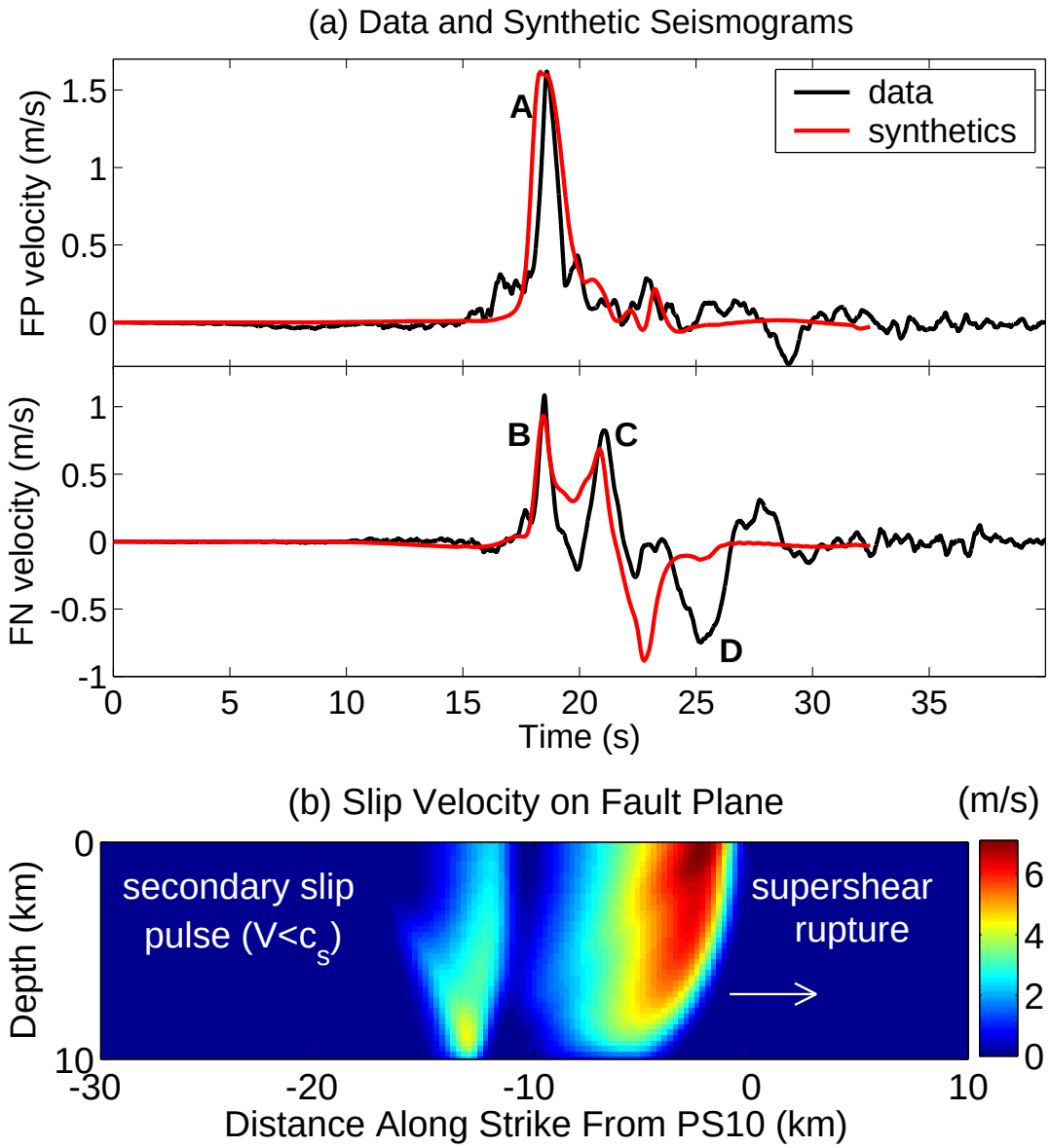

Figure 7.8: Data and synthetic seismograms at Pump Station 10 (PS10) (a) and a snapshot of the slip velocity on the fault plane (b) for the 2002 Denali Fault earthquake from the dynamic model by Dunham and Archuleta (2004).

Chapter 8

Conclusion

The near-source ground motion of earthquakes is of particular interest in seismology. On one hand, it is responsible for the loss of buildings and life, while on the other hand, it offers the most complete set of information regarding the source process. Our focus in this work has been how the character of this ground motion changes with rupture speed, in particular when it exceeds the S-wave speed.

Material failure processes within fault zones release the strain energy stored within the surrounding medium, leading to frictional dissipation and the generation of seismic waves. These waves transmit shearing stresses to the unbroken region ahead of the rupture, allowing for further material failure. In this thesis, we have examined in detail the properties of these elastic waves, including their interaction with the frictionally sliding portion of the fault and eventual diffraction off of the rupture front. Much of the focus was devoted to the two-dimensional mode II rupture geometry, which is the dominant mode for crustal strike-slip earthquakes. In this case, waves with phase velocities up to the Rayleigh wave speed, as well as those in the intersonic region between the S- and P-wave speeds, transmit shearing stresses that extend the rupture. Those with phase velocities between the Rayleigh and S-wave speeds transmit stresses of the opposite sign. This leads to the existence of two rupture propagation velocity regimes: sub-Rayleigh and intersonic, or as more commonly known in seismology, supershear.

The limiting velocity of three-dimensional or mixed-mode ruptures is more complicated, since the direction of slip breaks the symmetry of the rupture process and the amplitude of excited P and S waves varies anisotropically within the plane of the fault. To address this question, we studied the three-dimensional problem of wave propagation in the vicinity of a frictionally sliding interface. Steady sliding between two identical elastic half-spaces is stable with respect to slip perturbations at any orientation with respect to the original sliding. Friction introduces a preferred direction of slip. Transverse motions encounter an effectively viscous frictional resistance that increases with transverse slip velocity, damping waves in the vicinity of the interface. Friction further influences wave propagation by coupling the SH (antiplane) and P-SV (inplane) wave systems. The source-free response is characterized by the existence of damped interface waves, whose phase velocity depends on both the steady state conditions and the direction of propagation with respect to the initial sliding direction. Two allowed propagation velocity regimes exist in each direction, with the tendancy for supershear ruptures greatly accentuated in the mode II direction.

The ground motion from supershear ruptures was our next focus. As a starting model, we examined the two-dimensional problem of steady state ruptures for speeds within both the sub-Rayleigh and supershear regimes. Synthetic seismograms demonstrate that coherent high-frequency information about the source

process rapidly attenuates with distance from the fault for sub-Rayleigh ruptures. Such records provide almost no resolution of the spatial extent of the stress breakdown zone. At supershear speeds, S waves radiate away from the fault to form a Mach front. These waves preserve the full source spectrum and carry an exact history of the slip velocity on both the fault-parallel and fault-normal components of motion, whose amplitudes are given by a function of rupture speed that vanishes at $\sqrt{2}$ times the S-wave speed. The waves generate particularly large peak ground velocities and accelerations at unexpectedly far distances from the fault. The extent of the breakdown zone, which is quite unimportant in determining the ground motion for sub-Rayleigh ruptures, becomes a critical parameter. Numerical modeling of these ruptures requires the use of large values for the breakdown zone size. If these values are much larger than those existing within the earth, as the scaling of laboratory measurements indicate, this will lead to significant underestimation of the peak ground motion.

We analyzed strong ground motion recordings from the 2002 Denali Fault earthquake, concluding that they provide evidence of supershear rupture propagation past a near-source seismograph station along the Trans Alaska Oil Pipeline, pump station 10 (PS10). Rupture growth into a region of increased stress release prior to PS10 triggers a set of transient diffractions that accelerate the rupture from sub-Rayleigh to supershear velocities. This process is accompanied by the

release of a Rayleigh wave on the fault surface. This interface wave appears as a secondary slip pulse that manifests itself primarily in fault normal ground motion, explaining late-arriving fault normal pulses recorded at PS10 that are not explained in supershear kinematic models. The separation in time of these fault normal pulses indicates that the supershear transition occurred about 30 km before PS10. The minimum total distance of supershear propagation required to match the records is approximately 65 km.

The narrow width of the recorded ground motion pulses are incompatible with a traditional crack model, indicating that the supershear rupture took the form of a narrow slip pulse. The same cannot be concluded for the secondary Rayleigh rupture pulse, which we speculate was about twice as broad as the pulse observed in our simulations. Our dynamic models demonstrate that a narrow supershear pulse could arise either from frictional healing over a time scale of 1.5 s or from the presence of a 5 km length scale characterizing the stress distribution. While the rupture histories of these models differ, the resulting ground motion at PS10 is nearly identical. In light of this, we emphasize that our models should not be interpreted as providing an exact slip history of the fault, which cannot be determined uniquely from one record. Instead, our models contain only the minimum number of parameters required to explain the main features of the record. The multiple slip pulses that we observe in our dynamic models highlight the diffi-

culty kinematic models may have when fitting or inverting data that result from supershear ruptures, particularly if supershear growth occurs in transient bursts.

The theoretical and observational work that we conducted argues for the inclusion of supershear ruptures in seismic hazard analysis. The generation of an *S*-wave Mach front leads to extremely impulsive ground motion that persists far from the fault. Evidence for the existence of supershear ruptures in nature is quite solid, coming from both laboratory studies and seismic observations. The unanswered question that must be addressed is how often these ruptures occur, and on which faults will they appear.

Appendix A

Appendices to Chapter 4

A.1 Roots of the Dispersion Relation

We can use the argument principle to demonstrate that depending on the value of η, either two or three roots exist to the dispersion relation (4.5.1). This method was used by Cagniard (1962) in his study of the existence of interface waves for two solids in welded contact and by Achenbach (1973) for the Rayleigh function. First, we recast the dispersion relation (4.5.1) in terms of wave slowness, setting $q = 1/\Omega$, $d = 1/c_p$, and $s = 1/c_s$:

$$D(q) = \eta^{-1} s^{-1} (s^2 - q^2)^{1/2} R + R \cos^2 \phi + s^2 (s^2 - q^2) \sin^2 \phi, \qquad \text{(A.1.1)}$$

where $R = 4q^2(d^2-q^2)^{1/2}(s^2-q^2)^{1/2} + (s^2-2q^2)^2$. The function is rendered single valued by making a branch cut along the real axis in the complex q-plane between $\pm s$. The sign of the radicals is given as follows, where (+,-) denotes a positive real part and negative imaginary part: quadrant I (-,+), II (-,-), III (+,-), IV (+,+). The number of zeros Z, including multiplicity, of $D(q)$ within a closed contour Γ is given by

$$Z = \frac{1}{2\pi \mathrm{i}} \int_\Gamma \frac{D'(q)}{D(q)} dq, \tag{A.1.2}$$

since $D(q)$ has no poles. We consider Γ to be composed of two sections: Γ_∞, a counterclockwise circle at infinity, and Γ_{br}, a clockwise path surrounding and infinitesimally close to the branch cut (see Fig. A.1). We consider the function $D(q)$ as a mapping of the complex q-plane to the complex D-plane, and let $\Gamma' = \Gamma'_\infty + \Gamma'_{br}$ be the image of Γ. Thus,

$$Z = \frac{1}{2\pi \mathrm{i}} \int_{\Gamma'} \frac{dD}{D}, \tag{A.1.3}$$

which is just the number of times that Γ' encircles the origin.

Let us first consider Γ_∞. For $\eta \to 0$, we drop the last two terms. For large q, $R = 2q^2(d^2 - s^2)$ and thus $D = \mathrm{i}\eta^{-1}s^{-1}(d^2 - s^2)q^3$. Γ'_∞ encircles the origin three times, giving three roots. For $\eta \to \infty$, we drop the first term and $D =$

$[2(d^2-s^2)\cos^2\phi - s^2\sin^2\phi]q^2$, giving only two roots. Finally, for arbitrary nonzero η, the first term dominates and the path contributes three roots.

The image of Γ_{br} is somewhat complicated. We define the contour formally as two line segments running parallel to the real axis, the first just above the axis from $q = -s + \mathrm{i}\epsilon$ to $q = s + \mathrm{i}\epsilon$, and the second just below the axis from $q = s - \mathrm{i}\epsilon$ to $q = -s - \mathrm{i}\epsilon$. The segments are connected with semicircular contours centered on the branch points $q = \pm s$ with radius ϵ. This is shown in Fig. A.1, along with several labelled reference points. The contour is interpreted in the $\epsilon \to 0$ limit, allowing us to expand for small ϵ. Values of $D(q)$ along the portion of the top line segment in quadrant II are given to leading order in ϵ as follows.

At A, $q = -s + \mathrm{i}\epsilon$ and

$$\begin{aligned} \Re D &= s^4\cos^2\phi \\ \Im D &= s^2\sqrt{\epsilon s}(-\eta^{-1}s + 4\sqrt{s^2-d^2}\cos^2\phi). \end{aligned} \tag{A.1.4}$$

Along $\overline{AB}$, $q = -p + \mathrm{i}\epsilon$ with $d < p < s$, and

$$\begin{aligned} \Re D &= (2p^2-s^2)^2(-\eta^{-1}s^{-1}\sqrt{s^2-p^2} + \cos^2\phi) + s^2(s^2-p^2)\sin^2\phi \\ \Im D &= 4p^2\sqrt{s^2-p^2}\sqrt{p^2-d^2}(-\eta^{-1}s^{-1}\sqrt{s^2-p^2} + \cos^2\phi). \end{aligned} \tag{A.1.5}$$

At B, $q = -d + \mathrm{i}\epsilon$ and

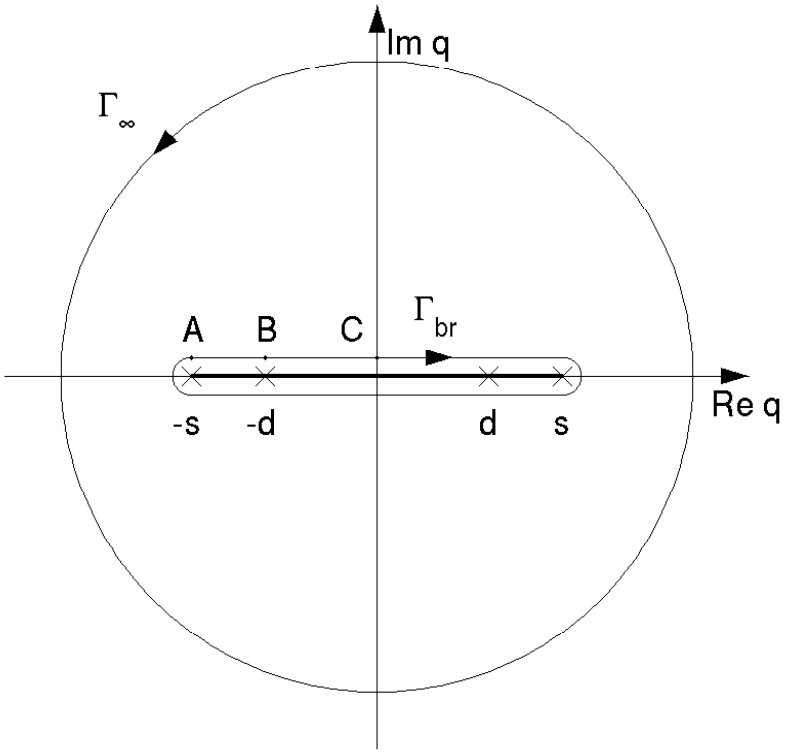

Figure A.1: Integration path in the complex slowness plane that encloses all potential roots of the dispersion relation. Shown also are the branch points and branch cuts.

$$\begin{aligned}\Re D &= (2d^2 - s^2)^2(-\eta^{-1}s^{-1}\sqrt{s^2-d^2} + \cos^2\phi) + s^2(s^2-d^2)\sin^2\phi \\ \Im D &= 4d^2\sqrt{s^2-d^2}\sqrt{\epsilon d}(-\eta^{-1}s^{-1}\sqrt{s^2-d^2} + \cos^2\phi). \end{aligned} \tag{A.1.6}$$

Along $\overline{BC}$, $q = -p + \mathrm{i}\epsilon$ with $p < d < s$, and

$$\begin{aligned}\Re D &= (-\eta^{-1}s^{-1}\sqrt{s^2-p^2} + \cos^2\phi)\left[4p^2\sqrt{s^2-p^2}\sqrt{d^2-p^2} + (2p^2-s^2)^2\right] + \\ &\quad s^2(s^2-p^2)\sin^2\phi \\ \Im D &= 4\epsilon p(-\eta^{-1}s^{-1}\sqrt{s^2-p^2} + \cos^2\phi)\Bigg[2(s^2-2p^2) - \\ &\quad 2\sqrt{s^2-p^2}\sqrt{d^2-p^2} + p^2\left(\sqrt{\frac{s^2-p^2}{d^2-p^2}} + \sqrt{\frac{d^2-p^2}{s^2-p^2}}\right)\Bigg] - \\ &\quad \epsilon p\eta^{-1}s^{-1}\frac{4p^2\sqrt{s^2-p^2}\sqrt{d^2-p^2} + (2p^2-s^2)^2}{\sqrt{s^2-p^2}} + 2\epsilon p s^2\sin^2\phi. \end{aligned} \tag{A.1.7}$$

At C, $q = \mathrm{i}\epsilon$ and

$$\begin{aligned}\Re D &= (1-\eta^{-1})s^4 \\ \Im D &= 0. \end{aligned} \tag{A.1.8}$$

The above results are extended to calculate the image path for the remaining sections of Γ_{br} by noting several symmetries of the various terms. We write the dispersion relation as $D(q) = D_1(q) + D_2(q) + D_3(q)$, where the D_i are the three

terms as ordered in Eq. (A.1.1). Letting $q = q_R + \mathrm{i}q_I$ where q_R and q_I are real, we note that $D(-q_R+\mathrm{i}q_I)$ is the complex conjugate of $D(q_R+\mathrm{i}q_I)$. Thus, the sections of Γ'_{br} from q in quadrants I and III are the complex conjugates of the sections from q in quadrants II and IV, respectively. Furthermore, $\Re D_1(q_R - \mathrm{i}q_I) = -\Re D_1(q_R + \mathrm{i}q_I)$ and $\Im D_1(q_R - \mathrm{i}q_I) = \Im D_1(q_R + \mathrm{i}q_I)$, while $D_2(q_R - \mathrm{i}q_I) = D_2(q_R + \mathrm{i}q_I)$ and $D_3(q_R - \mathrm{i}q_I) = D_3(q_R + \mathrm{i}q_I)$. Thus, when $\Im q < 0$, $\Re D(q) > 0$; hence, only sections of Γ_{br} above the real axis can potentially have an image with negative real part.

We now show that for $\eta > 1$ the image path never encircles the origin, leaving a total of three roots for the dispersion relation, while for $\eta < 1$, the image path encircles once clockwise, leaving only two roots for the dispersion relation. Our proof rests on the following logic. For the image path to encircle the origin at least once, there must exist some q on Γ_{br} such that $\Re D(q) < 0$ when $\Im D(q) = 0$. We prove that this is either never true and $\Re D(q) > 0$ when $\Im D(q) = 0$, or that there is only one value of q on Γ_{br} such that $\Re D(q) < 0$ when $\Im D(q) = 0$, and as q moves through this point $\Im D(q)$ goes from negative to positive.

We consider the sign of $\Re D(q)$ when $\Im D(q) = 0$. If $\Im D = 0$ at A, $\Re D > 0$. Along $\overline{AB}$, $\Im D = 0$ when $-\eta^{-1}s^{-1}\sqrt{s^2 - p^2} + \cos^2\phi = 0$. At this point, $\Re D = s^2(s^2 - p^2)\sin^2\phi$, which is always positive. A similar argument shows that if $\Im D = 0$ at B, $\Re D = s^2(s^2 - d^2)\sin^2\phi$, which is always positive.

Along $\overline{BC}$, we write

$$\begin{aligned} \Re D &= fR + s^2(s^2-p^2)\sin^2\phi \\ \frac{\Im D}{\epsilon p} &= -\frac{\eta^{-1}R}{s\sqrt{s^2-p^2}} + 4fg + 2s^2\sin^2\phi, \end{aligned} \tag{A.1.9}$$

where

$$\begin{aligned} R &= 4p^2\sqrt{s^2-p^2}\sqrt{d^2-p^2} + (s^2-2p^2)^2 \\ f &= -\eta^{-1}s^{-1}\sqrt{s^2-p^2} + \cos^2\phi \\ g &= 2\left(s^2-2p^2-\sqrt{s^2-p^2}\sqrt{d^2-p^2}\right) + p^2\left(\sqrt{\frac{s^2-p^2}{d^2-p^2}} + \sqrt{\frac{d^2-p^2}{s^2-p^2}}\right). \end{aligned} \tag{A.1.10}$$

We will need that $g > 0$. This follows by noting that since

$$\sqrt{\frac{s^2-p^2}{d^2-p^2}} + \sqrt{\frac{d^2-p^2}{s^2-p^2}} > 2 \tag{A.1.11}$$

then

$$g > 2\sqrt{s^2-p^2}(\sqrt{s^2-p^2} - \sqrt{d^2-p^2}), \tag{A.1.12}$$

which is clearly positive. Next, using $\Im D = 0$ as a constraint, we can write

$$\Re D = \frac{\eta^{-1}R^2}{4gs\sqrt{s^2-p^2}} + \frac{s^2\sin^2\phi[2g(s^2-p^2)-R]}{2g}. \tag{A.1.13}$$

Since $g > 0$, the first term is positive. Likewise, the second term is positive if the bracketed expression is positive. Some algebra and Eq. (A.1.11) shows that $2g(s^2 - p^2) - R > s^2 h$, where $h = 3s^2 - 4p^2 - 4\sqrt{s^2 - p^2}\sqrt{d^2 - p^2}$. We need to show $h > 0$. The extrema of h occur when

$$\frac{dh}{dp} = 4p\left(-2 + \sqrt{\frac{s^2 - p^2}{d^2 - p^2}} + \sqrt{\frac{d^2 - p^2}{s^2 - p^2}}\right) \tag{A.1.14}$$

vanishes. A minimum occurs at $p = 0$, where $h = s(3s - 4d) > 0$ since $d < \sqrt{2}s$. Other extrema could exist if $2 = \sqrt{s^2 - p^2}/\sqrt{d^2 - p^2} + \sqrt{d^2 - p^2}/\sqrt{s^2 - p^2}$; however, this requires the unphysical condition that $d = s$. It follows then that $h > 0$, allowing us to conclude that $\Re D > 0$ if $\Im D = 0$ along $\overline{BC}$.

At C, $\Im D = 0$ and $\Re D = (1 - \eta^{-1})s^4$. This is then the only location at which $\Im D = 0$ with $\Re D < 0$, which only occurs when $\eta < 1$. For a point on Γ_{br} just to the left of C (i.e., $q = -\epsilon + \mathrm{i}\epsilon$),

$$\frac{\Im D}{s\epsilon^2} = -\eta^{-1}(9s - 8d) + 2s + 2(3s - 4d)\cos^2\phi. \tag{A.1.15}$$

We show that this is negative for $\eta > 1$. As η decreases, the expression becomes more negative; hence, it is sufficient to show that the expression is negative for $\eta = 1$. For $\eta = 1$, the expression may be written as $-(7s - 8d) + (6s - 8d)\cos^2\phi$. Since $s \geq \sqrt{2}d$, this is negative. Thus $\Im D < 0$ at this point and the image path

crosses the real axis to the left of the origin moving in a clockwise direction. We conclude that for $\eta < 1$, the dispersion relation has two roots, and for $\eta > 1$ it has three.

A.2 Long-time Response of the System to Transient Excitations

We investigate how the roots of the dispersion relation (4.5.1) determine the long-time response of the system to transient excitations, particularly to elucidate the signature of the standing wave mode. For simplicity, we consider the response of a single spatial Fourier mode to a step function stress drop, similar to the analysis of Geubelle and Rice (1995). The boundary conditions are

$$\begin{aligned} \sigma_{xz} &= -SH(t)\mathrm{e}^{\mathrm{i}k(x\cos\phi+y\sin\phi)} \\ \frac{\sigma_{yz}}{\mu} - \eta\frac{v_y}{c_s} &= 0 \\ \sigma_{zz} &= 0, \end{aligned} \tag{A.2.1}$$

where S has units of force/area. The Laplace transformed solution for particle velocity is

$$v_i(\Omega, k, \phi, z) = \frac{-iS}{\mu k D(\Omega, \phi)} \left[f_i^d(\Omega, \phi) \mathrm{e}^{-k\alpha_p z} + f_i^s(\Omega, \phi) \mathrm{e}^{-k\alpha_s z} \right], \qquad \text{(A.2.2)}$$

where f_i^d and f_i^s are defined in Eq. (4.6.4) and the $\exp[\mathrm{i}k(x\cos\phi + y\sin\phi)]$ in this and following expressions is assumed. The inverse Laplace transform is

$$v_i(t, k, \phi, z) = \frac{k}{2\pi} \int_{-\infty+\mathrm{i}0}^{\infty+\mathrm{i}0} dc v_i(\Omega, k, \phi, z) \mathrm{e}^{-\mathrm{i}k\Omega t}. \qquad \text{(A.2.3)}$$

We close the inversion contour with a semicircle at infinity in the lower half-space, as shown in Fig. A.2, similar to the procedure of Eason (1966). Integral terms arise from distorting the contour around the branch cuts, corresponding to the head waves. We obtain residue contributions from the poles that occur when $D(\Omega, \phi) = 0$. These correspond to the propagating interface waves (denoted $\Omega_\pm$) and standing wave mode (denoted Ω_0) discussed previously. We focus on these residues, which provide the asymptotic solution in the vicinity of the interface in the long-time limit, as described by Chao et al. (1961) in the context of a free surface. These are simple poles, so their contribution to the inversion integral is

$$
\begin{aligned}
v_i(t,k,\phi,z) \;=\; & \left[\frac{v_i(\Omega,k,\phi,z)D(\Omega,\phi)}{\partial D(\Omega,\phi)/\partial\Omega}\right]_{\Omega=\Omega_+} \mathrm{e}^{-\mathrm{i}k\Omega_+ t} + \\
& \left[\frac{v_i(\Omega,k,\phi,z)D(\Omega,\phi)}{\partial D(\Omega,\phi)/\partial\Omega}\right]_{\Omega=\Omega_-} \mathrm{e}^{-\mathrm{i}k\Omega_- t} + \\
& \left[\frac{v_i(\Omega,k,\phi,z)D(\Omega,\phi)}{\partial D(\Omega,\phi)/\partial\Omega}\right]_{\Omega=\Omega_0} \mathrm{e}^{-\mathrm{i}k\Omega_0 t}
\end{aligned}
\tag{A.2.4}
$$

In order to have a distinguishable signature, the decay rate of the standing wave mode must be small in some region of parameter space where the residue is large. We find that the residue of v_y for this mode is an order of magnitude larger than that of v_x or v_z, again suggesting that the physical nature of this mode is related to the competition in the transverse direction between radiation damping and the effective viscosity. Fig. A.3 shows the amplitude of the residue for v_y as a function of ϕ and η. It is largest for mixed mode perturbations and increases as η decreases to unity (counteracting this, however, is the increasing decay rate as η decreases). As an example, we consider the case when $\phi = 3\pi/8$ and $\eta = 10$. We compare the residue contributions to the exact response computed numerically by the boundary integral methodology; results are presented in Fig. A.4.

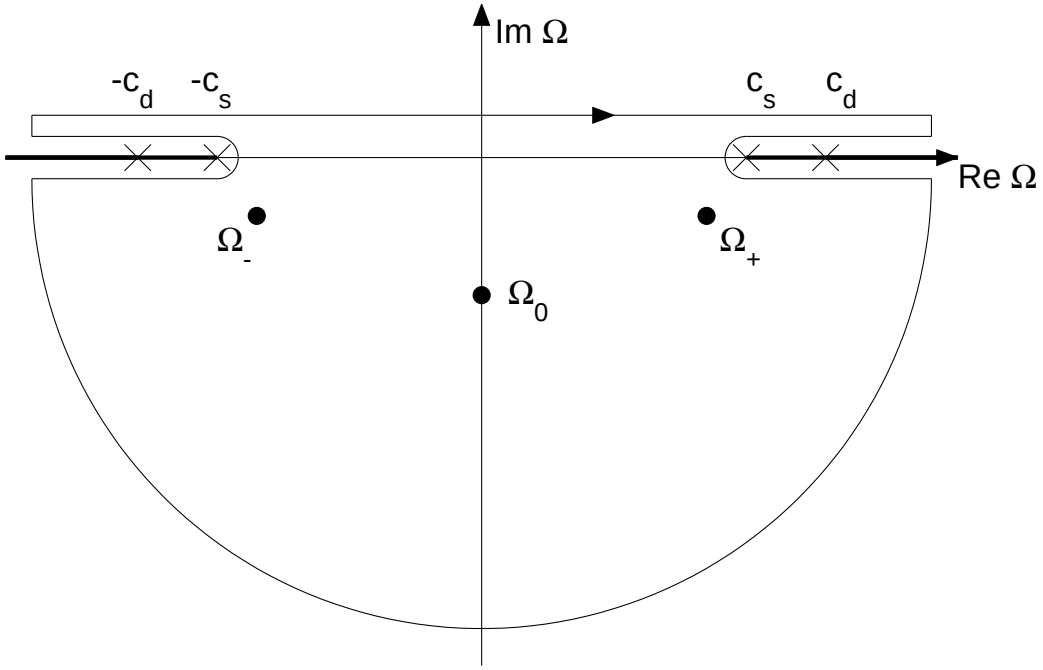

Figure A.2: Inversion contour for the Laplace transform, which is distorted around the branch cuts. The contour is interpreted in the limit that the paths parallel to the $\Re\Omega$-axis, here drawn slightly offset from it, converge upon it.

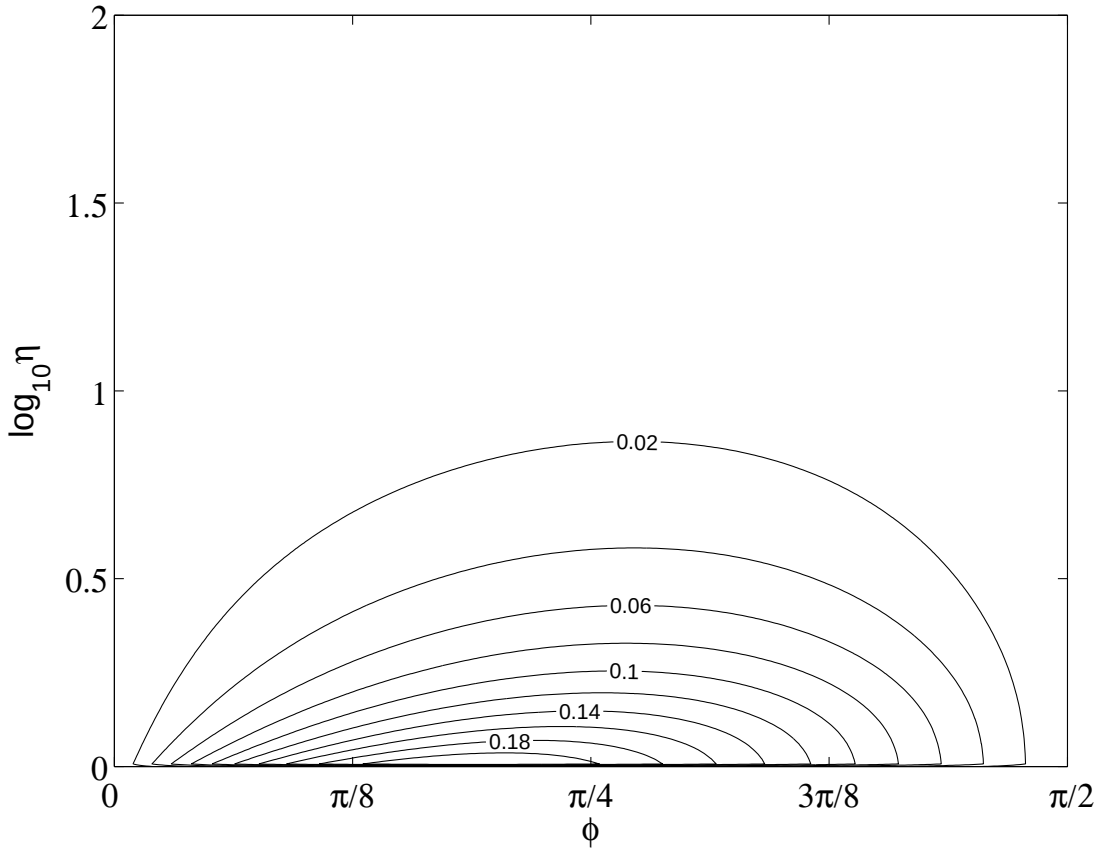

Figure A.3: Standing wave mode residue contribution to a single Fourier mode of v_y under a step function stress drop. The amplitude is nondimensionalized by $c_s S/\mu$.

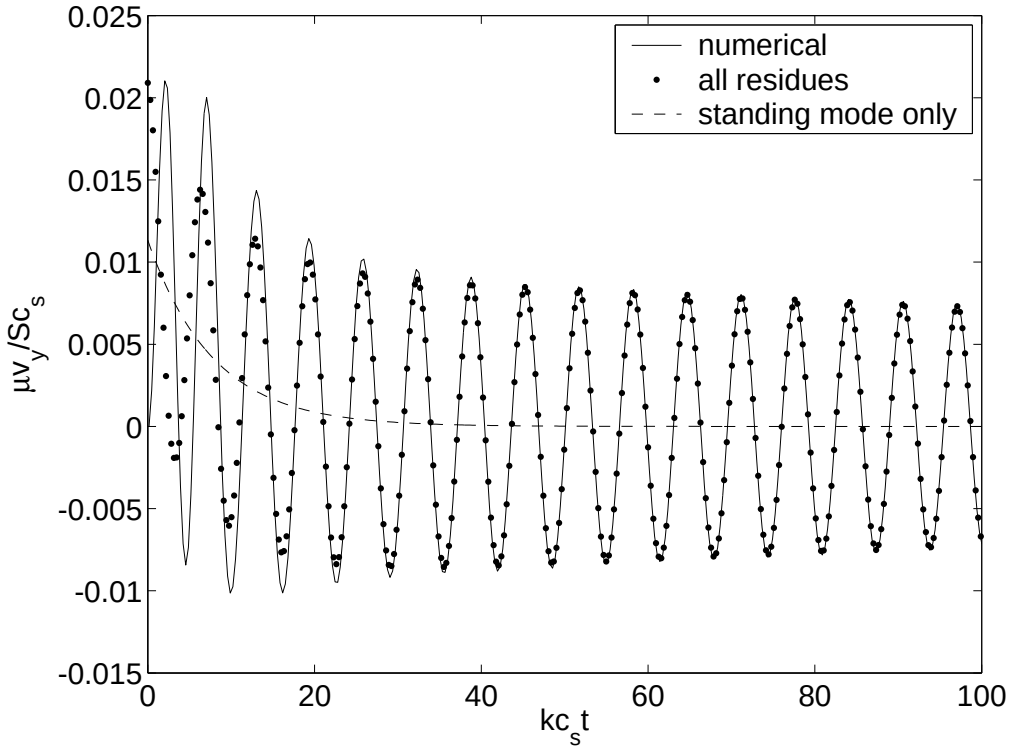

Figure A.4: Response of a single Fourier mode to a step function stress drop for $\phi = 3\pi/8$ and $\eta = 10$. The numerical solution is compared to the sum of all residue contributions, which is dominated in the long-time limit by the oscillatory decay from the propagating interface wave modes, rather than the standing wave mode.

Appendix B

Appendices to Chapter 5

B.1 Derivation of the Steady State Solution

Consider two identical isotropic linear elastic half-spaces, having a shear modulus μ and P- and S-wave speeds c_p and c_s, joined along the interface $y = 0$. Along this fault a steady state two-dimensional rupture pulse propagates in the positive x direction at a constant velocity V. The fields are a function of $x - Vt$ and y only, and for convenience we shall take $t = 0$ such that $x - Vt \to x$ in the following expressions, equivalent to transforming into a frame of reference moving with the rupture. We shall take the origin of the coordinate system to coincide with the rupture front. On the fault, we specify the length of the slip zone L and the shear traction within the slip zone $\tau(x)$. The mixed boundary value problem

is defined formally as

$$\begin{aligned} v_x(\infty < x < -L, y = 0) &= 0 \\ \sigma_{xy}(-L < x < 0, y = 0) &= \tau(x) - \tau_0 \qquad \text{(B.1.1)} \\ v_x(0 < x < \infty, y = 0) &= 0 \\ \sigma_{yy}(-\infty < x < \infty, y = 0) &= 0, \qquad \text{(B.1.2)} \end{aligned}$$

where v_i are velocities, σ_{ij} are stresses, and τ_0 is the initial shear stress on the fault far ahead of and behind the slip zone. The healing process at the trailing edge of the slip zone ($x = -L$) is assumed to be energy-neutral (i.e., it is accompanied by neither dissipation nor release of energy).

We first consider the general case of an arbitrary $\tau(x)$, but later specialize to the linear distance-weakening model of Palmer and Rice (1973):

$$\tau(x) = \begin{cases} \tau_p + (\tau_p - \tau_r)x/R, & -R < x < 0 \\ \tau_r, & -L < x < -R, \end{cases} \qquad \text{(B.1.3)}$$

where τ_p is the peak strength, τ_r is the residual strength, and R is the length of the breakdown zone.

Expressions for the shear traction and slip velocity on the fault for both subshear ($V < c_s$) and supershear ($V > c_s$) ruptures having an arbitrary $\tau(x)$ have

been given by Broberg (1978, 1989), who also examined the off-fault fields only in the limiting case of a vanishingly small breakdown zone. We present the complete derivation for all fields, both on and off of the fault, at supershear speeds. A recent derivation of the subshear expressions is given by Rice et al. (2005), although they do not present results for the velocity fields. First, we decompose the displacement field u_i into dilatational and shear components:

$$u_i(x,y) = u_i^p(x,y) + u_i^s(x,y), \tag{B.1.4}$$

governed by

$$\left(\alpha_p^2 \frac{\partial^2}{\partial x^2} + \frac{\partial^2}{\partial y^2}\right) u_i^p(x,y) = 0 \tag{B.1.5}$$

and

$$\left(-\beta_s^2 \frac{\partial^2}{\partial x^2} + \frac{\partial^2}{\partial y^2}\right) u_i^s(x,y) = 0, \tag{B.1.6}$$

with $\alpha_p = \sqrt{1 - V^2/c_p^2}$ and $\beta_s = \sqrt{V^2/c_s^2 - 1}$. The P-wave equation is elliptic with evanescent (i.e., inhomogeneous) wave eigenfunctions. In contrast to the subshear expressions, the S-wave equation at supershear velocities is now hyperbolic and its eigenfunctions are radiating S waves, which form a planar Mach front extending from the rupture front.

A solution to these equations, restricting ourselves to $y \geq 0$ for now and taking into account the conditions $\nabla \times \mathbf{u}^p = 0$ and $\nabla \cdot \mathbf{u}^s = 0$, is

$$\begin{aligned} u_x^p(x,y) &= \Re P(z_p) \\ u_y^p(x,y) &= -\alpha_p \Im P(z_p) \\ u_x^s(x,y) &= -\beta_s S(z_s) \\ u_y^s(x,y) &= S(z_s), \end{aligned} \tag{B.1.7}$$

where $z_p = x + i\alpha_p y$ and $z_s = x + \beta_s y$. Here, $P(z)$ is a function that is analytic except across the slip zone, and $S(z)$ is a real function. In terms of these functions,

$$\sigma_{yy} = (\beta_s^2 - 1)\Re P'(z_p) + 2\beta_s S'(z_s), \tag{B.1.8}$$

where the prime indicates differentiation with respect to the argument. Setting this expression equal to zero on the fault, as required by the boundary condition (B.1.2), yields

$$S'(x) = -\frac{\beta_s^2 - 1}{2\beta_s}\Re P'(x). \tag{B.1.9}$$

This expression remains valid away from the fault under the substitution $x \to z_s$. We use (B.1.9) to eliminate $S'(z)$ and rewrite expressions for the fields in terms of a new analytic function

$$N(z) = 2i\mu\alpha_p P'(z), \tag{B.1.10}$$

yielding

$$\begin{aligned}
v_x &= -\frac{V}{\mu}\left[\frac{1}{2\alpha_p}\Im N(z_p) + \frac{\beta_s^2-1}{4\alpha_p}\Im N(z_s)\right] \\
v_y &= -\frac{V}{\mu}\left[\frac{1}{2}\Re N(z_p) - \frac{\beta_s^2-1}{4\alpha_p\beta_s}\Im N(z_s)\right] \\
\sigma_{xx} &= \frac{1+\beta_s^2+2\alpha_p^2}{2\alpha_p}\Im N(z_p) + \frac{\beta_s^2-1}{2\alpha_p}\Im N(z_s) \\
\sigma_{xy} &= \Re N(z_p) + \frac{(\beta_s^2-1)^2}{4\alpha_p\beta_s}\Im N(z_s) \\
\sigma_{yy} &= \frac{\beta_s^2-1}{2\alpha_p}\Im\left[N(z_p) - N(z_s)\right].
\end{aligned} \tag{B.1.11}$$

At this point, we apply the mode II symmetry properties:

$$\begin{aligned}
\Re N(z) &= \Re N(\bar{z}) \\
\Im N(z) &= -\Im N(\bar{z}),
\end{aligned} \tag{B.1.12}$$

where the overbar denotes complex conjugation, an operation that replaces y by $-y$ (effectively reflecting the observation point across the fault). This implies that $N(\bar{z}) = \bar{N}(z)$; hence,

$$\Re N(x) = \frac{N_+(x) + N_-(x)}{2}$$
$$\Im N(x) = \frac{N_+(x) - N_-(x)}{2i}, \tag{B.1.13}$$

where $N_\pm(x) = \lim_{y\to 0^\pm} N(z)$. Inserting (B.1.13) into the traction boundary condition (B.1.1) yields

$$N_+(x) = \frac{B - iA}{B + iA} N_-(x) + 2\frac{\tau(x) - \tau_0}{1 - iB/A} \tag{B.1.14}$$

for $-L < x < 0$, where $A = 4\alpha_p\beta_s$ and $B = (\beta_s^2 - 1)^2$. Writing

$$e^{-2\pi iq} = \frac{B - iA}{B + iA}, \tag{B.1.15}$$

yields

$$q = \frac{1}{\pi} \arctan \frac{A}{B} \tag{B.1.16}$$

with $0 < q \leq 1/2$. This allows us to recast (B.1.14) as

$$\begin{aligned} N_+(x) &= e^{-2\pi iq} N_-(x) + \\ &\quad 2i \sin(\pi q) e^{-i\pi q} \left[\tau(x) - \tau_0\right]. \end{aligned} \tag{B.1.17}$$

This defines a Hilbert problem Muskhelishvili (1953), which is solved by first introducing a solution $X(z)$ to the homogeneous problem

$$X_+(x) = e^{-2\pi i q} X_-(x). \tag{B.1.18}$$

Using this result to eliminate the factor $e^{-2\pi i q}$ yields

$$\frac{N_+(x)}{X_+(x)} = \frac{N_-(x)}{X_-(x)} + 2i \sin(\pi q) e^{-i\pi q} \frac{\tau(x) - \tau_0}{X_+(x)}. \tag{B.1.19}$$

An appropriate selection of $X(z)$ for a semi-infinite crack is $X(z) = z^{1-q}$, and for a pulse of length L is $X(z) = z^{1-q}(z+L)^q$. The branch cut is taken along $-L < x < 0$, $y = 0$. Defining

$$F(z) = \frac{N(z)}{X(z)} \tag{B.1.20}$$

and

$$f(x) = 2i \sin(\pi q) e^{-i\pi q} \frac{\tau(x) - \tau_0}{X_+(x)} \tag{B.1.21}$$

allows us to rewrite (B.1.19) as

$$F_+(x) - F_-(x) = f(x). \tag{B.1.22}$$

Using the Cauchy integral theorem to relate the value of F at some point z away from the fault to the jump in F across the slip zone (see Rice et al. (2005) for a complete description) solves the equation as

$$F(z) = \frac{1}{2\pi i}\int_{-L}^{0} \frac{f(w)}{w-z}dw + E(z), \tag{B.1.23}$$

where $E(z)$ is an entire function (i.e., a polynomial in z). Since the fields vanish at infinity (except within the region of S-wave radiation), $E(z) = 0$. Thus,

$$\begin{aligned} N(z) &= -\frac{\sin(\pi q)}{\pi} z^{1-q}(z+L)^q \times \\ &\int_{-L}^{0} \frac{\tau(w)-\tau_0}{(-w)^{1-q}(w+L)^q(w-z)}dw. \end{aligned} \tag{B.1.24}$$

Note that $N(z)$ is of the form $(\tau_p - \tau_r)h(R/L, V/c_s)$, which is quite different from the scaling for subshear ruptures, in which the dependence on V/c_s, here arising through q, is absent. The physical reason for this is related to the velocity-dependent S-wave radiation at supershear speeds. These waves alter the energy balance within the breakdown zone and the concentration of the stress fields around the rupture front.

To complete the solution, we must place a constraint on τ_0 by using the fact that the fields vanish at infinity (outside of the radiating S-wave region). Inserting (B.1.24) into (B.1.11) and taking the limit that $z \to \infty$ ahead of the Mach front

yields the constraint

$$\tau_0 = \frac{\sin(\pi q)}{\pi} \int_{-L}^{0} \frac{\tau(x)dx}{(-x)^{1-q}(x+L)^q}. \tag{B.1.25}$$

For subshear ruptures, an analogous derivation yields

$$\begin{aligned}
v_x &= -\frac{V}{\mu}\left[\frac{1}{2\alpha_p}\Im M(z_p) + \frac{\beta_s^2-1}{4\alpha_p}\Im M(z_s)\right] \\
v_y &= -\frac{V}{\mu}\left[\frac{1}{2}\Re M(z_p) - \frac{\beta_s^2-1}{4\alpha_p\beta_s}\Im M(z_s)\right] \\
\sigma_{xx} &= \frac{1+\beta_s^2+2\alpha_p^2}{2\alpha_p}\Im M(z_p) + \frac{\beta_s^2-1}{2\alpha_p}\Im M(z_s) \\
\sigma_{xy} &= \Re M(z_p) + \frac{(\beta_s^2-1)^2}{4\alpha_p\beta_s}\Im M(z_s) \\
\sigma_{yy} &= \frac{\beta_s^2-1}{2\alpha_p}\Im\left[M(z_p) - M(z_s)\right],
\end{aligned} \tag{B.1.26}$$

where

$$\begin{aligned}
M(z) &= -\frac{1}{\pi} z^{1/2}(z+L)^{1/2} \times \\
&\qquad \int_{-L}^{0} \frac{\tau(w)-\tau_0}{(-w)^{1/2}(w+L)^{1/2}(w-z)} dw.
\end{aligned} \tag{B.1.27}$$

The expressions for the stress components have been given by Rice et al. (2005). Note that $M(z)$ takes the form $(\tau_p - \tau_r)h(R/L)$, and is independent on rupture velocity (since for any subshear V, the fields in the singular model diverge with

an inverse square-root singularity). This results in the ability to factor the speed dependent function out of the expressions for the fields, which cannot be done for supershear ruptures.

B.2 Shear-Wave Radiation from Supershear Ruptures

In this section, we examine properties of the S-wave radiation from supershear ruptures. First, note that the shear component of the fields given in (B.1.11) involves only $\Im N(z)$; consequently, when $N(z)$ is purely real, no S-wave radiation will be present. It is thus desirable to study the properties of $N(z)$ in more detail.

Let us define

$$I(z) = \int_{-L}^{0} \frac{\tau(w) - \tau_0}{(-w)^{1-q}(w+L)^q(w-z)} dw, \tag{B.2.1}$$

which is the singular integral in (B.1.24). This has real and imaginary parts given by

$$\Re I(z) = \int_{-L}^{0} \frac{[\tau(w) - \tau_0]\,(w - z_R)}{(-w)^{1-q}(w+L)^q\,[(w-z_R)^2 + z_I^2]} dw \tag{B.2.2}$$

and

$$\Im I(z) = \int_{-L}^{0} \frac{[\tau(w) - \tau_0]\, z_I}{(-w)^{1-q}(w+L)^q \left[(w - z_R)^2 + z_I^2\right]} dw, \tag{B.2.3}$$

where $z_R = \Re z$ and $z_I = \Im z$. Now let us take the limit that $z_I \to 0$, equivalent to letting the observation point approach the fault. Care must be taken in (B.2.3), and we note that

$$\lim_{y \to 0} \frac{y}{(w-x)^2 + y^2} = \pi \delta(w - x). \tag{B.2.4}$$

Thus,

$$\Re I_+(x) = \int_{-L}^{0} \frac{\tau(w) - \tau_0}{(-w)^{1-q}(w+L)^q (w-x)} dw, \tag{B.2.5}$$

which is interpreted in the Cauchy principal value sense when $-L < x < 0$, and

$$\Im I_+(x) = \pi \frac{\tau(x) - \tau_0}{(-x)^{1-q}(x+L)^q} \tag{B.2.6}$$

for $-L < x < 0$; otherwise, $\Im I_+(x) = 0$.

Now we shall examine the behavior of $N(x)$ on the fault. Ahead of the slip zone ($x > 0$), $\Im I_+(x) = 0$ and we are left with the purely real expression

$$\begin{aligned} N_+(x) &= -\frac{\sin(\pi q)}{\pi} x^{1-q}(x+L)^q \times \\ &\quad \int_{-L}^{0} \frac{\tau(w) - \tau_0}{(-w)^{1-q}(w+L)^q (w-x)} dw. \end{aligned} \tag{B.2.7}$$

This result applies away from the fault as well, upon the substitution $x \to z_s$ since z_s is also real. Since the S-wave terms involve only $\Im N(z_s)$, this proves that the S waves vanish ahead of the S Mach front, defined by $x + \beta_s|y| = 0$.

Within the slip zone ($-L < x < 0$), (B.1.24) reduces to the complex expression

$$\begin{aligned} N_+(x) &= \frac{\sin(\pi q)}{\pi} e^{-i\pi q} \Bigg\{ (-x)^{1-q}(x+L)^q \times \\ &\quad \int_{-L}^{0} \frac{[\tau(w) - \tau_0]}{(-w)^{1-q}(w+L)^q(w-x)} dw \\ &\quad + i\pi \left[\tau(x) - \tau_0\right] \Bigg\}, \end{aligned} \tag{B.2.8}$$

which can be used in (B.1.11) to verify that $\sigma_{xy}(-L < x < 0) = \tau(x) - \tau_0$.

Behind the slip zone ($x < -L$), $\Im I_+(x) = 0$ and (B.1.24) reduces to the purely real expression

$$\begin{aligned} N_+(x) &= \frac{\sin(\pi q)}{\pi} (-x)^{1-q}(-x-L)^q \times \\ &\quad \int_{-L}^{0} \frac{[\tau(w) - \tau_0]}{(-w)^{1-q}(w+L)^q(w-x)} dw. \end{aligned} \tag{B.2.9}$$

Equations (B.2.7)-(B.2.9), when combined with (B.1.11), reveal an important result: S waves radiate only from the slip zone, as would be expected if working from the representation theorem.

Consequently, we focus on the behavior of the fields off of the fault between

the passage of the Mach front originating from $x = 0$ and that from $x = -L$ (i.e., when $-L < z_s < 0$). First, we observe that the slip velocity Δv on the fault may be written in terms of $\Im N(x)$ only as

$$\Delta v(x) = -2\frac{V}{\mu}\frac{\beta_s^2 + 1}{4\alpha_p}\Im N_+(x). \tag{B.2.10}$$

Using this in the off-fault expressions for velocity (B.1.11) yields

$$v_x = -\frac{V}{\mu}\left[\frac{1}{2\alpha_p}\Im N(z_p)\right] + \frac{\beta_s^2 - 1}{2(\beta_s^2 + 1)}\Delta v(z_s) \tag{B.2.11}$$

$$v_y = -\frac{V}{\mu}\left[\frac{1}{2}\Re N(z_p)\right] - \frac{1}{2\beta_s}\frac{\beta_s^2 - 1}{\beta_s^2 + 1}\Delta v(z_s), \tag{B.2.12}$$

which proves that both components of the off-fault velocity fields trace out the exact slip velocity function on the fault during the passage of the S waves. The usefulness of this feature rests on the separation of the shear and dilatational fields, which occurs for points sufficiently removed from the fault.

We also use our results to obtain the fracture energy G and final slip δ. We merely numerically integrate the following expressions

$$G = \frac{1}{V}\int_{-L}^{0} \Delta v(x)\left[\tau(x) - \tau_r\right] dx \tag{B.2.13}$$

and

$$\delta = \frac{1}{V}\int_{-L}^{0} \Delta v(x)dx, \tag{B.2.14}$$

where $\Delta v(x)$ is also obtained by numerical integration. Note that (B.2.13) and (B.2.14) are strictly valid only for steady state conditions. We find no problems with this procedure, and validate our numerical results against the analytical solution for subshear ruptures having a specific $\tau(x)$ given by Rice et al. (2005).

Dimensional considerations allow G to be written as

$$G = h(R/L, V/c_s)(\tau_p - \tau_r)^2 R/\mu. \tag{B.2.15}$$

Only for subshear ruptures can $h(R/L, V/c_s)$ be factored into the product of $f(V/c_s)$ and $g(R/L)$, as follows from the discussion after equations (B.1.24) and (B.1.27).

At supershear speeds, not all of the work done by the remote stress field in excess of friction goes into fracture energy, as is the case for subshear ruptures Rice et al. (2005). Instead, there is a flow of energy out to infinity associated with the radiating S waves. Let us denote this energy flux (per unit area advance of the rupture) as G_s. This quantity may be calculated by integrating the outward energy flux associated with the shear field over the slip zone. The fault-normal component of the energy flux is given by

$$\mathcal{F}_y = -\sigma_{xy} v_x - \sigma_{yy} v_y, \tag{B.2.16}$$

which may be simplified by eliminating the second term using $\sigma_{yy} = 0$, and G_s is given by

$$G_s = \frac{2}{V} \int_{-L}^{0} \mathcal{F}_y^s(x) dx \tag{B.2.17}$$

under steady state conditions. The factor of two arises from radiation leaving both sides of the fault. Substituting only the shear part of the field expressions in (B.1.11) for the stress and velocity components in (B.2.16), and using (B.2.10) to eliminate $\Im N_+(x)$ in favor of $\Delta v(x)$ yields

$$G_s = 2 g_s(V/c_s) \rho \int_{-L}^{0} \Delta v(x)^2 dx, \tag{B.2.18}$$

where ρ is the density of the medium and

$$g_s(V/c_s) = \frac{1}{\beta_s} \left(\frac{\beta_s^2 - 1}{\beta_s^2 + 1} \right)^2. \tag{B.2.19}$$

Dimensional considerations show that G_s, like G, takes the form

$$G_s = h_s(R/L, V/c_s)(\tau_p - \tau_r)^2 R/\mu, \tag{B.2.20}$$

such that the energetics of supershear ruptures depends strongly on both the size of the breakdown zone and the rupture velocity.

Bibliography

Aagaard, B., Anderson, G., Hudnut, K. W., 2004. Dynamic rupture modeling of the transition to strike-slip motion in the 2002 Denali Fault, Alaska, earthquake. Bull. Seismol. Soc. Am. submitted.

Aagaard, B., Heaton, T. H., 2003. How do near-source ground motions change when ruptures go supershear? Eos Trans. AGU 84, Fall Meet. Suppl., Abstract S42H–08.

Abraham, F. F., Gao, H., 2000. How fast can cracks propagate? Phys. Rev. Lett. 84, 3113–3116.

Abraham, F. F., Walkup, R., Gao, H., Duchaineau, M., Rubia, T. D. D. L., Seager, M., 2002. Simulating materials failure by using up to one billion atoms and the world's fastest computer: Brittle fracture. Proc. Natl. Acad. Sci. 99, 5777–5782.

BIBLIOGRAPHY

Achenbach, J. D., 1973. Wave Propagation in Elastic Solids. North-Holland, Amsterdam.

Achenbach, J. D., Epstein, H. I., 1967. Dynamic interaction of a layer and a half-space. J. Eng. Mech. Div. EM5, 27–42.

Achenbach, J. D., Harris, J. G., 1978. Ray method for elastodynamic radiation from a slip zone of arbitrary shape. J. Geophys. Res. 83, 2283–2291.

Adams, G. G., 1995. Self-excited oscillations of two elastic half-spaces sliding with a constant coefficient of friction. J. Appl. Mech. 62, 867–872.

Aki, K., 1968. Seismic displacements near a fault. J. Geophys. Res. 73, 5359–5376.

Aki, K., Richards, P., 2002. Quantitative Seismology. University Science Books, Sausalito, California.

Anderson, G., Aagaard, B., Hudnut, K., 2003. Fault interactions and large complex earthquakes in the los angeles area. Science 302, 1946–1949.

Andrews, D. J., 1976. Rupture velocity of plane strain shear cracks. J. Geophys. Res. 81, 5679–5687.

Andrews, D. J., 1994. Dynamic growth of mixed mode shear cracks. Bull. Seismol. Soc. Am. 84, 1184–1198.

BIBLIOGRAPHY

Antipov, Y. A., Obrezanova, O., Willis, J. R., 2004. A fracture criterion of "Barenblatt" type for an intersonic shear crack. Math. Mech. Solids 9, 271–283.

Antolik, M., Abercrombie, R. E., Ekstrom, G., 2004. The 14 November 2001 Kokoxili (Kunlunshan), Tibet, earthquake: Rupture transfer through a large extensional step-over. Bull. Seismol. Soc. Am. 94, 1173–1194.

Archuleta, R. J., 1984. A faulting model for the 1979 Imperial Valley earthquake. J. Geophys. Res. 89, 4559–4585.

Archuleta, R. J., Day, S. M., 1980. Dynamic rupture in a layered medium: an example, the 1966 Parkfield earthquake. Bull. Seismol. Soc. Am. 70, 671–690.

Archuleta, R. J., Hartzell, S. H., 1981. Effects of fault finiteness on near-source ground motion. Bull. Seismol. Soc. Am. 71, 939–957.

Barenblatt, G. I., 1959. The formation of equilibrium cracks during brittle fracture: General ideas and hypotheses, axially-symmetric cracks. Appl. Math. Mech. (PMM) 23, 622–636.

Beroza, G., Mikumo, T., 1996. Short slip duration in dynamic rupture in the presence of heterogeneous fault properties. J. Geophys. Res. 101, 22,449–22,460.

Beroza, G., Spudich, P., 1988. Linearized inversion for fault rupture behavior:

application to the 1984 Morgan Hill, California, earthquake. J. Geophys. Res. 93, 6275–6296.

Bouchon, M., Bouin, M. P., Karabulut, H., Toksöz, M. N., Dietrich, M., Rosakis, A., 2001. How fast is rupture during an earthquake? New insights from the 1999 Turkey earthquakes. Geophys. Res. Lett. 28, 2723–2726.

Bouchon, M., Toksöz, M. N., Karabulut, H., Bouin, M. P., Dietrich, M., Aktar, M., Edie, M., 2000. Seismic imaging of the 1999 Izmit (Turkey) rupture inferred from the near-fault recordings. Geophys. Res. Lett. 27, 3013–3016.

Bouchon, M., Vallée, M., 2003. Observation of long supershear rupture during the magnitude 8.1 Kunlunshan earthquake. Science 301, 824–826.

Broberg, K. B., 1960. The propagation of a brittle crack. Ark. Fys. 18, 159–192.

Broberg, K. B., 1978. On transient sliding motion. Geophys. J. Roy. Astr. Soc. 52, 397–432.

Broberg, K. B., 1989. The near-tip field at high crack velocities. Int. J. Fract. 39, 1–13.

Broberg, K. B., 1994. Intersonic bilateral slip. Geophys. J. Int. 119, 706–714.

BIBLIOGRAPHY

Broberg, K. B., 1995. Intersonic mode II crack expansion. Arch. Mech. 47, 859–871.

Broberg, K. B., 1999a. Cracks and Fracture. Academic Press, London.

Broberg, K. B., 1999b. Intersonic mode II crack acceleration. Fatigue Fract. Engng. Mater. Struct. 22, 17–24.

Brock, L. M., 1982. Shear and normal impact loadings on one face of a narrow slit. Int. J. Solid Structures 18, 467–477.

Brune, J., 1970. Tectonic stress and the spectra of seismic shear waves from earthquakes. J. Geophys. Res. 75, 4997–5009.

Burridge, R., 1973. Admissible speeds for plane-strain shear cracks with friction but lacking cohesion. Geophys. J. Roy. Astr. Soc. 35, 439–455.

Burridge, R., Conn, G., Freund, L. B., 1979. The stability of a rapid mode II shear crack with finite cohesive traction. J. Geophys. Res. 85, 2210–2222.

Cagniard, L., 1962. Reflection and Refraction of Progressive Seismic Waves. McGraw-Hill, New York.

Chao, C. C., Bleich, H. H., Sackman, J., 1961. Surface waves in an elastic half space. J. Appl. Mech. 28, 300–301.

BIBLIOGRAPHY

Cho, H., Barber, J. R., 1999. Stability of the three-dimensional Coulomb friction law. Proc. R. Soc. Lond. A 455, 839–861.

Cochard, A., Madariaga, R., 1994. Dynamic faulting under rate-dependent friction. Pure Appl. Geophys. 142, 419–445.

Cohee, B. P., Beroza, G. C., 1994. Slip distribution of the 1992 Landers earthquake and its implications for earthquake source mechanics. Bull. Seismol. Soc. Am. 84, 692–712.

Cotton, F., Campillo, M., 1995. Frequency domain inversion of strong motions: Application to the 1992 Landers earthquake. J. Geophys. Res. 100, 3961–3975.

Craggs, J. W., 1960. On the propagation of a crack in an elastic-brittle material. J. Mech. Phys. Solids 8, 66–75.

Das, S., 2003. Dynamic fracture mechanics in the study of the earthquake rupturing process: Theory and observation. J. Mech. Phys. Solids 51, 1939–1955.

Das, S., Aki, K., 1977a. Fault plane with barriers: a versatile earthquake model. J. Geophys. Res. 82, 5658–5670.

Das, S., Aki, K., 1977b. A numerical study of two-dimensional spontaneous rupture propagation. Geophys. J. Roy. Astr. Soc. 50, 643–668.

BIBLIOGRAPHY

Das, S., Kostrov, B., 1983. Breaking of a single asperity: rupture process and seismic radiation. J. Geophys. Res. 88, 4277–4288.

Day, S. M., 1982a. Three-dimensional finite difference simulation of fault dynamics: Rectangular faults with fixed rupture velocity. Bull. Seismol. Soc. Am. 72, 705–727.

Day, S. M., 1982b. Three-dimensional simulation of spontaneous rupture: The effect of nonuniform prestress. Bull. Seismol. Soc. Am. 72, 1881–1902.

Dmowska, R., Rice, J. R., 1986. Fracture and its seismological applications. In: Teisseyre, R. (Ed.), Continuum Theories in Solid Earth Physics. Elsevier, pp. 187–255.

Dugdale, D. S., 1960. Yielding of steel sheets containing slits. J. Mech. Phys. Solids 8, 100–104.

Dunham, E. M., 2005. Dissipative interface waves and the transient response of a three dimensional sliding interface with Coulomb friction. J. Mech. Phys. Solids 53, 327–357.

Dunham, E. M., Archuleta, R. J., 2004. Evidence for a supershear transient during the 2002 Denali Fault earthquake. Bull. Seismol. Soc. Am. 94, S256–S268.

BIBLIOGRAPHY

Dunham, E. M., Favreau, P., Carlson, J. M., 2003. A supershear transition mechanism for cracks. Science 299, 1557–1559.

Eason, G., 1966. The displacements produced in an elastic half-space by a suddenly applied surface force. J. Inst. Math. Appl. 2, 299–326.

Eberhart-Phillips, D., Haeussler, P. J., Freymueller, J. T., Frankel, A. D., Rubin, C. M., Craw, P., Ratchkovski, N. A., Anderson, G., Carver, G. A., Crone, A. J., Dawson, T. E., Fletcher, H., Hansen, R., Hard, E. L., Harris, R. A., Hill, D. P., Hreinsdottír, S., Jibson, R. W., Jones, L. M., Kayen, R., Keefer, D. K., Larsen, C. F., Moran, S. C., Personius, S. F., Plafker, G., Sherrod, B., Sieh, K., Sitar, N., Wallace, W. K., 2003. The 2002 Denali fault earthquake, Alaska: A large magnitude, slip-partitioned event. Science 300, 1113–1118.

Ellsworth, W. L., Celebi, M., Evans, J. R., Jensen, E. G., Kayen, R., Metz, M. C., Nyman, D. J., Roddick, J. W., Spudich, P., Stephens, C. D., 2004. Near-field ground motions of the M 7.9 November 3, 2002, Denali fault, Alaska, earthquake recorded at Pump Station 10. Earthquake Spectra.

Eshelby, J. D., 1949. Uniformly moving dislocations. Proc. Phys. Soc. A 62, 307–314.

BIBLIOGRAPHY

Eshelby, J. D., 1969. The elastic field of a crack extending non-uniformly under general antiplane loading. J. Mech. Phys. Solids 17, 177–199.

Favreau, P., Campillo, M., Ionescu, I. R., 2002. Initiation of shear instability in three-dimensional elastodynamics. J. Geophys. Res. 107, 2147–2164.

Fossum, A. F., Freund, L. B., 1975. Nonuniformly moving shear crack model of a shallow focus earthquake mechanism. J. Geophys. Res. 80, 3343–3347.

Freund, L. B., 1972a. Crack propagation in an elastic solid subjected to general loading-I. Constant rate of extension. J. Mech. Phys. Solids 20, 129–140.

Freund, L. B., 1972b. Crack propagation in an elastic solid subjected to general loading-II. Non-uniform rate of extension. J. Mech. Phys. Solids 20, 141–152.

Freund, L. B., 1974. The stress intensity factor due to normal impact loading on the faces of a crack. Int. J. Solid Structures 12, 179.

Freund, L. B., 1979. The mechanics of dynamic shear crack propagation. J. Geophys. Res. 84, 2199–2209.

Freund, L. B., 1989. Dynamic Fracture Mechanics. Cambridge University Press, Cambridge.

BIBLIOGRAPHY

Fukuyama, E., Madariaga, R., 2000. Dynamic propagation and interaction of rupture front on a planar fault. Pure Appl. Geophys. 157, 1959–1979.

Fukuyama, E., Olsen, K. B., 2002. A condition for super-shear rupture propagation in a heterogeneous stress field. Pure Appl. Geophys. 157, 2047–2056.

Gao, H., Huang, Y., Abraham, F. F., 2001. Continuum and atomistic studies of intersonic crack propagation. J. Mech. Phys. Solids 49, 2113–2132.

Geubelle, P. H., Kubair, D. V., 2001. Intersonic crack propagation in homogeneous media under shear-dominated loading: numerical analysis. J. Mech. Phys. Solids 49, 571–587.

Geubelle, P. H., Rice, J. R., 1995. A spectral method for three-dimensional elastodynamic fracture problems. J. Mech. Phys. Solids 43, 1791–1824.

Gonzalez, S., 2003. Foam rubber and numerical simulations of near-fault seismic directivity. Master's thesis, San Diego State University, pp. 40-41.

Guatteri, M., Spudich, P., 1998. Coseismic temporal changes of slip direction; the effect of absolute stress on dynamic rupture. Bull. Seismol. Soc. Am. 88, 777–789.

Guatteri, M., Spudich, P., 2000. What can strong-motion data tell us about slip-weakening fault-friction laws. Bull. Seismol. Soc. Am. 90, 98–116.

Guo, G., Yang, W., Huang, Y., 2003a. Intersonic crack growth under time-dependent loading. Int. J. Solids Struct. 40, 2757–2765.

Guo, G., Yang, W., Huang, Y., Rosakis, A. J., 2003b. Sudden deceleration or acceleration of an intersonic shear crack. J. Mech. Phys. Solids 51, 311–331.

Hall, J. F., Heaton, T. H., Halling, M. W., Wald, D. J., 1995. Near-source ground motion and its effects of flexible buildings. Earthq. Spectra 11, 569–605.

Harris, R. A., Archuleta, R. J., Day, S. M., 1991. Fault steps and the dynamic rupture process: 2-D numerical simulations of a spontaneously propagating shear fracture. Geophys. Res. Lett. 18, 893–896.

Harris, R. A., Day, S. M., 1993. Dynamics of fault interaction: Parallel strike-slip faults. J. Geophys. Res. 98, 4461–4472.

Harris, R. A., Day, S. M., 1997. Effects of a low-velocity zone on a dynamic rupture. Bull. Seismol. Soc. Am. 87, 1267–1280.

Hartzell, S., Heaton, T., 1983. Inversion of strong ground motion and teleseismic waveform data for the fault rupture history of the 1979 Imperial Valley, California, earthquake. Bull. Seismol. Soc. Am. 73, 1553–1583.

Hartzell, S., Helmberger, D. V., 1982. Strong-motion modeling of the Imperial Valley earthquake of 1979. Bull. Seismol. Soc. Am. 72, 571–596.

Hatzell, S., Heaton, T., 1986. Rupture history of the 1984 Morgan hill, California, earthquake from the inversion of strong motion records. Bull. Seismol. Soc. Am. 76, 649–674.

Heaton, T. H., 1990. Evidence for and implications of self-healing pulses of slip in earthquake rupture. Phys. Earth Planet. In. 64, 1–20.

Hernandez, B., Cotton, F., Campillo, M., 1999. Contribution of radar interferometry to a two-step inversion of the kinematic process of the 1992 Landers earthquake. J. Geophys. Res. 104, 13,083–13,099.

Huang, Y., Gao, H., 2001. Intersonic crack propagation - part I: The fundamental solution. J. Appl. Mech. 68, 169–175.

Huang, Y., Gao, H., 2002. Intersonic crack propagation - part II: Suddenly stopping crack. J. Appl. Mech. 69, 76–80.

Ida, Y., 1972. Cohesive force across the tip of a longitudinal shear crack and Griffith's specific surface energy. J. Geophys. Res. 77, 3796–3805.

Ida, Y., 1973. Stress concentrations and unsteady propagation of longitudinal shear crack. J. Geophys. Res. 78, 3418–3429.

Johnson, E., 1990. On the initiation of unilateral slip. Geophys. J. Int. 101, 125–132.

Kanamori, H., Stewart, G., 1978. Seismological aspects of the Guatemala earthquake of February 4, 1976. J. Geophys. Res. 83, 3427–3434.

Kase, Y., Kuge, K., 1998. Numerical simulation of spontaneous rupture processes on two non-coplanar faults; the effect of geometry on fault interaction. Geophys. J. Int. 135, 911–922.

Kostrov, B. V., 1964. Self similar problems of propagation of shear cracks. Appl. Math. Mech. (PMM) 28, 889–898.

Kostrov, B. V., 1975. On the crack propagation with variable velocity. Int. J. Fract. 11, 47–56.

Kubair, D. V., Geubelle, P. H., Huang, Y. Y., 2002. Intersonic crack propagation in homogeneous media under shear-dominated loading: theoretical analysis. J. Mech. Phys. Solids 50, 1547–1564.

Kuo, M. K., Chen, T. Y., 1992. The Wiener-Hopf technique in elastodynamic crack problems with characteristic lengths in loading. Eng. Fract. Mech. 42, 805–813.

Luco, J. E., Anderson, J. G., 1983. Steady state response of an elastic half-space to a moving dislocation of finite width. Bull. Seismol. Soc. Am., 1–22.

BIBLIOGRAPHY

Madariaga, R., 1976. Dynamics of an expanding circular fault. Bull. Seismol. Soc. Am. 66, 639–667.

Madariaga, R., 1983. High frequency radiation from dynamic earthquake fault models. Ann. Geophys. 1, 17–23.

Madariaga, R., Cochard, A., 1994. Seismic source dynamics, heterogeneity and friction. Ann. Geophys. 37, 1349–1375.

Madariaga, R., Olsen, K. B., 2000. Criticality of rupture dynamics in 3-D. Pure Appl. Geophys. 157, 1981–2001.

Madariaga, R., Peyrat, S., Olsen, K. B., 2000. Rupture dynamics in 3d: a review. In: Boschi, E., Ekström, G., Morelli, A. (Eds.), Problems in Geophysics for the new millennium. Editrice Compositori, Bologna, Italy.

Magistrale, H., Day, S., 1999. Three-dimensional simulations of multisegment thrust fault rupture. Geophys. Res. Lett. 26, 2093–2096.

Muskhelishvili, N. I., 1953. Singular integral equations: boundary problems of function theory and their application to mathematical physics. P. Noordhoff, Groningen.

Needleman, A., 1999. An analysis of intersonic crack growth under shear loading. J. Appl. Mech. 66, 847–857.

Nielsen, S., Carlson, J. M., 2000. Rupture pulse characterization: Self-healing, self-similar, expanding solutions in a continuum model of fault dynamics. Bull. Seismol. Soc. Am. 90, 1480–1497.

Nielsen, S., Madariaga, R., 2004. On the self-healing fracture mode. Bull. Seismol. Soc. Am. 93, 2375–2388.

Obrezanova, O., Willis, J. R., 2003. Stability of intersonic shear crack propagation. J. Mech. Phys. Solids 51, 1957–1970.

Olsen, K. B., Madariaga, R., Archuleta, R. J., 1997. Three-dimensional dynamic simulation of the 1992 Landers earthquake. Science 278, 834–838.

Olson, A. H., Apsel, R. J., 1982. Finite faults and inverse theory with applications to the 1979 Imperial Valley earthquake. Bull. Seismol. Soc. Am. 72, 1969–2001.

Palmer, A. C., Rice, J. R., 1973. The growth of slip surfaces in the progressive failure of overconsolidated clay. Proc. Roy. Soc. London A 332, 527–548.

Perrin, G., Rice, J. R., Zheng, G., 1995. Self-healing slip pulse on a frictional interface. J. Mech. Phys. Solids 43, 1461–1495.

Peyrat, S., Olsen, K. B., 2004. Nonlinear dynamic rupture inversion of the 2000 Western Tottori, Japan, earthquake. Geophys. Res. Lett., in press.

Peyrat, S., Olsen, K. B., Madariaga, R., 2001. Dynamic modeling of the 1992 Landers earthquake. J. Geophys. Res. 106, 26467–26482.

Piessens, R., de Doncker-Kapenger, E., Ueberhuber, C. W., Kahaner, D. K., 1983. QUADPACK, A Subroutine Package for Automatic Integration, Springer series in computational mathematics. Springer Velag,.

Prakash, V., 1998. Frictional response of sliding interfaces subjected to time varying normal pressures. J. Tribol. 120, 97–102.

Prakash, V., Clifton, R. J., 1993. Time resolved dynamic friction measurements in pressure-shear. In: K. T. Ramesh, A. (Ed.), Experimental Techniques in the Dynamics of Deformable Solids. Appl. Mech. Div., ASME, New York, pp. 33–48.

Ranjith, K., Rice, J. R., 2001. Slip dynamics at an interface between dissimilar materials. J. Mech. Phys. Solids 49, 341–361.

Rice, J. R., 1980. The mechanics of earthquake rupture. In: Dziewonski, A. M., Boschi, E. (Eds.), Physics of Earth's Interior. Proc. Int. School Phys. Enrico Fermi, Course LXXVIII. North Holland, Amsterdam, pp. 555–649.

Rice, J. R., 1993. Spatio-temporal complexity of slip on a fault. J. Geophys. Res. 98, 9885–9907.

Rice, J. R., Lapusta, N., Ranjith, K., 2001. Rate and state dependent friction and the stability of sliding between elastically deformable solids. J. Mech. Phys. Solids 49, 1865–1898.

Rice, J. R., Sammis, C. G., Parsons, R., 2005. Off-fault secondary failure induced by a dynamic slip pulse. Bull. Seismol. Soc. Am. 95, 109–134.

Richards, P. G., 1979. Elementary solutions to lamb's problem for a point source and their relevance to three-dimensional studies of spontaneous crack propagation. Bull. Seismol. Soc. Am. 69, 947–956.

Rosakis, A. J., 2002. Intersonic shear cracks and fault ruptures. Adv. Phys. 51, 1189–1247.

Rosakis, A. J., Samudrala, O., Coker, D., 1999. Cracks faster than the shear wave speed. Science 284, 1337–1340.

Samudrala, O., Huang, Y., Rosakis, A. J., 2002. Subsonic and intersonic shear rupture of weak planes with a velocity weakening cohesive zone. J. Geophys. Res. 107, 10.1029/2001JB000460.

Spudich, P., 1992. On the inference of absolute stress levels from seismic radiation. Tectonophys. 211, 99–106.

Spudich, P., Cranswick, E., 1984. Direct observation of rupture propagation during the 1979 Imperial Valley earthquake using a short baseline accelerometer array. Bull. Seismol. Soc. Am. 74, 2083–2114.

Stoneley, R., 1924. Elastic waves at the surface of separation of two solids. Proc. R. Soc. Lond. A 106, 416–428.

Wald, D. J., Heaton, T. H., 1994. Spatial and temporal distribution of slip for the 1992 Landers, California, earthquake,. Bull. Seismol. Soc. Am. 84, 668–691.

Weertman, J., 1963. Dislocations moving uniformly on the interface between isotropic media of different elastic properties. J. Mech. Phys. Solids 11, 197–204.

Weertman, J., 1980. Unstable slippage across a fault that separates elastic media of different elastic constants. J. Geophys. Res. 85, 1455–1461.

Willis, J. R., 1973. Self-similar problems in elastodynamics. Phil. Trans. Roy. Soc. A 247, 435–491.

Woodhouse, J. H., 1974. Surface waves in a laterally layered medium. Geophys. J. Roy. Astr. Soc. 37, 461–490.

Xia, K., Rosakis, A. J., Kanamori, H., 2004. Laboratory earthquakes: The sub-Rayleigh-to-supershear transition. Science 303, 1859–1861.

Zheng, G., Rice, J. R., 1998. Conditions under which velocity-weakening friction allows a self-healing versus a cracklike mode of rupture. Bull. Seismol. Soc. Am. 88, 1466–1483.